Synthesis, Characterization and Applications of Metal Oxides Nanostructures

PhD Thesis

By

Muhammad Tariq Jan
(09-FBAS/PHDPHY/F10)

Supervised by:

Dr. Javed Iqbal

Department of Physics, FBAS, IIUI

Department of Physics
Faculty of Basic and Applied Sciences
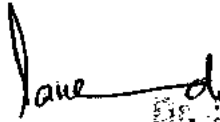**International Islamic University, Islamabad**
(2015)

nanostructure materials

Nanotechnology

Certificate

This is to certify that the work contained in this thesis entitled: **"Synthesis, Characterization and Applications of Metal Oxides Nanostructures"** has been carried out by **Mr. Muhammad Tariq Jan** in Laboratory of Nanoscience and Technology (LNT) under my supervision. In my opinion, this is fully adequate in scope and quality for the thesis of PhD Physics.

Supervisor

Department of Physics,

International Islamic University, Islamabad.

Synthesis, Characterization and Applications of Metal Oxides Nanostructures

By

Muhammad Tariq Jan
(09-FBAS/PHDPHY/F10)

A thesis submitted to

Department of Physics

For the award of the degree of

PhD Physics

Signature: _____

(Chairman, Department of Physics, IIUI)

CHAIRMAN
DEPT. OF PHYSICS
International Islamic University
Islamabad

Signature: _____

(Dean, FBAS, IIU, Islamabad)

International Islamic University, Islamabad

Faculty of Basic and Applied Sciences
Department of Physics
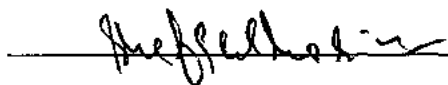
Dated: 16th October, 2015

Final Approval

This is to certify that the work in this dissertation entitled "**Synthesis, Characterization and Applications of Metal Oxides Nanostructures**" has been carried out by **Mr. Muhammad Tariq Jan**, Registration No. **09-FBAS/PHDPHY/F10** and completed in Laboratory of Nanoscience and Technology, Department of Physics, Faculty of Basic and Applied Sciences, International Islamic University, Islamabad is of sufficient standard in scope and quality for the award of degree of **PhD Physics**.

<u>COMMITTEE</u>

External Examiner 1
Dr. Shafqat Karim
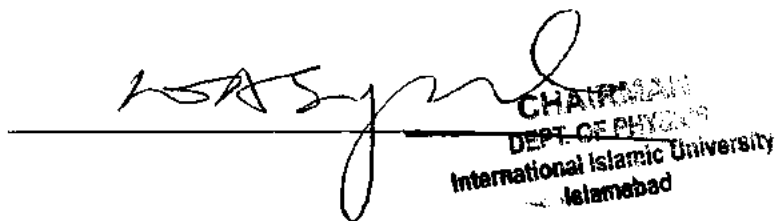Physics Division,
PINSTECH, Islamabad.

External Examiner 2
Dr. Abdul Rauf
Department of Physics,
AJK University, Muzaffarabad.

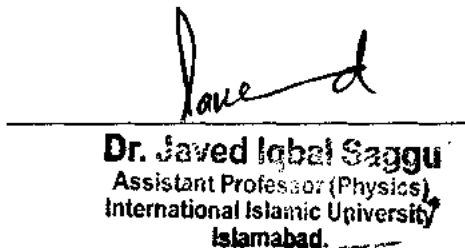**Internal Examiner**
Dr. Waqar Adil Syed

Department of Physics,

FBAS, IIUI.

Supervisor
Dr. Javed Iqbal Saggu
Department of Physics,
FBAS, IIUI.

Dr. Javed Iqbal Saggu
Assistant Professor (Physics)
International Islamic University
Islamabad.

This work is submitted as a dissertation in partial fulfillment of the requirement for the degree of

PhD in PHYSICS
at

Department of Physics

International Islamic University, Islamabad.

Declaration

I hereby declare and affirm that this thesis neither as a whole nor as part thereof has been copied out from any source. It is further declared that I have completed this thesis entirely on the basis of my personal effort, made under the sincere guidance of my supervisor. If any part of this report is proven to be copied or found to be a reproduction of some other, I shall stand by the consequences. The chapters, 3, 4, 5, 6 and 7 are based on my own publications in SCI journals as listed. No portion of the work presented in this report has been submitted in support of an application for other degree or qualification of this or any other university or institute of learning. If any part of this project is proved to be copied from any source or found to be reproduction of some other project, I (Mr. M Tariq Jan) shall be legally responsible for punishment under the plagiarism rules of Higher Education Commission (HEC), Pakistan.

Muhammad Tariq Jan

(09-FBAS/PHDPHY/F10)

DEDICATED TO

My sweet niece Rumaisa

AKNOWLEDGEMENT

I would like to express my sincere gratitude to my research supervisor Dr. Javed Iqbal Saggu (IIUI) and foreign supervisor Prof. Dr. Jan van Ruitenbeek (Leiden Institute of Physics, Leiden University, Netherland) for their continuous support, outstanding scientific guidance, tremendous cooperation and motivation. I would also like to thank Chairman Department of Physics and Dean Faculty of Basic and Applied Sciences, IIUI for their cooperation during my research work.

I am thankful to Dr. Muhammad Ismail and Mr. Qaisar Mansoor, Institute of Biomedical and Genetic Engineering Islamabad, for providing me the opportunity to do part of experimental work in their laboratory. My special thanks also go to my friends, Dr. Noor Badshah and Mr. Fazal Abbas for supporting me whenever I need them.

I am also thankful to Higher Education Commission of Pakistan (HEC), for giving me full financial assistance for carrying out my PhD indigenous 5000 fellowships.

At last but not the least, I owe my deepest gratitude to my family including my parents, sisters and brothers, especially Mr. Muhammad Taus Jan for their encouragement and prayers which enabled me to complete this project.

Muhammad Tariq Jan

List of Publications

This thesis is based on the following publications:

1. **Tariq Jan**, J. Iqbal, M. Ismail, M. Zakaullah, S. H. Naqvi, N. Badshah, Sn doping induced enhancement in the activity of ZnO nanostructures against antibiotic resistant S. aureus bacteria, *International Journal of Nanomedicine*, (2013) 8 3679–3687. **(I.F= 4.383)**

2. **Tariq Jan**, J. Iqbal, M. Ismail, N. Badshah, Q. Mansoor, A. Arshad, Q. Ahkam, Synthesis, physical properties and antibacterial activity of metal oxides nanostructures, *Materials Science in Semiconductor Processing*, 21 (2014) 154–160. **(I.F= 1.955)**

3. **Tariq Jan**, J. Iqbal, M. Ismail, A. Mahmood, Synthesis of Highly Efficient Antibacterial Agent Ag Doped ZnO Nanorods: Structural, Raman and Optical Properties, *Journal of Applied Physics*, 115 154308 (2014). **(I.F= 2.183)**

4. **Tariq Jan**, J. Iqbal, M. Ismail, Q. Mansoor, A. Mahmood, A. Ahmad, Eradication of Multi-drug Resistant Bacteria by Ni Doped ZnO Nanorods: Structural, Raman and optical characteristics, *Applied Surface Science*, 308 (2014) 75–81. **(I.F= 2.711)**

5. **Tariq Jan**, J. Iqbal, Q. Mansoor, M. Ismail, S. H. Naqvi, A. Gul, S. F. H. Naqvi and F. Abbas, Synthesis, physical properties and antibacterial activity of Ce doped CuO: a novel nanomaterial, *J. Phys. D: Appl. Phys.* 47 (2014) 355301. **(I.F= 2.721)**

Additional publications:

6. J. Iqbal, **Tariq Jan**, Y. Ronghai, Effect of Co doping on morphology, optical and magnetic properties of ZnO 1-D nanostructures, *J Mater Sci: Mater Electron*, (2013) 24 4393–4398. **(I.F= 1.569)**

7. J. Iqbal, **Tariq Jan**, M. Shafiq, A. Arshad, N. Ahmad, S. Badshah, Y. Ronghai, Synthesis as well as Raman and optical properties of Cu-doped ZnO Nanorods prepared at low temperature, *Ceramics International*, (2014) 40 2091–2095. **(I.F= 2.605)**

8. J. Iqbal, H. Tabassum, I. Ahmad, **Tariq Jan**, C. F. Dee, M. Madhuku, A. A. Umar & N. Ahmad, Carbon Ion-beam-induced Modification in Structural and Electrical Properties of ZnO Nanowires, *Sains Malaysiana*, 43(2) (2014) 283–287. **(I.F= 0.446)**

9. J. Iqbal, **Tariq Jan**, M. Ismail, N. Ahmad, A. Arif, M. Khan, M Adil, S. Haq, A. Arshad, Influence of Mg doping level on morphology, optical, electrical properties and antibacterial activity of ZnO nanostructures, *Ceramics International*, 40 (2014) 7487–7493. **(I.F= 2.605)**

10. J. Iqbal, **Tariq Jan**, Y. Ronghai, S. H. Naqvi, I. Ahmad, Doping induced tailoring in the morphology, band-gap and ferromagnetic properties of biocompatible ZnO Nanowires, Nanorods and Nanoparticles, *Nano-Micro Letters*, 6(3) (2014) 242-251. **(I.F= 1.975)**

11. J. Iqbal, M. Rajpoot. **Tariq Jan**, I. Ahmad, Annealing Induced Enhancement in Magnetic Properties of $Co_{0.5}Zn_{0.5}Fe_2O_4$ NPs, *Journal of Superconductivity and Novel Magnetism*, 27 (2014) 1743-1749. **(I.F= 0.909)**

12. J. Iqbal, R. A. Janjua, **Tariq Jan**, Structural, optical and magnetic properties of Co-doped ZnO nanoparticles prepared via a wet chemical route, *Int. J. Mod. Phys. B*, 28 (2014) 1450158. **(I.F= 0.937)**

13. J. Iqbal, N. Safdar, **Tariq Jan**, M. Ismail, S. S. Hussain, A. Mahmood, S. Shahzad, Q. Mansoor, Facile Synthesis as well as Structural, Raman, Dielectric and Antibacterial Characteristics of Cu Doped ZnO Nanoparticles, *Journal of Material Science & Technology*, 31 (2015) 300-304. **(I.F= 1.909)**

14. F. Abbas, J. Iqbal, **Tariq Jan**, S. H. Naqvi, A. Gul, A. Mahmood, R. Abbasi, I. Ahmad, Differential Cytotoxicity of Ferromagnetic Co Doped CeO2 Nanoparticles against Human Neuroblastoma Cancer Cells, *Journal of Alloys and Compound*, 648 (2015) 1060-1066. (I.F= 2.999)

15. **Tariq Jan**, J. Iqbal, U. Farooq, A. Gul, R. Abbasi, I. Ahmad, M. Malik, Structural, Raman and optical Characteristics of Sn doped CuO Nanostructures: A novel anticancer agent, *Ceramics International*, 41 (2015) 13074-13079. (I.F= 2.605)

16. F. Abbas, **Tariq Jan**, J. Iqbal, S. H. Naqvi, Fe doping induced enhancement in room temperature ferromagnetism and selective cytotoxicity of CeO2 nanoparticles, *Current Applied Physics*, 15 (2015) 1428-1434. (I.F= 2.212)

17. F. Abbas, **Tariq Jan**, J. Iqbal, I. Ahmad, S. H. Naqvi, M. Malik, Facile synthesis of ferromagnetic Ni doped CeO2 nanoparticles with enhanced anticancer activity, *Applied Surface Science*, 357 (2015) 931-936. (I.F= 2.711)

Abstract

Metal oxides (MOs) nanostructures represent new class of materials which have been explored for various applications such as solar cells, sensors, fuel cells, microelectronic circuits, photocatalysts, antibacterial agents and piezoelectric devices due to their unique physiochemical properties. MOs nanostructures have changed or enhanced characteristics in contrast to their bulk counterparts. Various physiochemical properties of MOs nanostructures are hugely dependent on their particle size and shape. Fabrication of MOs nanostructures with strict control over the above mentioned parameters, exploration of their unique physiochemical characteristics and applications have attracted enormous interest in various fields of science and technology.

In this thesis, first of all different MOs nanostructures such as ZnO, CuO, SnO_2 and CeO_2 have been synthesized by chemical co-precipitation technique and characterized by XRD, SEM, FTIR and UV–visible spectroscopy analysis. XRD results reveal the single-phase formation of all MOs. Spherical nanoparticles are observed in case of ZnO, SnO_2 and CeO_2 samples, while hierarchal nanostructures are observed in case of CuO sample. The average particle sizes obtained from SEM images are 25 nm, 28 nm and 30 nm for ZnO, SnO_2 and CeO_2 nanostructures, respectively. The antibacterial characteristics of four different MOs nanostructures against E. coli bacterium has been assessed by agar disc method. The order of antibacterial activity for different MOs nanostructures is found to be the following: $ZnO>SnO_2>CeO_2>CuO$.

Among these, the most efficient antibacterial agent ZnO has been selected and an effort is made to tailor its various physical properties by tuning its morphology, particle size and selective chemical doping in order to enhance its antibacterial potency. Sn_xZnO_{1-x} (where x = 0, 0.02, 0.04

and 0.06) nanostructures have been prepared via co-precipitation method. The detailed study has depicted the prepared Sn_xZnO_{1-x} samples have hexagonal wurtzite structure. The shift in the main diffraction peak (101), increase in the particle size, modification in morphology, and tailoring in the excitation absorption peak with increases in Sn concentration into ZnO clearly demonstrate the successful substitution of Sn dopant into the host matrix. It is observed from the antibacterial tests that Sn doping enhances the antibacterial activity of ZnO nanostructures. It is found that shape and size of ZnO nanostructures along with the percentage Sn dopant remarkably manipulate its antibacterial potency.

In the next step, Ag_xZnO_{1-x} (where $x = 0$, 0.02 and 0.04) nanorods have been prepared via chemical route and their structural, morphological, Raman, optical properties and antibacterial activity are studied. Structural analysis has revealed that Ag doping cannot deteriorate the structure of ZnO and wurtzite phase is maintained. Scanning electron microscopy results have demonstrated the formation of ZnO nanorods. These nanorods have observed to have average diameter of 96 nm and length of 700 nm, respectively. Raman spectroscopy results suggest that the Ag doping enhances the number of defects in ZnO host matrix. It has been found from optical study that Ag doping results in positional shift of band edge absorption peak. This is attributed to the successful incorporation of Ag dopant into ZnO host matrix. The surface defects have been observed to play major role to enhance antibacterial activity of Ag doped ZnO nanorods as compared to undoped ZnO.

Moreover, Ni_xZnO_{1-x} (where $x = 0$, 0.02, 0.04 and 0.06) nanorods have been synthesized via same procedure as used for the synthesis of Ag_xZnO_{1-x} nanorods. It has been found that though Ni dopant is not able to alter the wurtzite structure of ZnO nanorods but strongly influence the length and diameter of the nanorods. Raman spectroscopy results show that the

E_l^{LO} phonons mode band shifts to the higher values with Ni doping, which is attributed to large amount of crystal defects. Ni doping is also found to tune the optical properties of ZnO nanorods. Ni doping has also greatly enhanced the antibacterial potency of ZnO nanorods.

Finally, CuO nanostructures doped with Ce at different concentration levels have been synthesized via a simple co-precipitation technique. Structural studies exhibit the presence of a monoclinic structure of CuO for Ce_xCuO_{1-x} (where x = 0, 0.02, 0.04 and 0.06) samples without any additional impurity phases. SEM images have revealed the rod-like morphology with an average diameter of 30 nm for undoped CuO. The optical band gap of CuO has been observed to be decreased with doping which is assigned to the integration of the impurity band with the conduction band of CuO. The Ce doping induced effects on the antibacterial activity of the prepared Ce_xCuO_{1-x} nanostructures have been examined by recording the growth curves of bacteria in the presence of prepared nanostructures. It has been observed that S. aureus bacterium may be completely eradicated by the use of Ce doped CuO nanostructures.

The cytotoxicity analysis of all the prepared nanostructures has shown that the synthesized nanostructures are biocompatible and non-toxic towards the human cell line SH-SY5Y cells. The bio-safe and biocompatible nature of the synthesized nanostructures along with the tunable optical properties and significant antibacterial potency make them potential for various applications in industrial, environmental and health sector.

Table of Contents

List of Figures

xix

List of Tables

Chapter No. 1

Introduction

1.1 Introduction Metal Oxides (MOs)

MOs play very critical role in many fields of science and technology such as Physics, Chemistry, Material Science and Engineering and Medicines. Metal elements are able to make chemical bond with oxygen and form oxidic compounds which can exhibit conductor, semiconductor or insulator distinctiveness. In these days, MOs are widely used in the fabrication of solar cells, sensors, fuel cells, microelectronic circuits, as a catalyst and piezoelectric devices [1-6].

Nanotechnology is an emerging and most growing field of science and technology. At nanoscale, the main goal is to fabricate nanostructure materials, which have particular and extra ordinary properties as compared to those bulk forms [7-10]. Nanostructures of MOs can demonstrate unique physical and chemical properties because of their nano scale size, high surface to volume ratio of atoms and edge effect [8-10]. The nanostructure size can influence following three major set of characteristics in any MOs;

First of all, scaling down of MOs from bulk to nanoscale influences their structural properties such as lattice parameters and its symmetry. In bulk form, most of the MOs have usually stable and dynamic crystallographic structures. However, when MOs are scaled down to nanoscale, their surface energies and stress in the lattice may increase dramatically leading to thermodynamic instability. This thermodynamic instability can induce modifications in cell parameters and structural alterations. In some cases, due to extremely high surface free energy MOs nanoparticles interact with the immediate environment and disappear completely. The

nanostructures (nanoparticles, nanowires, nanorods etc.) must have smallest amount of surface free energy to sustain structural stability. With the purpose of fulfilling this criteria, some of the phases with lower stability in bulk form transforms into highly stable phases at nanoscale. For example, Palker et al., have observed lattice distortion and enhancement in unit cell volume of CuO upon scaling it down to nanoscale from bulk because crystal symmetry leans to increase and a phase transition from low symmetry monoclinic structure of CuO to the high symmetry cubic structure with the decrease in particle size has been found [11]. Similarly, lattice expansion is also found in CeO_2 and ZnO nanostructures [12, 13].

Secondly with decreasing particle size, more and more atoms are accommodated on the surface which leads to higher surface area of MOs nanostructures. The presence of more atoms on the surface makes MOs nanostructures highly chemically reactive because more atoms are available for a chemical reaction on the surface. Study on particle size and chemical reactivity of ZnO demonstrates inverse relationship between them [14]. ZnO having smallest particle size shows maximum chemical reactivity. The particle size reduction may also lead to formation of edges (under coordinated atoms) and oxygen vacancies in metal oxides. Jonathan E. Spanier et al; studied bulk and nanostructure ceria with varying particle sizes with the help of Raman spectroscopy [15]. They observed formation and enhancement of oxygen vacancies in the crystal structure of ceria with decreasing particle size from 5 μm down to 6.1 nm.

Thirdly, at nanosacle quantum confinement effects may arise in metal oxides. These effects arise when particle size is comparable to the Bohr exciton radius of MOs. In this case, electrons in MOs can feel the presence of particle boundaries and respond by changing their energy. Quantum confinement effects lead to enhancement in excitonic transition energy and widening of MOs band gap. The idea of this effect was first introduced in 1982 in order to explain the shift

2

in the absorption peak of CuCl with decreasing particle size [16]. The relation deduced for band gap energy (E_g) of a nanoparticle having radius R was as follows;

$$E_g(R) = E_g(\infty) + \frac{\pi^2 h^2}{2\mu R^2} \qquad (1.1)$$

Where μ is the reduced mass of electron hole pair. This relation demonstrates that expansion of the E_g is arising from the kinetic energy of electron hole pair separated by distance R. This relation was further modified by the inclusion of Coulomb interaction of electron hole pair and spatial correlation energy E_R functions. The modified form after simplification is as follows [17, 18];

$$E_g(R) = E_g(\infty) + \frac{\pi^2 h^2}{2\mu R^2} - \frac{1.786 e^2}{\varepsilon_r} + 0.284 E_R \qquad (1.2)$$

This relation with inclusion of dielectric constant (ε_r) and the reduced mass (μ) functions demonstrates that E_g expansion at nanoscale is dominated by both kinetic and potential energies of electron hole pair. This theory predicts an inverse square relation between E_g and particle size R. This holds very well for some MOs such as Fe_2O_3 [19] and CdO [20] but fails for others such as ZnO, CeO_2 and SnO_2 etc [21-23] which suggests that this theory over estimates the E_g expansion. The theory was later further modified to a relation $E_g \propto R^{-n}$ (where n vary material to material) [24].

Such effects are experimentally observed in ZnO, CuO, SnO_2 and CeO_2 nanostructures [21-23, 25]. In bulk form, CuO has direct band gap energy of 1.2 eV which increases up to 2.1 eV at nanoscale. Even some researchers have reported band gap energy of 4.13 eV for CuO quantum dots having particle size of 10 nm [25].

3

1.2 Ceria (CeO$_2$)

CeO$_2$ is one the most important and abundant amongst all the rare earth MOs. It has a wide band gap (3.2 eV) and large free exciton binding energy (58 meV) at room temperature with cubic fluorite crystal structure. CeO$_2$ is only soluble in some of the strong acids while completely insoluble in water. It has capability to absorb minute quantities of water molecules and CO$_2$ from surrounding environment. Furthermore, it demonstrates high oxygen storage capability and strong absorption of ultraviolet (UV) radiations [26, 27]. Due to these tremendous properties, CeO$_2$ is vastly explored for applications in various fields such as solid oxide fuel cells, UV filters, gas sensors, antibacterial agents, targeted drug deliver, photocatalytic activities and automotive exhaust catalysts [28-32]. CeO$_2$ is also used in MOs semiconductor devises as a luminescent material and phosphor material containing both activator and hosts [33, 34]. But, the efficiency of CeO$_2$ in these applications is limited by several problems such as surface area, morphology, particle size and crystalline quality [35]. It has been discussed in the previous section that at nanoscale MOs possesses unique physiochemical properties as compared to their bulk counterparts. Hence, synthesis of CeO$_2$ nanomaterials and their applications are highly desirable.

1.3 Copper Oxide (CuO)

CuO is a narrow band gap semiconductor having monoclinic crystal structure. Being a simplest member of the copper compounds family, CuO has attracted enormous amount of interest, because of its tremendous physical properties likewise narrow band gap, spin dynamics, high temperature superconductivity and electron correlation effects [27, 28]. Furthermore, CuO is an important p-type semiconductor having diverse applications in solar energy conversion, High T$_C$ superconductors, gas sensors, lithium ion batteries and CO reduction [36]. Due to

4

narrow optical band gap, CuO is also extensively used in photocatalytic, photovoltaic and photoconductivity applications [37]. By decreasing particle size and controlling morphology of CuO, it may show changed or enhanced properties as compared to those of bulk counterpart. Moreover, CuO nanostructures with high surface area, outstanding stability, cost effective synthesis and good optical and electrical properties could effectively be used to enhance the performance of above mentioned functionalities [38].

1.4 Tin Dioxide (SnO_2)

SnO_2 is a broad band gap (3.8 eV) semiconductor having rutile type crystal structure. SnO_2 is normally regarded as oxygen deficient n-type semiconductor material. It is one of the most important MOs because of its tremendous properties such as low electrical resistance, highly transparent in visible range of electromagnetic spectrum, wide energy band gap, chemical and mechanical stability and sensitivity towards variety of gases [39, 40]. SnO_2 is widely used in MOs based gas sensors, photo-catalysis, as an anode material in lithium ion batteries bulk ceramics, pigments and transparent electrodes [41-45]. On the other hand, mostly physiochemical properties of SnO_2 material depends various structural parameters such as particle size and aspect ratio. For example performance of SnO_2 based gas sensors strongly depends on these parameters [46]. Similarly, photocatalytic and antibacterial activity of SnO_2 is also critically dependent on particle size [47]. Various research groups suggested that specific surface of SnO_2 could be enhanced remarkably by bringing it to down to nanoscale [48]. Hence, it is highly demanding to develop an easy approach for the synthesis of SnO_2 nanomaterials and thereafter its applications.

1.5 Zinc Oxide (ZnO)

5

ZnO is most common and widely studied material in the field of science and technology due to its unique properties; such as wide band gap energy (3.37 eV), electrical and thermal stability, large exciton binding energy (60 meV), biocompatibility and biosafety [41]. ZnO crystallizes in stable wurtzite structure having lattice constants a (3.25 Å) and c (5.21 Å). Due to these tremendous properties ZnO nanostructures are widely used in electronic and optoelectronic devices, sensors, solar cells, antibacterial coating, UV protectors and targeted drug delivery [49-53]. As main focus of the thesis is on ZnO, so it will be discussed in detail.

1.5.1 Structure

ZnO crystallizes in three different crystal structures; zinc blende, rock salt and wurtzite depending on conditions provided for crystallization. All the three crystal structures are illustrated in figure 1.1. The most thermodynamically stable crystal structure for ZnO is wurtzite under ambient conditions [54]. Zinc blende structure of ZnO could be obtained by growing it on cubic crystal surface, while rock salt structure could only be achieved under high pressure environment [55].
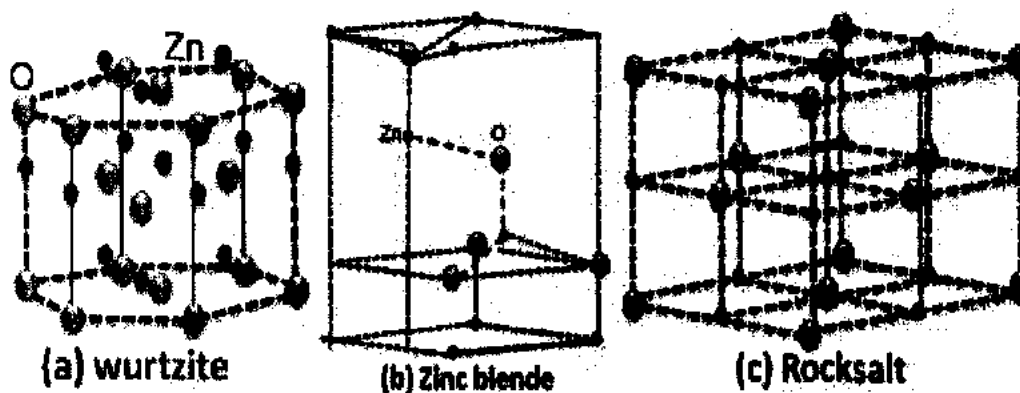
Figure 1.1 Different crystal structures of ZnO [56]

ZnO usually crystallizes in wurtzite crystal structure having lattice constants a = b = 3.25 Å and c = 5.12 Å. The ionic bonding between zinc (Zn) and oxygen (O) is possible due to the huge difference of the electronegativities of Zn (1.65) and O (3.44). In wurtzite crystal structure, number of Zn and O surfaces is stacked alternatively along the c-axis. Each Zn atom is tetrahedrally coordinated to four O atoms as shown in figure 1.1 (a). ZnO wurtzite crystal consists of both polar and non polar surfaces. The cations (Zn^{2+}) and anions (O^{2-}) can take such a configuration that some of the surfaces are completely terminated with Zn^{2+} or O^{2-} giving the positively or negatively charged surfaces, respectively. And the resulting charged surfaces are known as polar surfaces [56]. The electric charges on these polar surfaces are fixed, which cannot be transferred or altered. The interactions of these charges depend on their distribution over the surfaces. The structure of the ZnO is arranged in such a configuration that it maintains minimum electrostatic energy. The polar surfaces control the various physiochemical properties of ZnO. ZnO wurtzite crystal also has non polar surfaces comprising same number of Zn^{2+} and O^{2-} ions. Non polar surfaces of ZnO generally have lower surface energies than polar surfaces. Paticle size and shape of ZnO nanostructures can be tailored by varying the growth rate along polar and non polar surfaces.

1.5.2 Physical properties of ZnO

Some of the basic physical properties of bulk ZnO are summed up in table 1.1. Various physical properties of ZnO change significantly at nano scale due to significant enhancement in the surface area, dominant quantum confinement effects and higher surface states etc. For example lattice expansion and contraction with variation in particle size has been reported previously and attributed this to variation in electrostatic forces due to surface dipoles [12]. Furthermore, lattice constant values approach to that standard bulk values as particle size increase [57]. Similarly, optical band gap energy of ZnO nanostructures varies from 3.4 eV to

3.6 eV depending on particle size which is higher than that of bulk ZnO value of 3.37 eV [58]. This widening of the band gap may be understood quantum confinement effects perspectiveas discussed earlier in section 1.1. Particle size also influences the refractive index of ZnO due to the decrement in compactness and crystalline quality of nanostructures as compared to their bulk counterparts [59]. Furthermore, refractive index is also related with band gap energy of ZnO therefore variation band gap energy as a function particle size will lead to variation in refractive index values [60]. Electrical characteristics of nano ZnO such as electron mobility and concentration may vary from that of bulk counterparts due to their surface area and presence of oxygen vacancies on the surface which may react with atmospheric molecules and change their electric response [61].

Table 1.1: Basic physical properties of wurtzite ZnO at room temperature [62-64]

Lattice constants	a = b = 3.2Å, c = 5.2Å
Melting point	1977 °C
Dielectric constant	8.6
Optical band gap energy	3.37 eV
Exciton binding energy	60 meV
Electron mobility	210 cm^2/Vs
Refractive index	2.02
Molecular mass	81.39 g/mol

1.5.3 Vibrational properties of ZnO

The exact knowledge of the vibrational properties of ZnO is essential for understanding of its various physical properties. Various techniques such as Raman and infrared (IR) spectroscopy are being utilized for long time to analyze the vibrational properties of ZnO [65-68]. ZnO crystal has different vibrational modes i.e. Raman active modes, IR active modes and optically inactive modes. Wurtzite ZnO crystal has 4 atoms per unit cell i.e. s = 4 and hence 12 total phonon modes (Total modes = 3s) [56]. ZnO has 1 and 2 longitudinal acoustic (LA) and transverse acoustic (TA) modes, respectively. Furthermore, wurtzite ZnO crystal has 6 transverse optical (TO) and 3 longitudinal optical (LO) phonon modes. Raman and IR spectroscopy are usually being used to probe the some zone boundary and zone center phonon modes of ZnO crystal. The group theory foresees 8 set of phonon modes i.e. $2A_1 + 2E_1 + 2B_1 + 2E_2$ for wurtzite structure of ZnO. One A_1 and one E_1 modes are acoustic modes whereas the remaining 6 are optical modes. The typical Raman spectra of bulk ZnO at room temperature are shown in figure 1.2. In this figure, the solid lines represent first order phonon modes of ZnO while dashed lines represent vibrational modes featured due to the multiple phonon scattering processes.
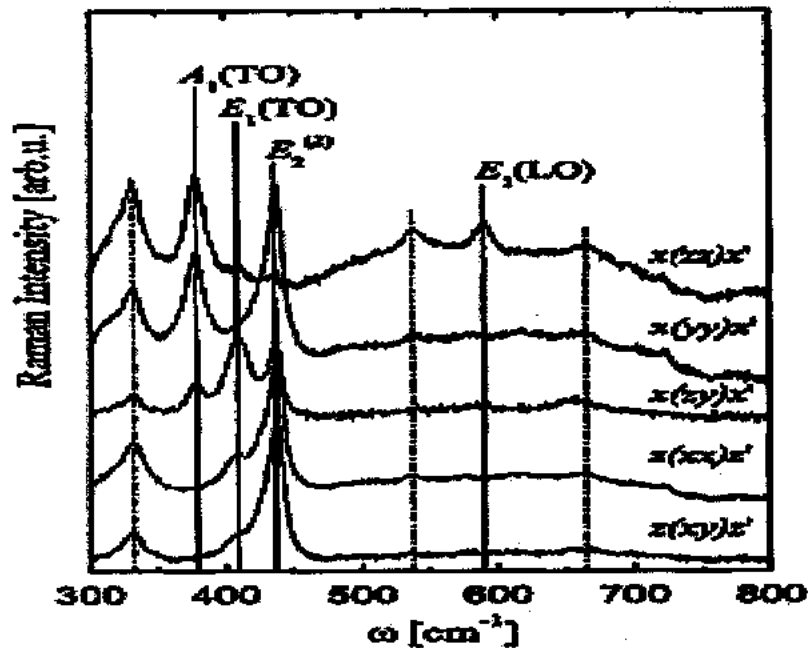
Figure 1.2 Typical Raman spectra of bulk ZnO obtained at room temperature [69]

The vibrational modes of ZnO are extremely sensitive to dopants, defects (such as Zn interstitial and oxygen vacancies etc) and strain [70]. Various authors have reported shift in the Raman modes at nanoscale which is attributed to defects creation [71]. Hence, important information about ZnO nanostructures can be extracted from the analysis of the position and broadening of the Raman and IR peaks.

1.5.4 Optical properties of ZnO

ZnO is a direct wide band gap (3.37 eV) semiconductor which makes it potential material for photonics applications. ZnO also has large exciton binding energy (60 meV) which can ensure efficient excitonic emission at room temperature. Thus, optical properties of ZnO are of immense interest for exploring its potential applications. Optical properties of ZnO are widely investigated through various techniques likewise; ultraviolet (UV)-visible absorption

spectroscopy, photoluminescence spectroscopy and cathode-luminescence spectroscopy etc. The optical properties of ZnO can be originated due to both intrinsic and extrinsic effects. When optical transitions are triggered between electrons in the conduction band and holes in the valance band then such transitions are known as intrinsic optical transitions. Intrinsic optical transitions also include excitonic effects due to coulomb effects. The excitons may be categorized into two groups i.e. free excitons and bound excitons. Bound excitons are normally linked with dopants and defects which govern the extrinsic optical transitions. The dopants and defects can generate extra discrete energy states in the ZnO band gap, which strongly affect the optical properties of ZnO. These defects are categorized into two major groups: intrinsic defects and extrinsic defects. The intrinsic defects are related to crystal imperfection involving only the cations and anions. The intrinsic defects are further divided into groups i.e. the Franklin defects and the Schottky defects. The defects created when an anion or cation is removed from its native site and pushed into interstitial sites are called the Franklin defects. But the defects created when an anion or cation is completely removed from its native site leaving a vacancy are called the Schottky defects. The extrinsic defects are those which are created by impurities and dopants. Both intrinsic and extrinsic defects play vital role in controlling the optical characteristics of ZnO. Overall, the optical characteristics of ZnO depend on particle size and dimensions, defects concentrations and impurity doping [72]. Hence, optical properties of ZnO nanostructures can be significantly tuned via modifying these parameters.

1.6 Doping Induced Effects on the MOs

Different applications of MOs demand their different physiochemical properties. The doping is an easiest approach to tune the different physiochemical properties of MOs according to the needs. Commonly, different elements as a dopant in MOs can be categorized into two

groups: 1) cation dopants and 2) anion dopants. The cation dopants substitute for metal ions while anion dopants replace oxygen ions. The discussion will be centered on cation dopants and their effects on the properties of MOs as anion dopants are not often used.

In stoichiometric solid solutions, the excess charge of the dopant is compensated by lattice defects of opposite charge in order to have bulk charge neutrality. While in non stoichiometric solid solutions, it is compensated by electronic defects. The dopants may be characterized into two groups based on their charges. If the charge on the dopants is less than the host cation, then they are known as acceptor dopants. But they are known as donor dopants if their charge is greater than host cation.

If the dopant has an extra negative charge then either cation interstitial or oxygen vacancies defects will compensate for the extra charge as shown the equation below:

$$M_2O \rightarrow M'_N + M'_I + O_N \qquad (1.3)$$

$$M_2O \rightarrow 2M'_N + O_N + V^{\cdot\cdot}_A \qquad (1.4)$$
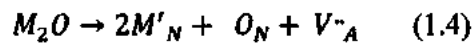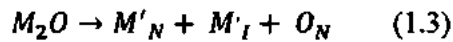
In the above equations, M_2O represents divalent metal oxide, M'_N is metal ion at native sites, $M^{\cdot}_I$ shows metal ions at interstitial sites, O_N represent oxygen ions at native sites and $V^{\cdot\cdot}_A$ are the oxygen vacancies. The number of host cations are much larger as compared to dopant cations, therefore the interstitial cations may be the host cations in equation 1.3. This equation depicts the scenario where anions sites are completely filled while cations sites are over filled. It is demonstrated in equation 1.4 that cations sites are completely occupied while anions sites partially occupied. Any of the two cases may be case in doped MOs to compensate the extra charge. The choice of utilization may be determined by size of ionic radii and charge. It is worth mentioning that mass, charge and lattice sites are perfectly conserved in these equations.

12

Similarly, the extra positive charge of the dopant is compensated either by metal ions vacancies or oxygen interstitials as illustrated in the equations 1.3 and 1.4.

$$M_2O_3 \rightarrow 2M'_N + O_N + O''_I \quad (1.5)$$

$$M_2O_3 \rightarrow 2M'_N + V^{\cdot\cdot}_A + 3O_N \quad (1.6)$$
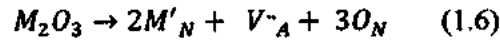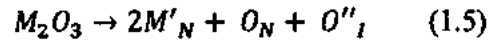
Here, $V^{\cdot\cdot}_I$ represents oxygen interstitial and $V^{\cdot\cdot}_A$ represent metal ions vacancies. Equation 1.5 depicts the situation of perfectly filled cations sites and overfilled anions sites. Equation 1.6 demonstrates the scenario of imperfectly filled cations sub-lattice and perfectly filled anions sub-lattice. The mass, charge and number of lattice sites are also conserved in these equations. The type of defects produced by dopant ions strictly depends on size of ionic radii and charge on it.

1.7 MOs Band Gap Tuning via Doping

Band gap energies of MOs are of immense interest in various applications such as optoelectronic devices, solar cells and photo-catalysis etc. The performance of these devices can be remarkably improved via successful band gap tuning. In photo-degradation of multi-drug resistant bacteria, the activation energy range of MOs is of utmost importance. Activation energies of MOs and their light absorption capabilities play a vital role in controlling their photo-degradation capabilities. Hence, controlling these two parameters may lead to higher bactericidal potency of MOs nanostructures. Selective chemical doping is believed to the easiest, efficient and versatile method for this purpose. In undoped MOs, band gap is defined as the energy required to excite an electron from valance band (VB) to conduction band (CB) as shown in figure 1.3 (a). Doping of impurities in MOs can lead to either shrinking or widening of the band gap. The band gap widening can be explained on the basis of Burstein Moss (BM) shift [73]. According to BM shift theory, donor electrons from doped impurities can occupy the states at bottom of conduction

13

band. Therefore, optical transition are vertical and the band gap is defined as the energy difference between the states with Fermi momentum in CB and VB as Pauli exclusion principle prevents the electron form doubly occupying the states in CB. This leads to widening of band gap as illustrated in figure 1.3 (b). Secondly, doping can lead to formation of impurity sates close to the VB which leads to its expansion as shown in figure 1.3 (c). The expansion of VB shrinks the optical band gap of semiconductors.
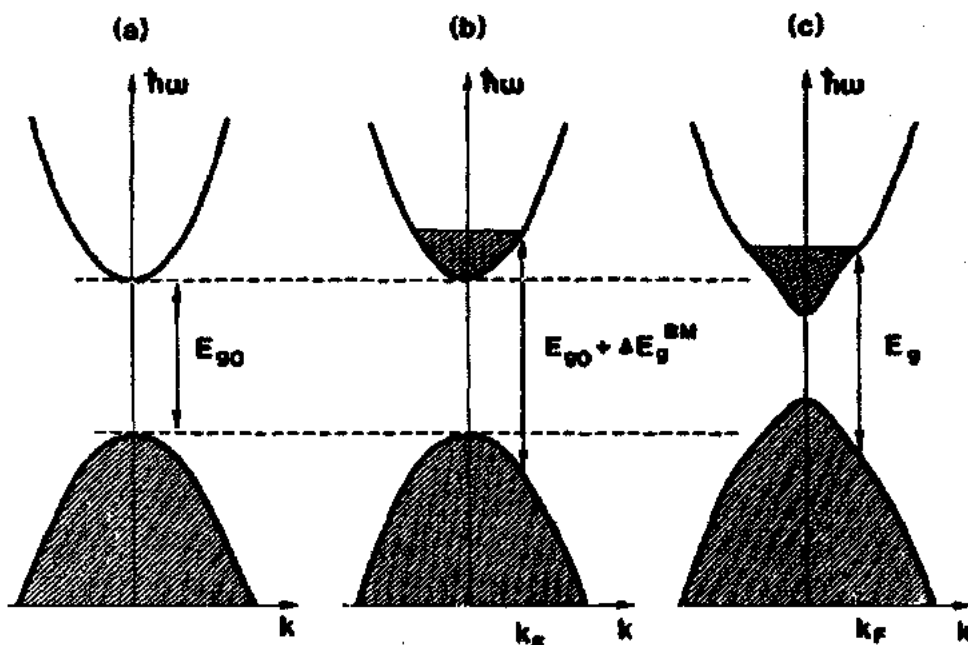
Figure 1.3 Schematic band gap representation of (a) undoped semiconductors, (b) widening of band gap and (c) shrinking of band gap [73]

There are some other explanations for band gap tuning via doping such as sp-d exchange interactions, quantum confinement effects depending the type of host and dopant and variation particle size with doping. Furthermore, concentration of doping impurities is also important to determine that which phenomenon will be effective.

14

1.8 Antibacterial Activity of MOs Nanostructures

Antibacterial agents are those materials which have toxic nature towards bacteria but do not affect the surrounding healthy cells. They are characterized into two groups 1) those agents which kill bacteria are known as bactericidal agents 2) and those antibacterial agents which only slows down or inhibit the growth rate of bacteria are called bacteriostatic agents. Both types of antibacterial agents are of great interest in several industries, such as hospital implants, medicine, food packaging and preservation, textile fabrics and water disinfection [74, 75]. Traditionally, organic compounds are used for disinfection. But, the use of organic compounds poses various disadvantages such as toxicity towards healthy cells and low chemical and physical stability especially at high temperatures and pressure [75]. Furthermore, life threatening infections causing antibiotic resistant bacteria have emerged due to extensive use and abuse of antibiotics in the last two decades [76]. Among these, *E. coli, S. aureus* and *Pseudomonas aeruginosa* are the multi-drug resistant common species that can cause wide variety of infections and diseases [77, 78]. Mortality and morbidity linked with these bacteria remain high regardless of antimicrobial therapy, partially because these species develop resistance capability to antibiotics. Therefore new strategies are highly desired to identify and develop new generation of agents against these species.

In this context, inorganic nanostructures have shown great potential because of their excellent catalytic, optical and antibacterial characteristics [79]. Silver nanomaterial is the most studied antibacterial agent having remarkable antibacterial activity against wide range of bacteria. But, cytotoxicity of silver nanomaterial limits its application as an antibacterial agent [80]. Now, another option is to explore inorganic metal oxides nanostructures, such as TiO_2, ZnO, CuO, SiO_2, SnO_2, MgO and CeO_2 have shown significant antibacterial activities [79-85].

15

The exact mechanisms of action of MOs nanostructures toxicity towards various bacteria are still debatable. Several mechanisms of action are proposed such as ability of nanostructures to electrostatically attach to the bacteria membrane which can disturb the membrane integrity [79]. Secondly, the release of metal ions in water suspension of MOs nanostructures, these ions react lethally with bacteria [85]. Third and the most important mechanism of action is the photoactivation of MOs nanostructures and release of reactive oxygen species (ROS) [86-88]. These mechanisms of action for the toxicity of MOs nanostructures towards bacteria are shown in figure 1.4.
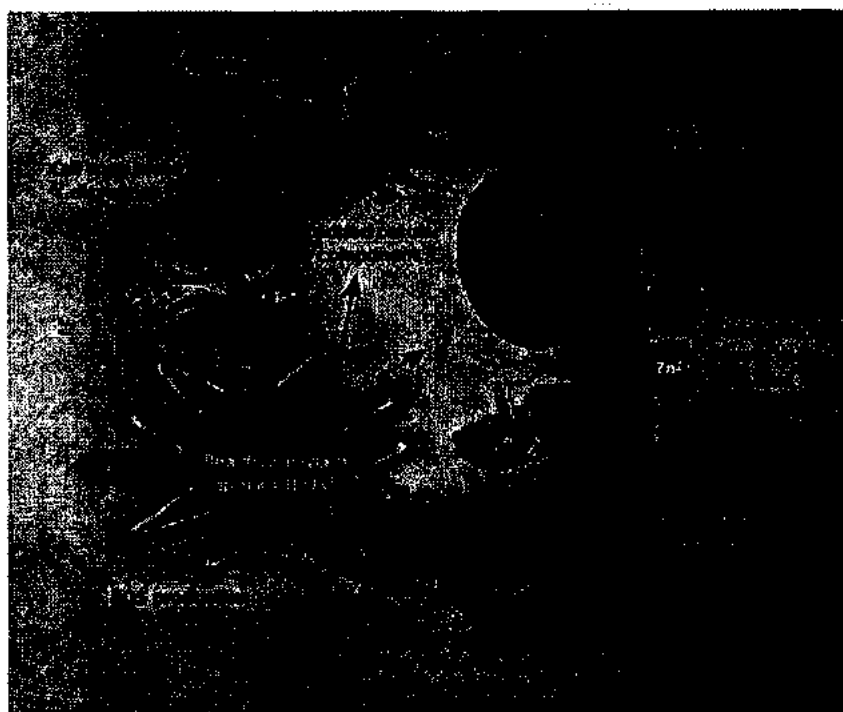
Figure 1.4 Mechanisms of action for the toxicity of MOs nanostructures towards bacteria [89].

1.9 Statement of Problem

The development of nanotechnology based devices has recently become one of the most emerging fields of research in the physical sciences. Enhancing the surface area exclusive of alteration in the size of the device dimension show the way to extra efficient devices based on surface controlled phenomena such as in solar cells, sensors, detectors, targeted drug delivery, antibacterial agents and photocatalysis. Numerous research groups have developed techniques that utilize metal oxide nanostructures to fabricate these devices. However, the effective and large scale exploitation of nanotechnology is mostly held up by the at variance demands for strict control over size, shape, morphology, their physical properties and low-cost mass production. Due to this reason it is highly demanding to build up new approaches for the fabrication of nanostructures with desired characteristics. These approaches must be efficient, cost effective and easily reproducible. Soft chemical routes are; low cost, fast and versatile methods which can be employed for the fabrication of MOs nanostructures. Furthermore, the different properties of the MOs nanostructures need to be tailored according to the demands.

Despite multiple research approaches, the bacterial contamination and related infections is serious issue worldwide. This demands development of new novel antibacterial agents having selective toxicity towards various bacteria. In this regard, numbers of MOs nanostructures such as TiO_2, ZnO, CuO, SiO_2, SnO_2 and MgO have shown great potential due to their toxic nature towards bacteria without harming healthy cells. But their antibacterial activities are still very low which needs to be enhanced.

1.10 Aims and Objectives of the Thesis

➤ Synthesis of MOs nanostructures with controlled particle size and morphology by a simple, cost effective and easily reproducible technique.

17

- Optimization of different synthesis parameters (such as reaction temperature, reactants, molarities etc.) in order to get ultrafine nanostructures.

- Investigating the morphological, structural, optical, and vibrational properties of the MOs nanostructures.

- Determination of the antibacterial activity of these MOs nanostructures.

- Selection of the best suitable MOs nanostructures regarding their antibacterial potency against *E. coli, S. aureus* and *Pseudomonas aeruginosa*.

- Tailoring of physical properties of the selected MOs nanostructures by selective metal doping to enhance their antibacterial activity.

Chapter No. 2

Synthesis and Characterization Techniques

2.1 Nanoscience and Nanotechnology

Nanoscience and nanotechnology can be defined as the science and technology of designing, synthesis and applications of materials at nanoscale as well as understanding of their physical characteristics. Nanomaterials are those materials which have at least one dimension less than 100 nm. Nanomaterials have found number of applications in various systems such as chemical, physical and biological due to their enhanced or changed physiochemical properties as compared to their bulk counterparts. These new or enhanced properties of nanomaterials are attributed to their lesser particle sizes. When the particle sizes of materials decreases their surface area (surface to volume ratio) increases [75]. It means that with the reduction in the particle sizes more and more percentage of atoms are accommodated on the surface as shown in figure 2.1. The increased percentage of surface atoms affects the structural, morphological, optical, thermal, electrical and chemical properties of the materials.
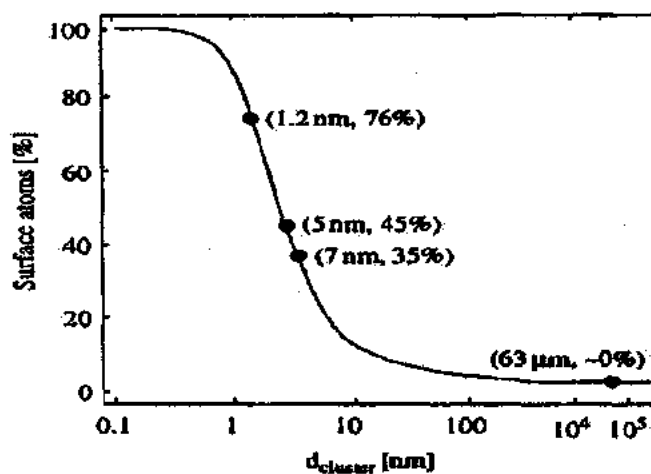
Figure 2.1 Variation of surface atoms percentage with the particle size [90]

19

2.2 Synthesis Techniques

The development of versatile synthesis techniques is essential for the exploration of the physical characteristics and realization of the nanomaterials applications. There are two approaches for the preparation of nanomaterials i.e. top-down and bottom-up approaches. Both types of approaches are illustrated in figure 2.2.
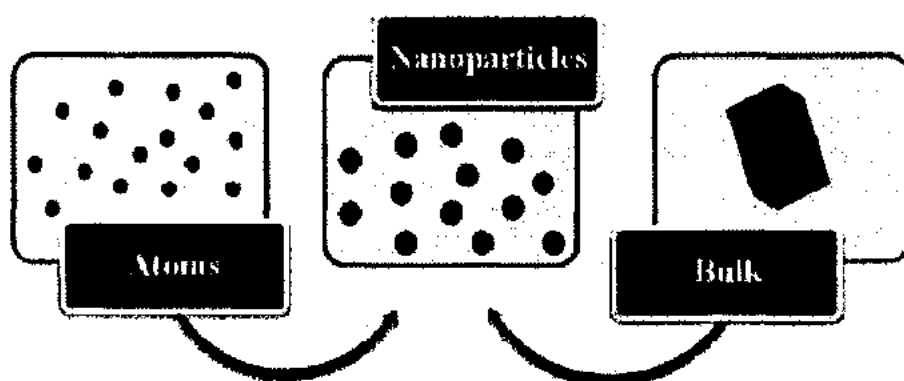
Figure 2.2 Schematic illustration of the top-down and bottom-up approaches

A top-down approach is a way to synthesize the nanomaterials by breaking/slicing bulk materials down to nanoscale. Top-down approach is just similar to manufacturing of integrated circuits in which the constituents of the system are fabricated like carving. There are many synthesis techniques for fabrication of nanomaterials based on the top-down approach, such as; lithography process (photolithography, ion beam lithography and electron beam lithography), ball milling method, embossing, molding, printing and skiving. The top down approach combines both conventional and unconventional methods to generate nanoscale materials in a way similar to "carving" smaller objects from a large bulk material. Bottom-up approach is the inverse of top down i.e. fabrication of nanomaterials from the bottom atom by atom or molecule

20

by molecule. Some examples of the bottom-up approach for synthesizing nanomaterials are chemical co-precipitation method, sol gel method, thermal evaporation method, carbothermal method, solvothermal method, hydrothermal method, physical vapor deposition (PVD) and chemical vapor deposition (CVD) methods [90].

MOs nanostructures have attracted wide variety of applications in field of science and technology such as lithium ion batteries, fuel cells, electronics, photovoltaics, magnetic storage devices, sensors, cancer therapy, and antibacterial agents [10]. However, for successful applications of MOs nanostructures, strict control over their size and morphology is essential. Also developing synthesis techniques, which are versatile, easy to handle, cost effective and reproducible is of core importance. Several routes have been adopted for synthesis of MOs nanostructures such as sol-gel method, hydrothermal method, combustion route, ball milling, and co-precipitation method [91-94]. The chemical methods based on bottom-up approach have an edge over the top-down approach in many ways. For example it gives better control over the particle size distribution and morphologies. Moreover, the stoichiometry of the MOs nanostructures can be controlled in a precise way by adopting chemical routes.

Among these, the chemical co-precipitation technique is the most useful and easiest way for the synthesis of MOs nanostructures. In this method, the salt precursors (Chloride, Nitrate, etc.) are dissolved into the distilled water (or other solvent). The precipitates such as oxo-hydroxides are formed with the help of a base agent such as a NaOH, KOH or NH$_4$OH. Most of time, the controlled size and chemical homogeneity are difficult to achieve in the case of mixed MOs. However, the use of surfactants and optimization of various synthesis parameters such as Precursors concentration and pH value are seen to be effective in controlling size and chemical homogeneity of the MOs nanostructures. General synthesis procedure for MOs nanostructures

21

preparation is illustrated in flow chart shown in figure 2.3. The synthesized samples were annealed at 300 °C to get high crystal quality MOs nanostructures. The un-annealed nanostructures were observed to have some extra phases related to metal hydroxides and poor crystalline nature. The annealing temperature was chosen to be 300 °C because at this temperature phase purity and good crystalline quality was achieved. This enhancement in the crystalline quality of MOs nanostructures may assigned to the fact that at higher temperatures, the crystallites have gained enough energy to orient themselves in proper equilibrium sites.
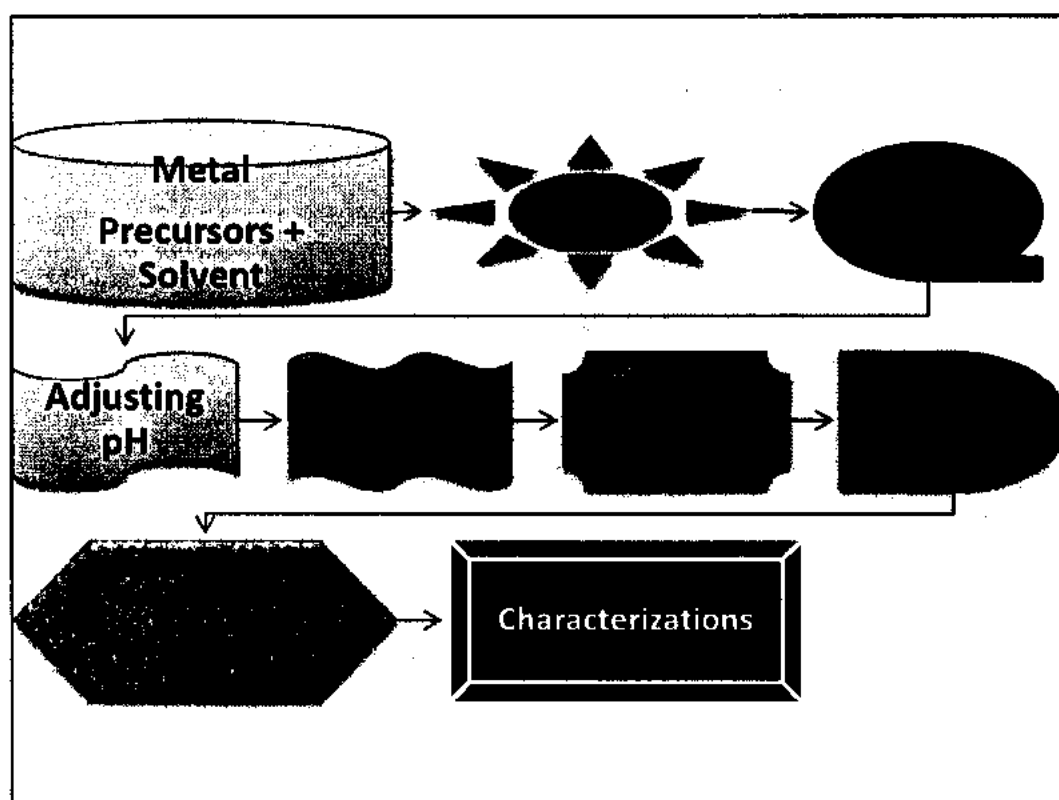
Figure 2.3 Schematic representation of synthesis procedure

2.3 Optimization of synthesis parameters

22

In this thesis, different synthesis parameters were optimized to control the phase purity, particle size and shape of MOs nanostructures which are discussed here briefly.

2.3.1 Reaction temperature

Here, experimental procedure for the synthesis of MOs nanostructures was carried out at different reaction temperatures. Figure 2.4 depicts the XRD patterns of ZnO and CuO samples prepared at room temperature and 90 °C. It is clear from this figure that at room temperature, the wurtzite and monoclinic structures of ZnO and CuO are mixed with other phases while single phases have been observed at 90 °C. This suggests that reaction temperature plays vital in the growth of MOs nanostructures. The presence of secondary phases in the samples synthesized at room temperature may be understood on the fact that decomposition of metal salts and their hydroxide complexes formed after the reaction of metal ions with OH⁻ were not complete. Moreover, crystalline quality was observed to improve at higher temperature as depicted from the higher intensities of diffraction peaks. This optimized reaction temperature was used for the synthesis of all samples.
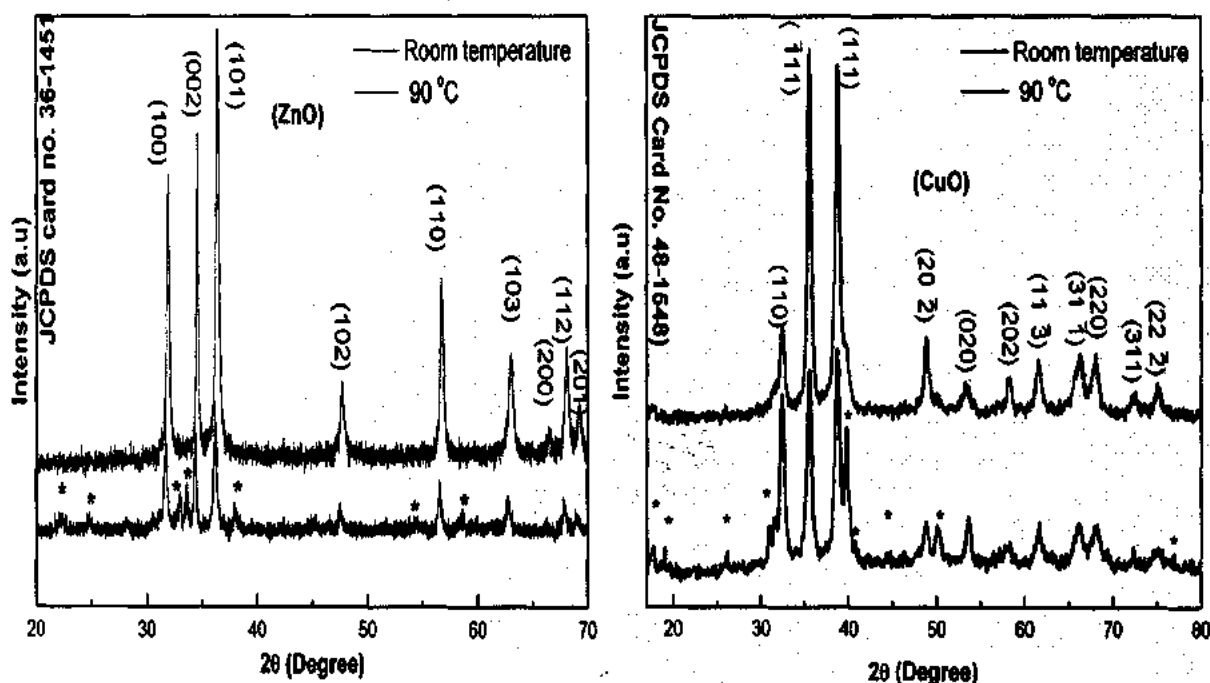
Figure 2.4 XRD patterns of ZnO and CuO prepared at different reaction temperatures

2.3.2 Role of pH

The pH of solution is very important in the synthesis of MOs nanostructures. According to the growth mechanism, when metal salts are dissolved in water they undergo decomposition and form metal ions which react with OH^- ions in the solution which are generated from the decomposition of NaOH to form metal hydroxide complexes. NaOH has been used in these experiments to adjust the pH values. Proper pH value ensures the adequate amount of OH^- ions in the solution which is necessary for super-saturation which leads to nucleation of metal ions. Hence, optimization of pH value is of utmost importance in the growth of MOs nanostructures. In these experiments, pH value has been optimized for the synthesis of different MOs nanostructures.

2.3.3 Role of acetic acid

Surfactants or capping agents may be added to the solutions in order to modify the shape and particle size of the MOs nanostructures. In this thesis, acetic acid (CH_3COOH) has been used as a surfactant. Adding CH_3COOH in water leads generation of CH_3COO^- ions which can bind to the different surfaces of MOs and modify their growth rate and orientation. Figure 2.5 (a-c) depicts the SEM micrographs of ZnO nanostructures prepared at various percentages of CH_3COOH added with respect to solvent. It can be seen from figure 2.5 (a) that without the addition of CH_3COOH, the large size particles are formed. The particle size reduces with addition of 1% CH_3COOH as shown figure 2.5 (b). Higher concentration of surfactant leads to growth of one-dimensional nanostructures. This may be attributed to the enhancement in nucleation rate of MOs upon addition of CH_3COOH. Fast nucleation leads to of formation of small nanoparticles. At higher concentration, CH_3COOH may improve the growth of ZnO along

[0001] direction as ZnO have higher growth rate along this direction if suitable conditions are provided.
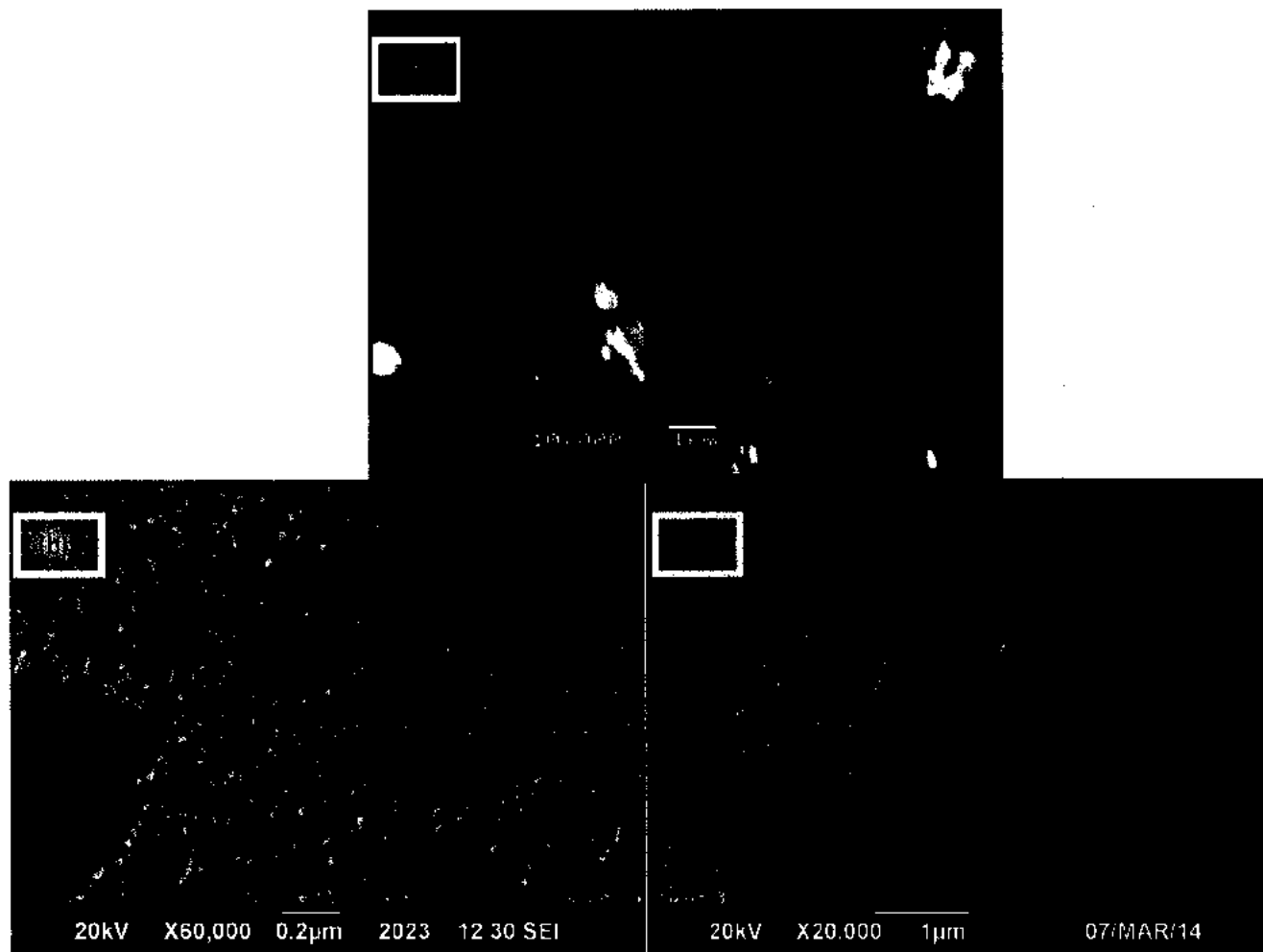
Figure 2.5 SEM images of ZnO nanostructures grown with (a) 0%, (b) 1% and (c) 2% acetic acid concentration

2.4 Crystal growth mechanism of MOs nanostructures

In this thesis, four different MOs were studied but here only growth mechanism of ZnO nanostructures is discussed. In general, crystal growth mechanism of ZnO nanostructures can be controlled through the combination of internal chemistry, external factors (supper-saturation,

reaction temperature and surfactants) and structural components [95]. ZnO is an amphoteric oxide with isoelectric point value of 9.5 which means that ZnO can be crystallized from the hydrolysis of Zn salts in basic solutions [96]. Zn^{2+} ions are known to coordinate in tetrahedral complexes and it is colourless with zero crystal field stabilization energy due to its 3d electronic configuration. When Zn salts are dissolved in solvents, Zn^{2+} ions are produced in the solution. OH^- ions are provided by the addition of alkaline solutions such as NaOH or KOH. Zn^{2+} and OH^- ions can form different intermediates depending on pH and reaction temperature. The addition of alkaline solutions is necessary for the formation of ZnO as usually divalent metal ions are not able to hydrolyze in acidic atmosphere [97]. ZnO can be achieved from these intermediates via dehydration. The chemical reactions for the formation of intermediates are as follows;

$$Zn^{2+} + 2OH^- \leftrightarrow Zn(OH)_2 \qquad (2.1)$$

$$Zn(OH)_2 + 2OH^- \leftrightarrow [Zn(OH)_4]^{2-} \qquad (2.2)$$

$$[Zn(OH)_4]^{2-} \leftrightarrow ZnO_2^{2-} + 2H_2O \qquad (2.3)$$

$$ZnO_2^{2-} + 2H_2O \leftrightarrow ZnO + 2OH^- \qquad (2.4)$$

$$ZnO + 2OH^- \leftrightarrow ZnOOH^- \qquad (2.5)$$
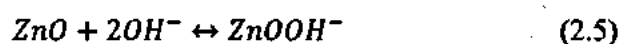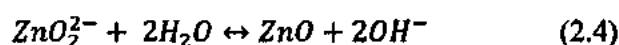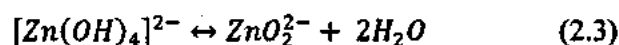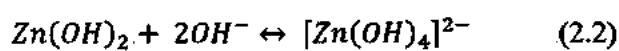
These chemical relations illustrate the main reactions involved in the growth of ZnO nanostructures. The end product in 2.2 may not be the same all the time. It may vary depending on pH value of the solution as demonstrated in figure 2.6. The dotted lines in this figure depict the thermodynamic equilibrium between Zn^{2+} soluble species and corresponding solid phases.

26

This demonstrates the importance of pH value of the solution for the growth of MOs nanostructures.
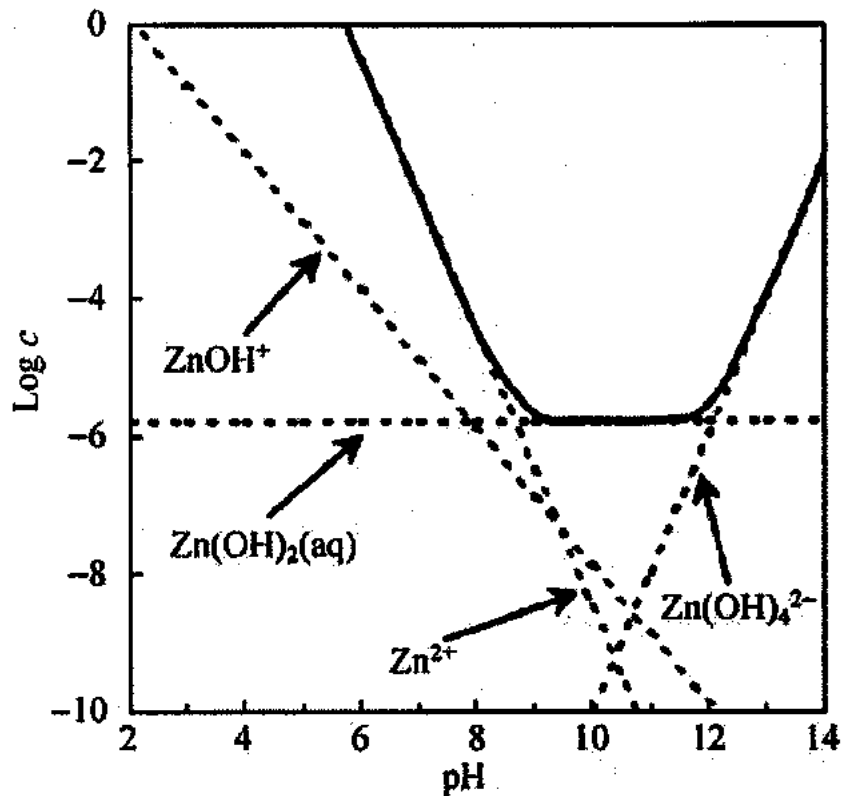
Figure 2.6 Phase stability diagrams for the $ZnO_{(s)}$–H_2O system [98]

Initially, the Zn^{2+} and OH^- ions interact with each other and then undergo dehydration by proton transfer, forming the metal hydroxide complexes as depicted in relation 2.2 with octahedral geometry. These complexes act as growth units for the nucleation of ZnO. The water molecules produced during the chemical reactions diffuse to the solution. When the growth units reach supersaturated values, wurtzite ZnO starts to nucleate at the central region of aggregates as shown in figure 2.7.

27
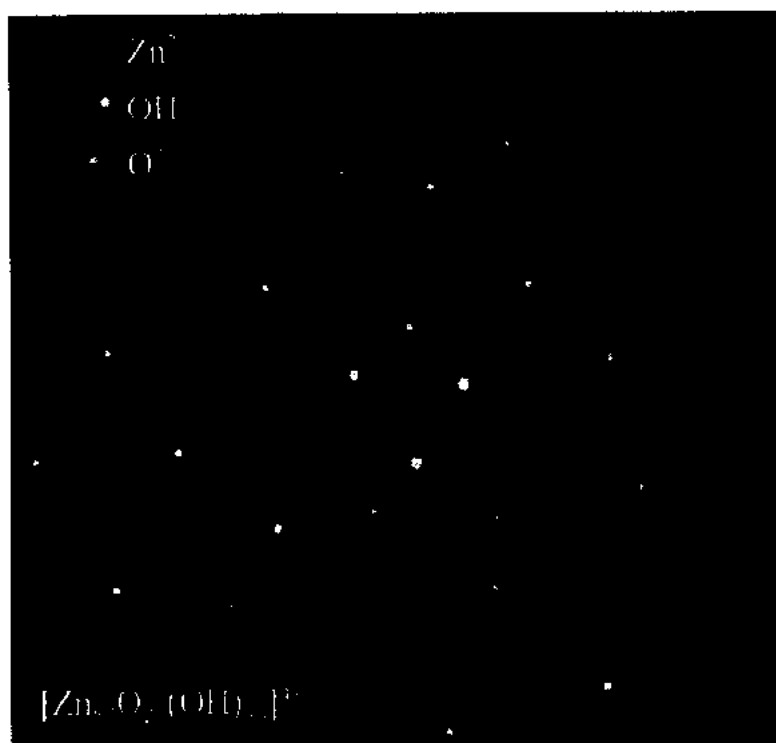
Figure 2.7 Nucleation of ZnO [99]

The core of the aggregates is comprised of Zn^{2+} and O^{2-} surrounded by Zn^{2+} and OH^-. The size of the nanostructures can be controlled by controlling the nucleation rate.

2.5 Synthesis procedures

2.5.1 Synthesis of MOs nanostructures

The chemicals used for synthesis of MO nanostructures were zinc chloride ($ZnCl_2$), copper chloride ($CuCl_2$-$5H_2O$), stannous chloride ($SnCl_4$-$5H_2O$), cerium nitrate ($CeNO_3$-$6H_2O$), sodium hydroxide (NaOH) and acetic acid (CH_3COOH). All MOs samples were synthesized via chemical co-precipitation technique using distilled water as a solvent. For synthesis of MOs nanostructures, 0.1M solution of all metal precursors were prepared in distilled water and stirred up to 20 minutes for complete dissolution. CH_3COOH was added as surfactant and again stirred

for 20 minutes. The pH values of the solutions were adjusted at 8 via drop-wise addition of 1M NaOH solution. After adjusting the pH value, solution was stirred for one hour. Finally, precipitates were collected and washed via centrifugation. The cleaned precipitates were dried in an electric oven for 12 hours at 80°C and then grinded with help of mortar and pestle to acquire the powder. Finally, the prepared MOs samples were annealed at 300 °C for 2 hrs to enhance their crystallinity.

2.5.2 Synthesis of Sn_xZnO_{1-x} nanostructures

For synthesis of Sn_xZnO_{1-x} nanostructures, $ZnCl_2$, $SnCl_4$-$5H_2O$ and NaOH were used. The synthesis was performed by a simple co-precipitation technique by using distilled water as a solvent. For synthesis of undoped ZnO nanostructures, 0.1M solution of $ZnCl_2$ in distilled water was stirred up to 20 minutes for complete dissolution. Then 1M NaOH solution was added drop-wise to adjust the pH value at approximately 8. After adjusting the pH value, solution was stirred for one hour. Precipitates are collected from the solution by centrifugation. For Sn doping, the same procedure was adopted except the addition of $SnCl_4$-$5H_2O$ with various molar ratios to $ZnCl_2$ for 2, 4 and 6% Sn doping. All samples were dried in an oven for 5 hours at 80°C and then grinded with help of mortar and pestle to acquire the powder. The samples were annealed in a chamber furnace for 2 hours at 600°C.

2.5.3 Synthesis of Ag_xZnO_{1-x} nanorods

Ag_xZnO_{1-x} nanorods were prepared by chemical co-precipitation technique using zinc chloride ($ZnCl_2$), silver nitrate ($AgNO_3$), sodium hydroxide (NaOH) and acetic acid (CH_3COOH). For synthesis of Ag_xZnO_{1-x} nanorods, acetic acid concentration was doubled as compared to that used for synthesis of ZnO nanoparticles in MOs chapter. This increase in concentration of acetic acid lead to the formation of rod-like shape of nanostructures. A quantity of 0.1M $ZnCl_2$ solution was prepared in 100 ml distilled water at 80 °C and in the meantime

acetic acid was added to this solution. Then 1M NaOH solution was added drop-wise to adjust the pH value at approximately 8. After the addition of NaOH, parent solution was vigorously stirred for one hour at 80 °C. Finally, the precipitates were collected through centrifugation and washed several times with distilled water. These cleaned precipitates were dried in an electric oven at 80 °C. The obtained product was grinded with mortar and pestle and annealed at 300 °C for 2 hours. Ag doped ZnO nanorods were prepared by same procedure except addition of different molar percent of $AgNO_3$. For 2% and 4% Ag doping, 0.002 and 0.004M $AgNO_3$ solutions were added to $ZnCl_2$ solution.

2.5.4 Synthesis of Ni_xZnO_{1-x} nanorods

Ni_xZnO_{1-x} nanorods were prepared by same procedure as adopted for Ag doped ZnO nanorods except addition of different molar percent of nickel chloride. For 2%, 4% and 6% Ni doping, .002, .004 and .006 M solutions of nickel chloride were added to $ZnCl_2$ solution.

2.5.5 Synthesis of Ce_xCuO_{1-x} nanostructures

Ce_xCuO_{1-x} nanostructures were synthesized via chemical co-precipitation route. Appropriate ratios of $CuCl_2.5H_2O$ and $CeNO_3-6H_2O$ were dissolved in distilled water to obtain 0, 2, 4 and 6% Ce doped CuO. Acetic acid was added as a surfactant to control the size and morphology. After 20 minutes of vigorous stirring, an aqueous solution of sodium hydro oxide (1M) was added dropwise to adjust the pH value at approximately at 10. The obtained solutions were again vigorously stirred at 80°C. After one hour of stirring, the solutions were cooled down to room temperature naturally. The precipitates were collected, washed with distilled water repeatedly and dried at 80 °C in an electric oven. The dried samples were annealed in electric furnace at 300 °C for 2 hours to obtain highly crystalline material.

2.6 Determination of Antibacterial Activity

Antibacterial activity of synthesized nanostructures were examined against; Gram-negative *E. coli, Pseudomonas aeruginosa* and Gram positive *S. aureus.* All strains were grown aerobically at 37°C under normal laboratory light conditions.

The in vitro antibacterial activities of the prepared nanostructures were studied by agar disc method. Single colonies of these bacteria were cultured in agar medium by lawn formation. The colloidal suspensions of nanostructures (2 mg/ml) were applied to agar Petri plates by disc method. These agar plates were incubated at 37°C for 24 hours and zone of inhibition was measured in millimetres (mm).

For antibacterial assay, above mentioned microorganisms were grown in a liquid media (nutrient broth media) in presence of colloidal suspension (2 mg/ml) of nanostructures. Cultures grown without prepared nanorods colloidal suspension under the same conditions were considered as control. Growth of these microbial colonies was monitored by measuring optical density (OD) at interval of every 2 hours by UV-visible spectrophotometer at wavelength of 600 nm.

2.7 Cell culture and Treatment with MOs Nanostructures

The human cell line *SH-SY5Y* Cells was purchased from ATTC (Manassas, VA, USA). Cells were maintained in Dulbecco's Modification of Eagle's Medium (DMEM) medium supplemented with 10% fetal bovine serum (FBS) and grown at 37 °C in humidified environment with 5% CO_2 plus 95% air. Cells were seeded in well plates and allowed to attach for 48 hours. The suspensions of the prepared nanostructures were applied to the cells. Cells cultured without presence of the nanostructures were used as control in these experiments. Florescence microscope was used for cells viability assay and Flow cytometry was used for ROS detection.

2.8 Characterization Techniques

In this portion, the characterization techniques employed to investigate the physical properties of the prepared nanostructures are briefly explained.

2.8.1 X-ray diffraction (XRD)

XRD is a powerful and non-destructive characterization tool being widely used for the examination of finger print of crystalline materials, crystal structure and quality, detection of impurity phases and crystallite sizes of various materials. XRD utilize X-rays for the material examination. X-rays are electromagnetic radiations having wavelength in the range of angstroms (Å) which is comparable to the inter-atomic spacing of the materials. Thus when x-rays of suitable wavelength are plunged on the material, it undergoes diffraction according to the Braggs law as shown in the figure 2.8.
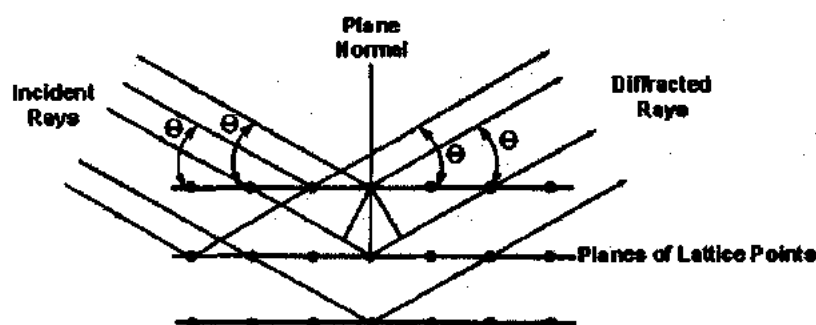
Figure 2.8 Diffraction of X-rays [100]

The diffracted X-rays experience constructive interference if they are in phase to each other and destructive interference if out of phase. The constructively interfered X-rays produce distinct diffraction peaks at specific angles which are recorded by a detector in the XRD setup. Every material has their own diffraction peaks located at specific angles which differentiate it from another material. Hence, by plotting the recorded intensities against diffraction angle gives

32

the finger print of the material and an unknown material can be identified. From these diffraction patterns, information about the crystal structure, crystallite sizes and crystalline quality can be obtained via crystallography. We have recorded the XRD patterns of all prepared MOs nanostructures with step size of 0.2° (2θ) and 2θ range of $20\text{-}70^\circ$ using PANalytical X-ray diffractometer (Model: 3040/60 X'Pert PRO made in Netherland). This X-ray diffractometer utilizes CuK_α X-rays having wavelength of 1.54 Å. XRD patterns have been recorded in powder form without any further processing.

2.8.2 Scanning electron microscopy (SEM)

The morphologies and particle sizes of the MOs nanostructures play vital role in det ermining their various properties. Hence, knowing these parameters of MOs nanostructures is of immense interest for understanding their physical properties as well as applications. The surface morphology and particle size of a nanomaterial can be characterized by SEM. SEM utilize electrons for material characterization. According to the principle of SEM, collimated beam of electrons generated from electron gun are focused on the sample which is placed in high vacuum chamber. The electron beam generates various types of signals from the sample such as; secondary electrons, Auger electrons, backscattered electrons, X-rays and light. These signals are detected by a detector present inside the sample chamber and attached with the computer. The secondary electrons give the images of the surface topography of the sample. The non-conducting samples are coated with carbon, silver or gold in order to avoid the surface charging effects. The average particle sizes have been obtained by marking diameter and length of 30 particles and taking their average.

2.8.3 Fourier transform infrared (FTIR) and Raman vibrational spectroscopy

The structural and vibrational characteristics of nanomaterials can be investigated by employing the FTIR and Raman spectroscopic techniques. They are the two most common and

33

useful spectroscopic techniques based on the atomic vibration of a molecule. Both spectroscopic techniques have different selection rules for transitions. Hence, utilization of both techniques is complimentary.

2.8.3.1 FTIR spectroscopy

FTIR spectroscopy is a powerful non-destructive characterization tool based on the interference of two beams of radiations to have an interferogram. The interferogram is a signal originated as function of difference in the pathlength of the interfering beams. In FTIR, infrared radiations are allowed to pass through the sample. Some portion of the radiation is absorbed by the sample while the remaining portion passes through it, which is called transmittance. The absorption of infrared radiation cause vibrational excitation of polar bonds of the sample. Therefore, the presence of dipole moment in the sample is essential for radiation absorption. The plot of radiation absorbed versus frequency gives FTIR spectra which contain information related to the vibrational or phonon modes present in the sample. The detection of vibrational or phonon modes are governed by certain selection rules. Every material polar bond can only be excited radiation of specific frequency. Hence, FTIR gives us fingerprints of the unknown material. Further, the peak position, width and height can give us information about the crystal structure and crystalline quality of the material. MOs nanostructures have a very high aspect ratio (i.e. surface to volume ratio) when compared to their bulk counterpart. This property makes nanostructures more chemically reactive, because more atoms are accommodated on the surface. Due to higher chemical reactivity, various functional groups can be attached with the surface of the MOs nanostructures intentionally or unintentionally. Therefore, knowing the surface chemistry of samples that have been synthesized is of immense interest. The infrared radiation can excite the molecule of these functional groups. Thus FTIR spectra also contain information about the different functional groups attached to the surface of the sample. In this thesis,

34

NICOLET 6700 FTIR spectrometer made by THERMO SCIENTIFIC, USA has been employed for investigation of the MOs nanostructures vibrational or phonon modes, presence or absence of impurity states and surface chemistry. FTIR spectra of prepared MOs nanostructures have been obtained by mixing 2 mg of nanostructures with 98 mg of KBr to prepare 13 mm pellets. For backgroung corrections 100 mg KBr pellets have prepared. First, an FTIR spectrum of pure KBr pellets has been recorded for background signals correction.

2.8.3.2 Raman spectroscopy

Raman spectroscopy is a more versatile spectroscopic technique than FTIR. Raman spectroscopy is believed to be more sensitive than FTIR. It is based on the Raman scattering phenomena discovered by an Indian scientist C.V. Raman in 1928. According to the working principle of Raman spectroscopy, when a beam of monochromatic light (usually obtained from LASER) is shined on the sample, the light is scattered. This scattering arises from the interaction of monochromatic light with electric dipole of a molecule in the sample. The scattering can be illustrated as the change in the vibrational energies of an electric dipole upon light illumination or in other words excitation of molecules to higher vibrational states. The resultant scattered light may have the same frequency as of the incident light (Raleigh scattering) or lower (Stokes scattering) or higher frequencies (anti-Stokes scattering). The Stokes scattering is normally experiential in Raman spectroscopy which is shown in figure 2.9. The Raman shift which is measure of the difference in the energies of the incident and scattered light, gives the vibrational or phonon frequencies of the sample. A Raman spectrum is obtained by plotting the Raman shift versus intensities of the scattered light.

35
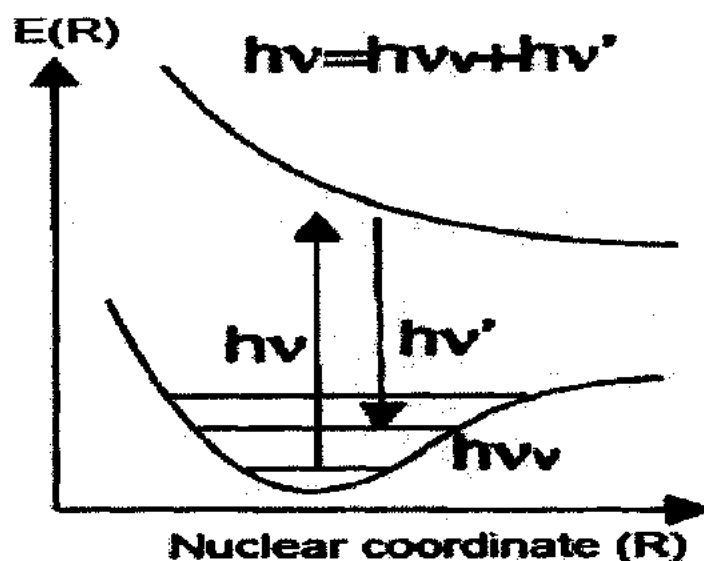
Figure 2.9 Stokes scattering in Raman spectroscopy [101]

Raman spectroscopy is a very valuable technique for examining the microstructure and structural defects of nanomaterials. It has the capability to notice the presence of minor phases in the sample which are not easy to detect with help of XRD. In this thesis, Raman spectroscopy has been used to study the vibrational properties of MOs nanostructures as well as to investigate the crystal defects in these nanostructures.

2.8.4 Ultra violet (UV)-visible absorption spectroscopy

UV-vis absorption spectroscopy is a simplest, non-destructive and most useful spectroscopic technique being widely used for the investigation of optical properties of nanomaterials. It is based on the principle of light absorption due to the electronic transitions in a sample. The electronic transitions in a sample can only be caused by light having wavelength in UV or visible region that is why this technique is named as UV-vis absorption spectroscopy. When light of intensity (I_o) is shined on the sample, some fraction of light is absorbed while the remaining fraction is transmitted by the sample. The transmitted light having intensity (I) is

36

detected by the detector. The I_0 and I are related to absorption of light A by Beer's law stated as follows:

$$A = Log (I_0/I)$$

This law states that when transmitted light fraction is low, the fraction of absorbed light will be high and the other way around. The schematic diagram of the UV-vis spectrometer is shown in figure 2.9. The plot of the transmitted light versus wavelength of the light will give absorption spectrum of the sample. From this spectrum, different information regarding the optical properties of the sample can be obtained such as light absorption and transmission capabilities of the sample, optical band gap energy and electronic behavior of the sample. UV-visible absorption spectra of the prepared MOs nanostructures have been obtained by dispersing 1 mg of nanostructures in 1 ml distilled water. For background correction, first absorption of pure distilled water has been recorded then subtracted from the spectra of MOs nanostructures.
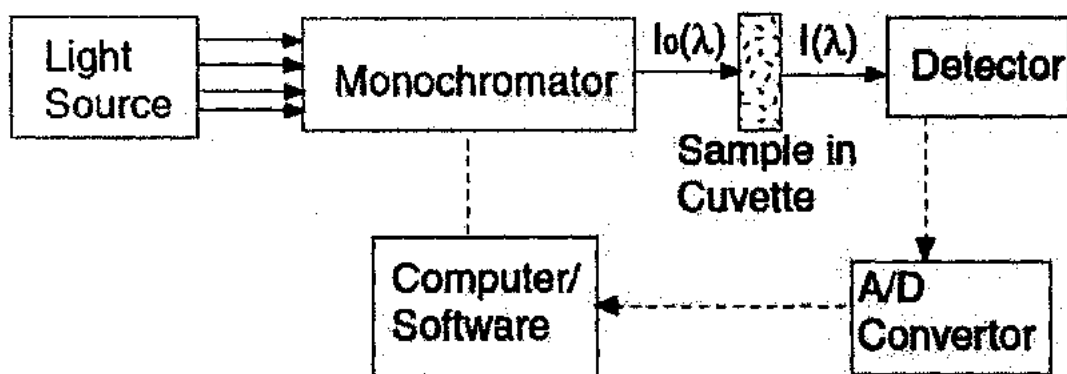
Figure 2.9 The schematic diagram of the UV-vis spectrometer [101]

Chapter No. 3

Synthesis, Characterizations and Antibacterial Activity of MOs Nanostructures

3.1 Introduction

These days, MOs have been used widely in the fabrication of solar cells, sensors, fuel cells, microelectronic circuits, catalysis process and in piezoelectric devices. Nanostructures of MOs can demonstrate unique physical and chemical properties because of their nano-scale size, high aspect ratio (i.e. surface to volume ratio of atoms) and edge effect [10]. MOs nanostructures such as ZnO, CuO, SnO_2 and CeO_2 synthesized by co-precipitation technique have been characterized for the study of several physical properties such as structural, morphological and optical properties. Furthermore, the antibacterial activity of these prepared MOs nanostructures have been investigated by agar disc method.

3.2 Results and Discussion

3.2.1 Structural and morphological study

The crystal structures and phase purity of the prepared MOs samples have been investigated by XRD. Figure 3.1 depicts the typical XRD patterns of ZnO, CuO, SnO_2 and CeO_2 nanostructures. All peaks in XRD patterns can be well indexed to the typical wurtzite, monoclinic, rutile type tetragonal and cubic fluorite structures of ZnO, CuO, SnO_2 and CeO_2, respectively [93, 94 and 102]. Furthermore, no impurity peaks are detected, which confirms the phase purity of all the prepared MOs nanostructures.
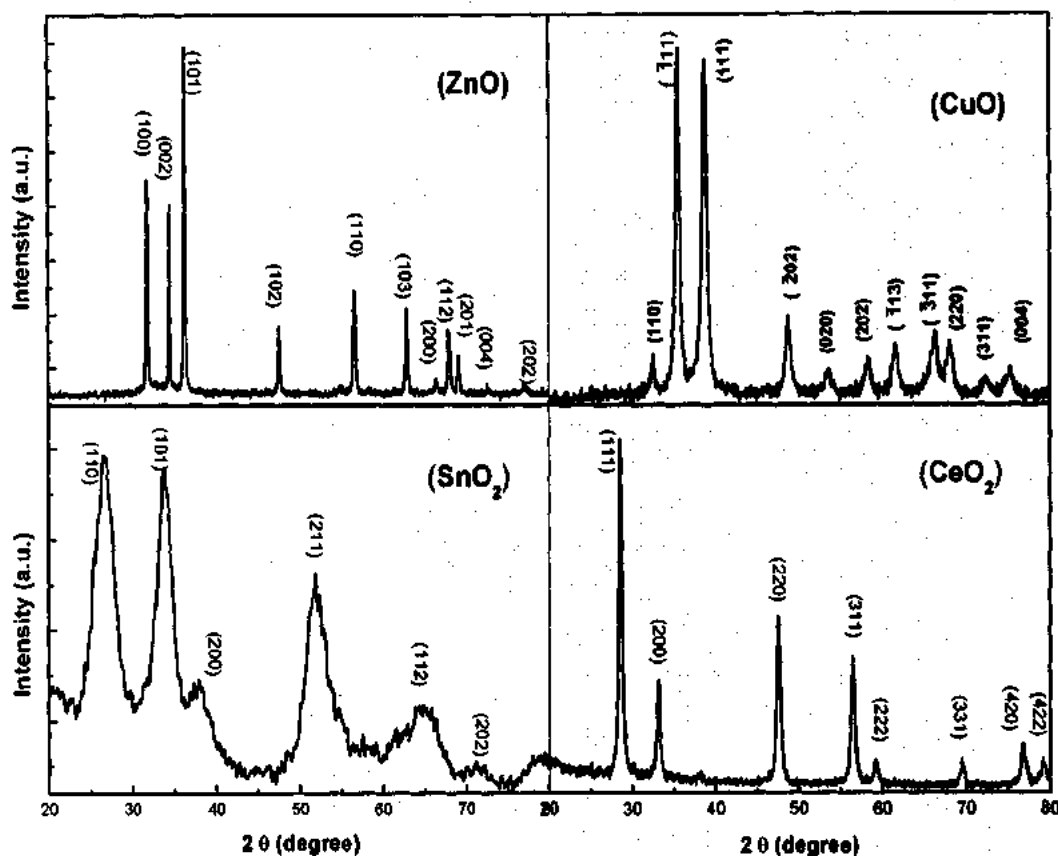
Figure 3.1 XRD patterns of MOs nanostructures.

The crystallite sizes for all prepared samples are calculated using Scherrer formula;

$$D = \frac{0.9\lambda}{\beta cos\theta}$$

where λ is the wavelength of X-ray, β is full width at half maximum of the peak at diffracting angle θ. The calculated crystallite sizes are found to be 18 nm, 12 nm, 8 nm and 17 nm for ZnO, CuO, SnO_2 and CeO_2, respectively. The morphology and chemical composition of the synthesized samples have been investigated by SEM. SEM micrographs of the synthesized MOs samples are shown in figure 3.2.
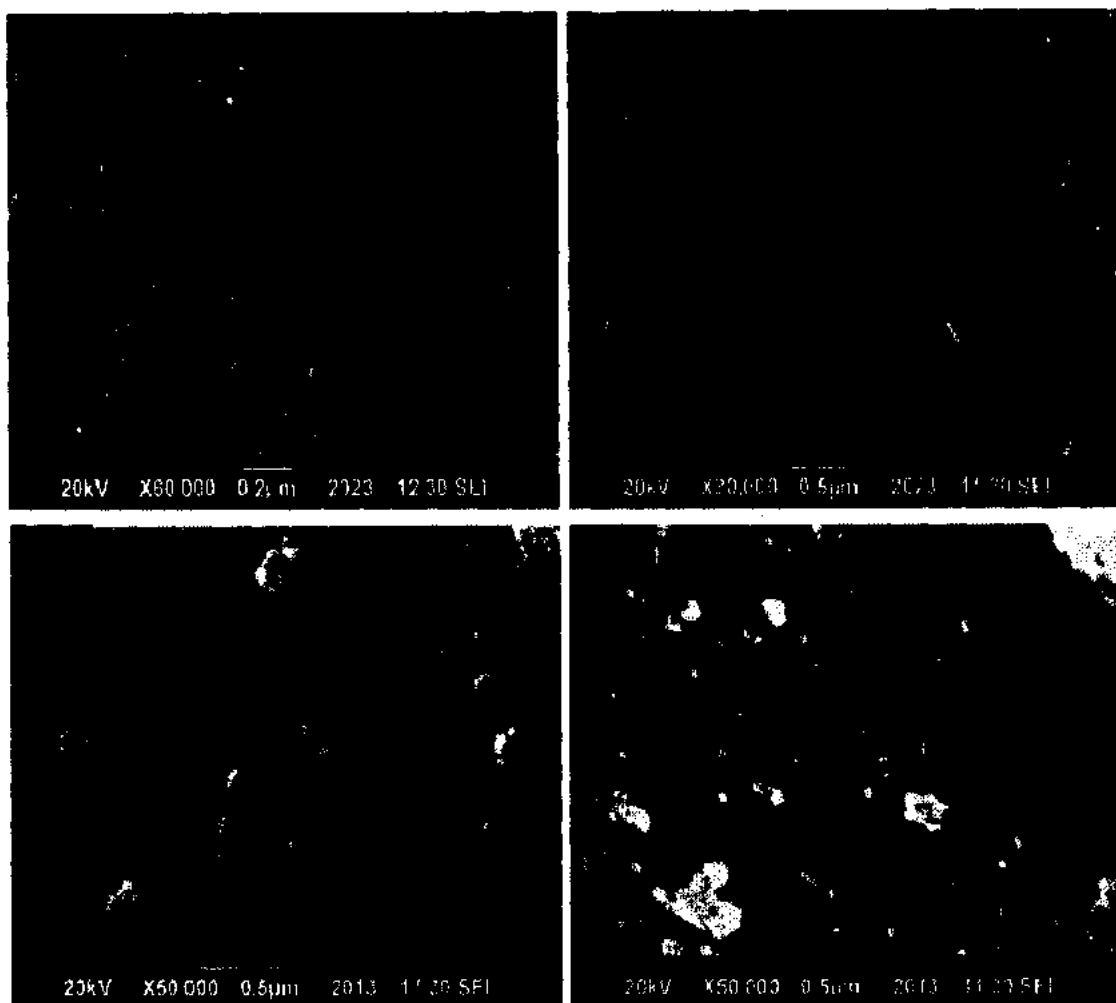
Figure 3.2 SEM images of MOs nanostructures.

Spherical nanoparticles are found in case of ZnO, SnO_2 and CeO_2 samples, while the hierarchal

nanostructures are found in case of CuO sample. The average particle sizes obtained from SEM

images are 25 nm, 28 nm and 30 nm for ZnO, SnO_2, and CeO_2 nanostructures, respectively.

3.2.2 FTIR study

Nanostructures have very high aspect ratio as compared to their bulk counterpart. This

property makes them more chemically reactive because more atoms are accommodated on the

surface. Therefore, the study of surface chemistry of prepared MOs nanostructures is of utmost

importance. To study the presence or absence of various vibration modes on the surfaces of

40

samples, FTIR spectra have been recorded in the range of 400-1500 cm^{-1}. FTIR spectra of ZnO, CuO, SnO$_2$ and CeO$_2$ nanostructures are shown in Figure 3.3. The FTIR spectra of all MOs nanostructures demonstrate series of vibrational modes from 400 to 1500 cm^{-1}. The presence of vibrational modes in the region of 400–600 cm^{-1}, for all samples, shows the existence of M-O bonding (M = Zn, Cu, Sn, and Ce) [93]. Thus, FTIR spectroscopy results corroborate very well with the XRD results.
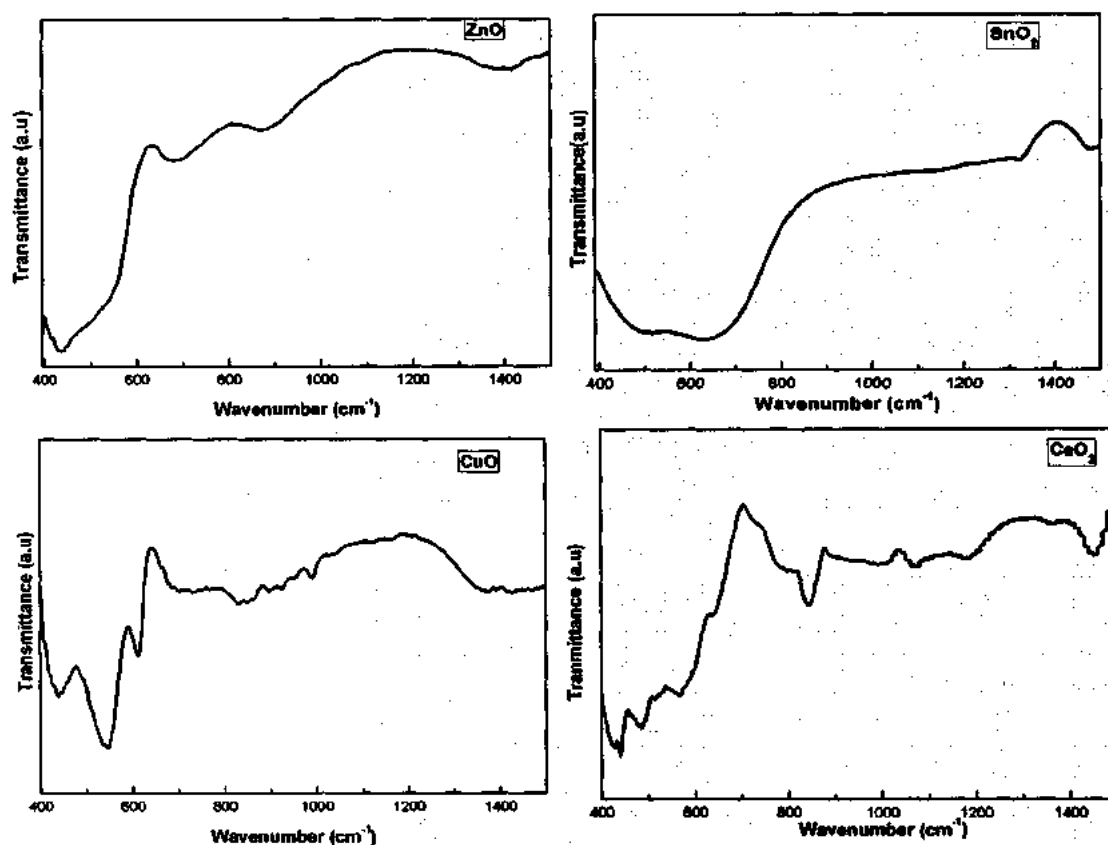
Figure 3.3 FTIR spectra of MOs nanostructures

3.2.3 Optical study

After determining the structure, morphology and purity, the optical characteristics of MOs nanostructures have been studied at room temperature. Optical spectra of the MOs nanostructures dispersed in distilled water are depicted in figure 3.4. ZnO nanoparticles exhibit

typical exciton band gap absorption at 376 nm which is blue shifted as compared to its bulk counterpart [103]. CuO nanostructures show maximum absorption peak at 380 nm, which is assigned to the surface plasmon absorption [104]. SnO_2 and CeO_2 exhibit band edge absorption at 326 nm and 322 nm, respectively. The obtained results are matched well with the reported ones [103–106].
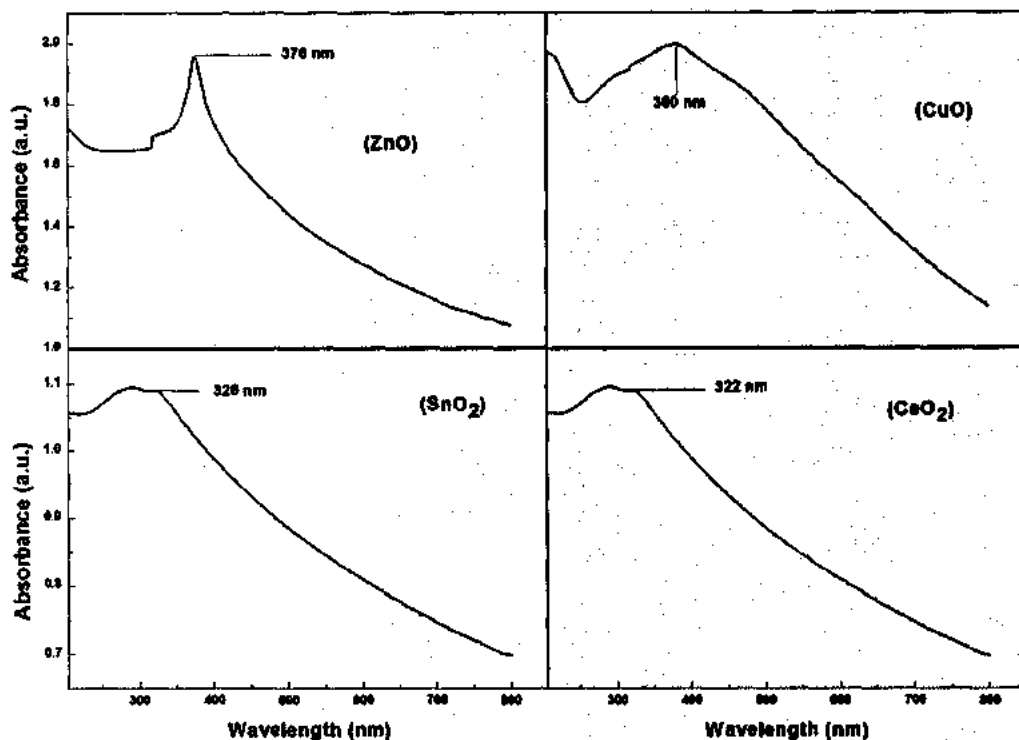
Figure 3.4 UV–visible absorption spectra of MOs nanostructures

3.2.4 Antibacterial activity

E. coli is one of the most resistant bacterium due to its thick cell wall. The cell wall of it is comprised of a thick PG layer and outer membrane. It shows resistance to wide variety of drugs because of this complex cell wall [101]. Additionally, the E. coli bacterium protects itself by creating bio-films. Bio-films cover the bacterial cells community and protect it from antibiotics [107]. Hence MOs nanostructures can be effectively used to break these bio-films due

to their small sizes and extraordinary physiochemical characteristics. At nanoscale, MOs possess high surface area which leads to higher chemical and biological reactivity of MOs nanostructures. Due to these properties, the MOs nanostructures react proficiently with the cell membranes and lead to their death [108]. Previously, number of possible mechanisms of interaction between MOs nanostructures and bacteria are proposed likewise photo-activation of MOs and generation of electron hole pairs which produce reactive oxygen species (ROS) by interacting with water and oxygen molecules, Columbic interaction between nanostructures and bacterial cells and accumulation of nanostructures inside the cells [109]. By the interaction of MOs nanostructures with bacterial cells via any of the above mechanisms, it leads to cell death and form zone of inhibition (ZOI) around nanostructures. Disc diffusion method has been adopted to investigate the in vitro antibacterial activity of MOs nanostructures against multi-drug resistant E. coli bacterium. Antibacterial activity results reveal that the ZnO nanoparticles exhibit highest level of bactericidal potency against E. coli. ZnO, SnO_2 and CeO_2 nanoparticles produce 10 mm, 6 mm, and 3 mm of ZOI, while CuO nanostructures could not produce any ZOI (figure 3.5). The ZOIs formed around the SnO_2 and CeO_2 nanoparticles (white spot) are not much clear, which demonstrate that some E. coli are still proliferated within the ZOI. This shows that the bactericidal effectiveness of SnO_2 and CeO_2 nanoparticles is poor. While the ZOI around ZnO nanoparticles (white spot) is very much clear, which reveals that ZnO nanoparticles act as an excellent antibacterial agent as compared to other MOs nanostructures tested. Particle sizes and morphology play an important
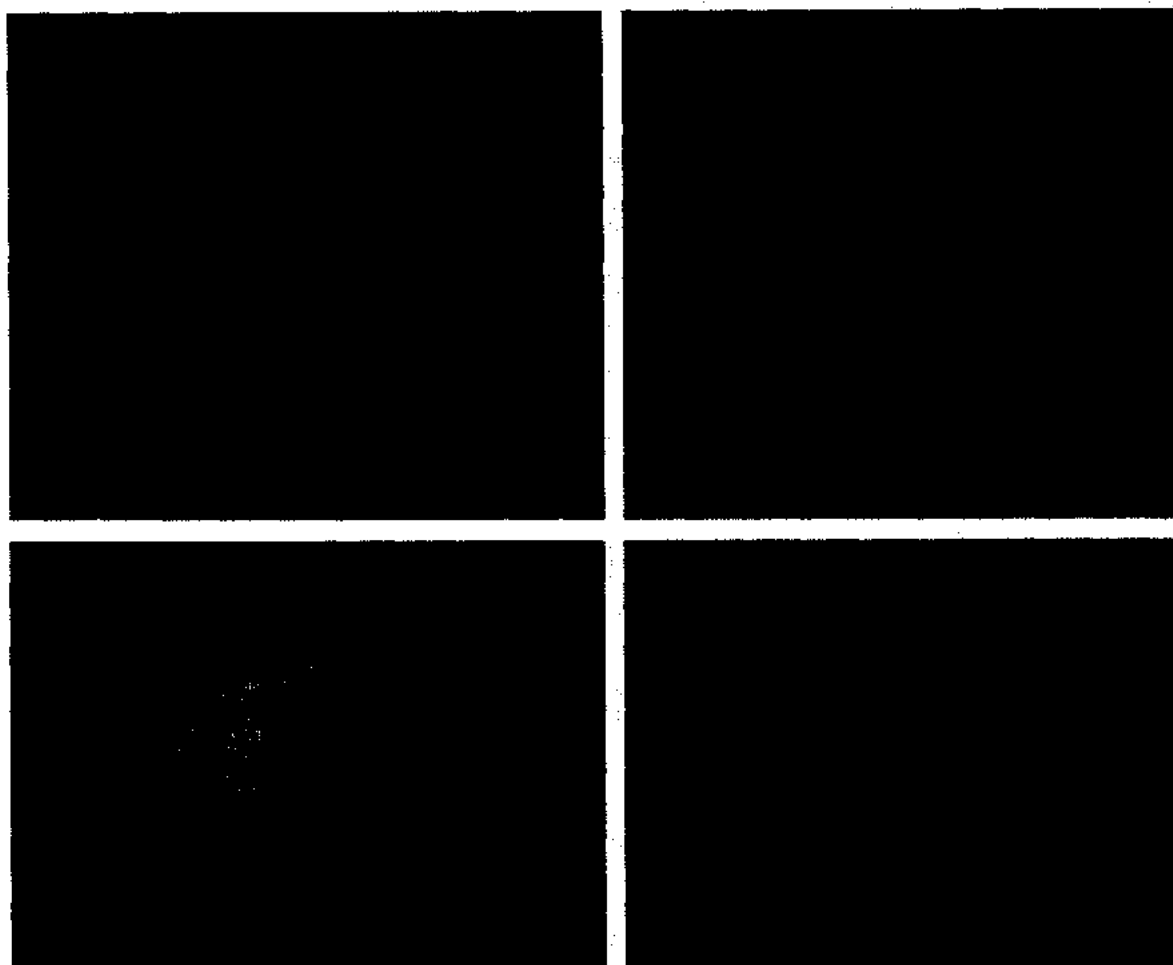
Figure 3.5 ZOI produced by different MOs nanostructures (a) ZnO, (b) CuO, (c) SnO$_2$ and (d) CeO$_2$

role in the antibacterial activity of MOs nanostructures [93, 110]. Tam et al. have reported the highest antibacterial activity for small size spherical nanoparticles as compared to nanopowders and nanorods [110]. The SEM results demonstrate that ZnO has the smallest particle size (25 nm) among all the MOs samples. It can also be seen from the SEM results that CuO has a hierarchal morphology. Thus, the higher antibacterial activity of ZnO nanoparticles may be attributed to its smaller particle sizes. The resistance of E. coli towards CuO may be attributed to its hierarchal morphology. The solubility of MOs increases with the decrease in particle sizes.

The high solubility of MOs nanostructures can increase the concentration of soluble metal ions as a result there is enhancement in the antibacterial activity of MOs nanostructures [51]. Furthermore, the solubility of MOs nanostructures also depends on the type of MOs. Recently, it is reported that ZnO nanoparticles have higher solubility than CuO, Sb_2O_3 and NiO nanoparticles [111]. Antibacterial activity also depends on the physicochemical properties of MOs nanostructures [107]. Hence, the difference in antibacterial activity of different MOs nanostructures may be attributed to their particle sizes, different morphology, solubility and physicochemical properties.

Chapter No. 4

Synthesis, Characterizations and Antibacterial Activity of Sn Doped ZnO Nanostructures

4.1 Introduction

At nanoscale, ZnO demonstrates unique physical and chemical properties because of its high aspect ratio of atoms (i.e. surface to volume ratio). ZnO nanostructures have vast applications such as dye sensitized solar cells, field effect transistors, targeted drug delivery, anticancer agents, and antibacterial activity [111–115] Recently, it has been reported that the doping of ZnO nanostructures with other elements can enhance its various properties [116]. Commonly, different elements as a dopant in ZnO can be categorized into two groups: one group can fill in for zinc (Zn) and the second group for oxygen (O). These different dopants can tune various properties of ZnO nanostructures. Sn as a cation dopant can substitute for Zn and tailor various properties of ZnO nanostructures [117].

Mortality and morbidity linked with pathogenic bacteria remain high regardless of antimicrobial therapy, partially because these species develop resistance capability to antibiotics. Therefore, new strategies are highly desired to identify and to develop a new generation of agents against these species. ZnO nanostructures are of particular interest due to their low cost, nontoxic nature, their abundance in nature, and established use in health care products [118, 119]. Recently, it is reported that Sn doping has significantly enhanced the antibacterial activity of titanium dioxide (TiO_2) nanoparticles [120]. But the use of TiO_2 is limited due to its allergic reactions to sensitive skin. However, ZnO is known to have significant activity against various microorganisms and does not cause any allergic reactions on the skin by dispersing the light falling on it [121]. In this chapter, $Sn_xZn_{1-x}O$ nanostructures have been fabricated by a simple co-

precipitation technique and the effects of Sn doping on the antibacterial activity and physiochemical characteristics of ZnO nanostructures is studied in detail.

4.2 Results and Discussions

4.2.1 Structural and morphological studies

To study the influence of Sn doping on the structural characteristics of ZnO nanostructures, XRD analysis of $Sn_xZn_{1-x}O$ nanostructures has been carried out with step size of $0.2°$ (2θ) and 2θ range of $20°–70°$ with CuKα radiation having wavelength $1.54Å$. Figure 4.1 shows the XRD patterns for $Sn_xZn_{1-x}O$ nanostructures. The broadness of the peaks in XRD patterns shows the nanocrystalline nature of all prepared samples. All peaks are indexed to (100), (002), (101), (102), (110), (103), (200), (112), and (201) planes which corresponds to the typical hexagonal wurtzite structure of ZnO. This is in conformity with reported literature and the standard pattern of ZnO [122]. The absence of extra peaks related to Sn or other impurities in the XRD patterns with Sn doping substantiates the phase purity of all synthesized samples. There is a shift toward higher angle and a decrease in the peak width with Sn doping, as shown in figure 4.2, which confirms the successful incorporation of Sn into the ZnO lattice and the reduction of strain [123]. The particle sizes have been calculated from the broadening of the main peak (101) using Scherrer's formula $Sn_xZn_{1-x}O$ samples. The average sizes of particles are 17 nm, 24 nm, 32 nm, and 36 nm for undoped, 2%, 4%, and 6% Sn doped ZnO, respectively. The increase in particle size of ZnO grown under the same synthesis conditions as a function of Sn doping may be attributed to the fact that ionic radii of Sn^{4+} may be larger than Zn^{2+} ($0.74Å$), which means that the coordination number of Sn^{4+} in the crystal would be greater than 4 ($0.69Å$ for 4-coordinate, $0.83Å$ for 6-coordinate, and 0.95 for 8-coordinate) [124]. The increase in particle size

with doping in the ZnO host matrix may be linked with enhancement in the crystallinity of the synthesized $Sn_xZn_{1-x}O$ nanostructures.
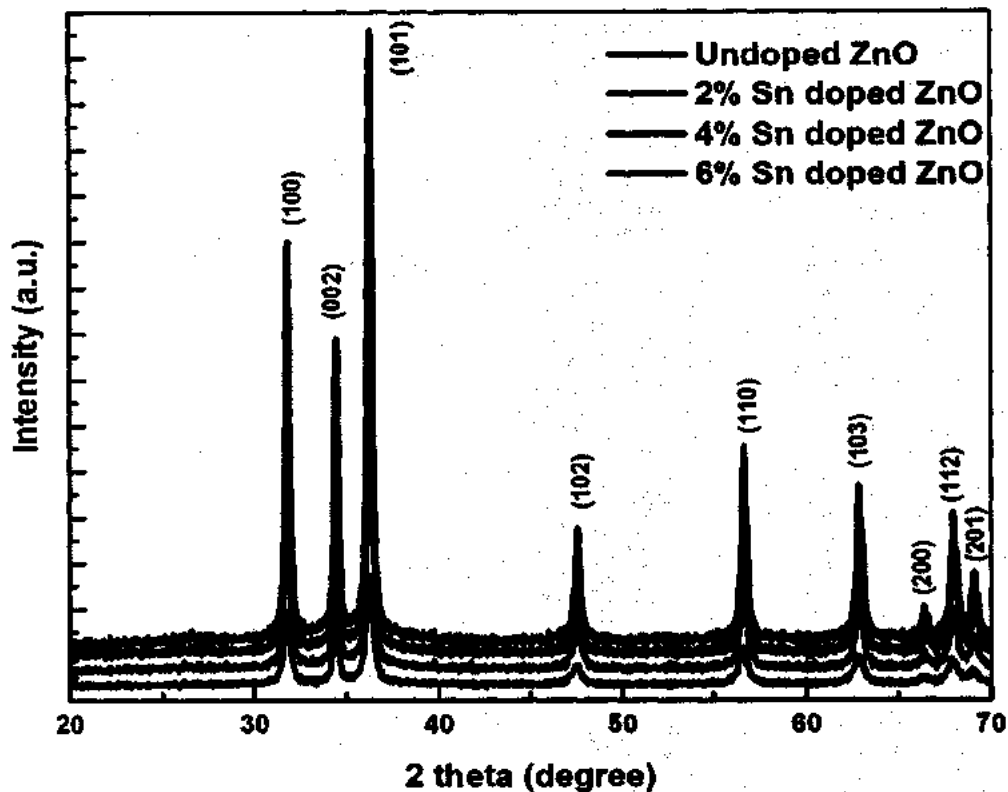
Figure 4.1 XRD patterns $Sn_xZn_{1-x}O$

The morphological examination of $Sn_xZn_{1-x}O$ samples was done by SEM. Figure 4.3 shows SEM micrographs $Sn_xZn_{1-x}O$ samples. It can be observed from the figure that the morphology of ZnO samples is spherical and changes from spherical to rods with Sn doping. The morphological variation may be due to the remarkable influence of Sn ion doping on ZnO nanostructures and dipolar interaction along the c-axis with the Sn^{4+} substitution to Zn^{2+}. The development of nanoparticle's shape strongly depends on the free surface energies associated with various crystallographic planes which differ significantly from each other. In wurtzite structure of ZnO, (0001) surface is the most energetic one and therefore ZnO nanostructures grow along c-axis if

48

suitable conditions are provided [125]. The growth along c-axis guides to formation of one-dimensional ZnO nanostructures. Sn has been reported previously to act as catalyst for directing the ZnO nanostructures growth along c-axis [126]. Hence, sufficient Sn concentration may guide the ZnO growth along c-axis and leads to nanorods formation from the oriented attachment of nanoparticles. A clear increase in particle sizes of $Sn_xZn_{1-x}O$ nanostructures as a function of Sn doping level.
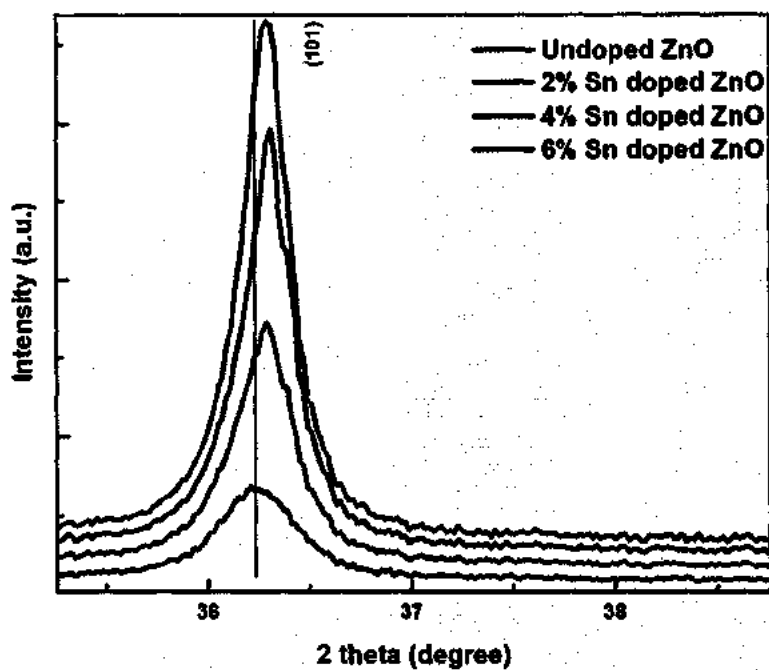
Figure 4.2 Extended XRD patterns of undoped and Sn doped ZnO
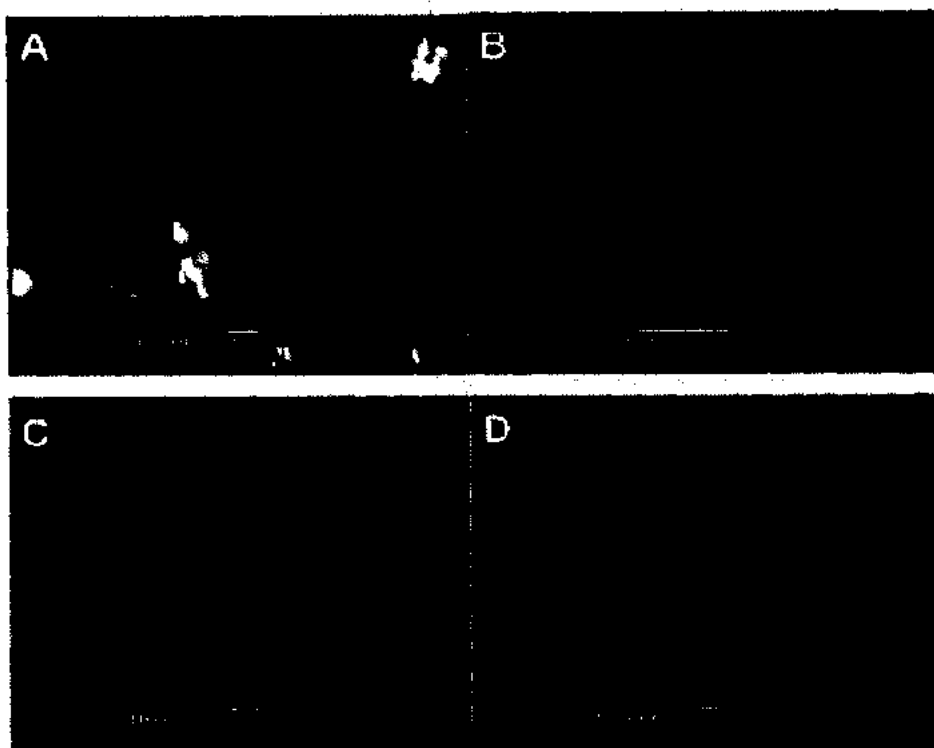
Figure 4.3 SEM micrographs of (A) undoped, (B) 2% Sn (Sn), (C) 4% Sn, and (D) 6% Sn doped ZnO.

The morphologies of $Sn_xZn_{1-x}O$ nanostructures were further examined by transmission electron microscope (TEM). TEM micrographs of undoped ZnO nanoparticles show nearly spherical particles with an average size of 47 nm as shown in figure 4.4 (A). Figure 4.4 (B) represents a TEM micrograph of 4% Sn doped ZnO nanostructures with nanoparticles and nanorods mixed morphologies. It is demonstrated by the TEM results that both particle size and morphology are greatly influenced by Sn doping into ZnO matrix.
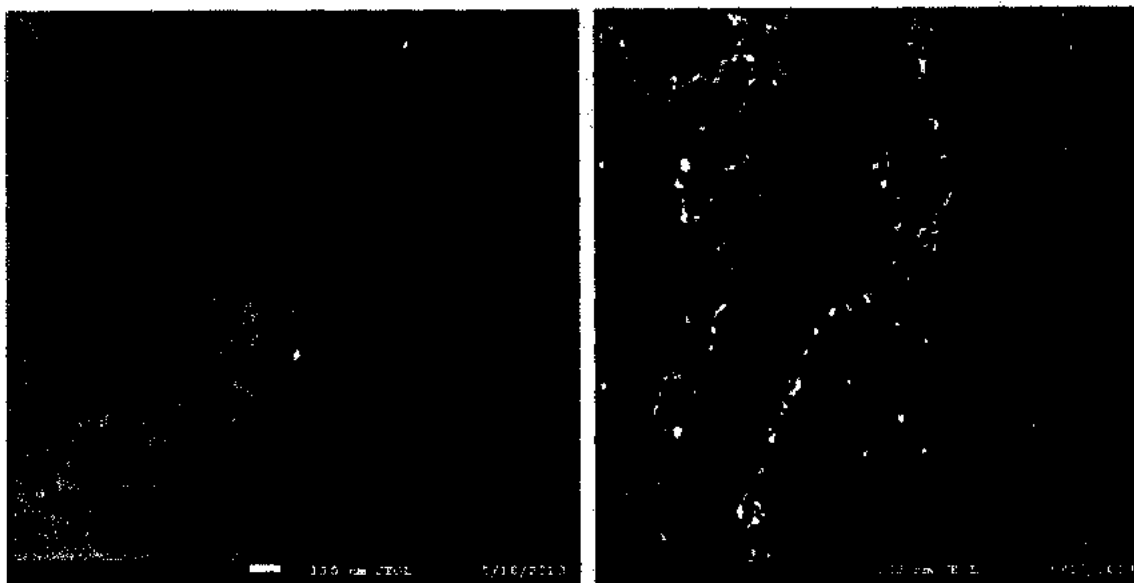
Figure 4.4 TEM micrographs of (A) 0%, (B) 4% Sn doped ZnO nanostructures

4.2.2 FTIR and Raman studies

Nanostructures have a very high aspect ratio (ie, surface to volume ratio) when compared to their bulk counterpart. This property makes nanostructures more chemically reactive, because more atoms are accommodated on the surface. Therefore, knowing the surface chemistry of samples that have been synthesized is of immense interest. To study the presence or absence of various vibration modes and to investigate the influence of Sn doping on ZnO nanostructures, FTIR spectroscopy of $Sn_xZn_{1-x}O$ nanostructures was performed. Figure 4.5 shows the FTIR transmission mode spectra of $Sn_xZn_{1-x}O$ nanostructures.
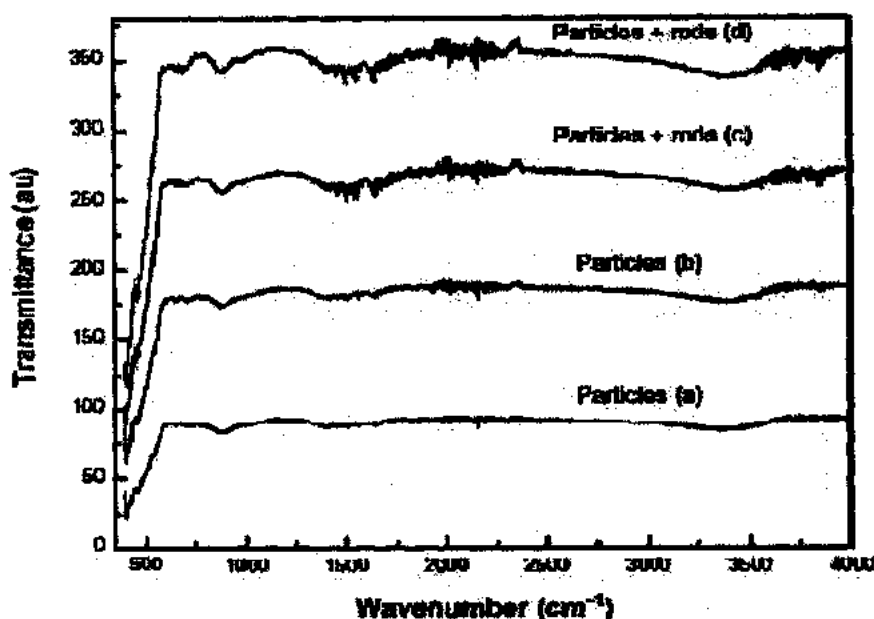
Figure 4.5 FTIR spectra of (a) undoped, (b) 2% Sn, (c) 4% Sn and (d) 6% Sn doped ZnO nanostructures.

The spectrum of each sample shows a series of absorption peaks from 400 to 4000 cm^{-1}. The broad peak at approximately 3360 cm^{-1} in all samples can be attributed to the presence of hydroxyl groups on the surface of samples. The peaks around 1500–1600 cm^{-1} are due to the presence of C=O stretching mode on the surfaces of the samples. In figure 4.5, the characteristic peak of ZnO occurs at approximately 412 cm^{-1}, which confirms the formation of ZnO. In infrared region, when morphology of particles changes from spherical particles to needle like structures, spectra often show two absorption maxima [127]. In our case, when the particle morphology changes from spherical nanoparticles to nanorods, two absorption peaks are observed at approximately 412 cm^{-1} and 695 cm^{-1} for ZnO.

The micro-structural and vibrational properties of the synthesized nanostructures have been studied using Raman spectroscopy. Figure 4.6 depicts the Raman spectra of $Sn_xZn_{1-x}O$ nanostructures. The Raman peak at 434 cm^{-1} represents the characteristic hexagonal wurtzite

52

structure of ZnO. The intensity of this peak is found to increase with Sn doping which is linked with enhancement in the crystallinity of the prepared nanostructures. Furthermore, no additional peaks are detected upon Sn doping which confirms the successful doping of Sn into ZnO matrix. FTIR and Raman spectroscopy results corroborate well with XRD results.
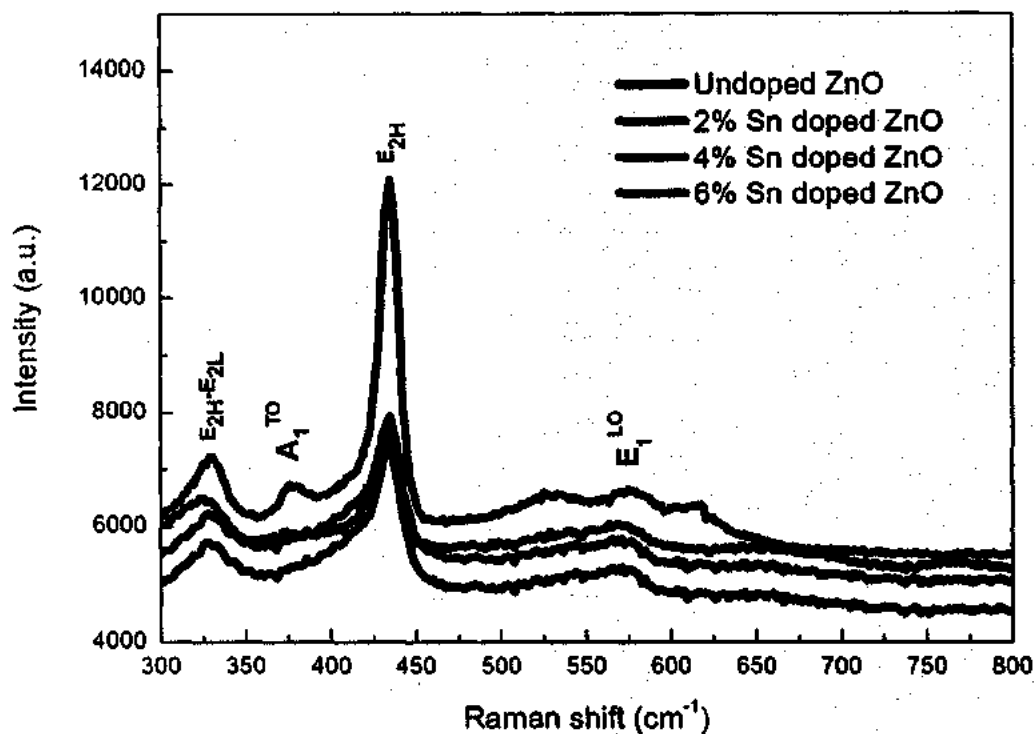
Figure 4.6 Raman spectra of $Sn_xZn_{1-x}O$ nanostructures

4.2.3 Optical study

UV-visible absorption spectroscopy is an important tool to investigate the optical characteristics of nanostructures. To examine the influence of Sn doping on the optical properties of ZnO nanostructures, UV-visible absorption spectroscopy of $Sn_xZn_{1-x}O$ nanostructures was performed and the results are shown in figure 4.7. A typical excitation absorption band at 378 nm is observed for pristine ZnO nanostructure which has a blue shift when compared to that of bulk

ZnO [101]. It can be observed from Figure 5 that the excitation absorption band has a further blue shift with increases in Sn concentration as a dopant into ZnO. As it can be depicted from the XRD and SEM results that particle size increases with the increase in Sn concentration, this blue shift may be attributed to quantum size effects.
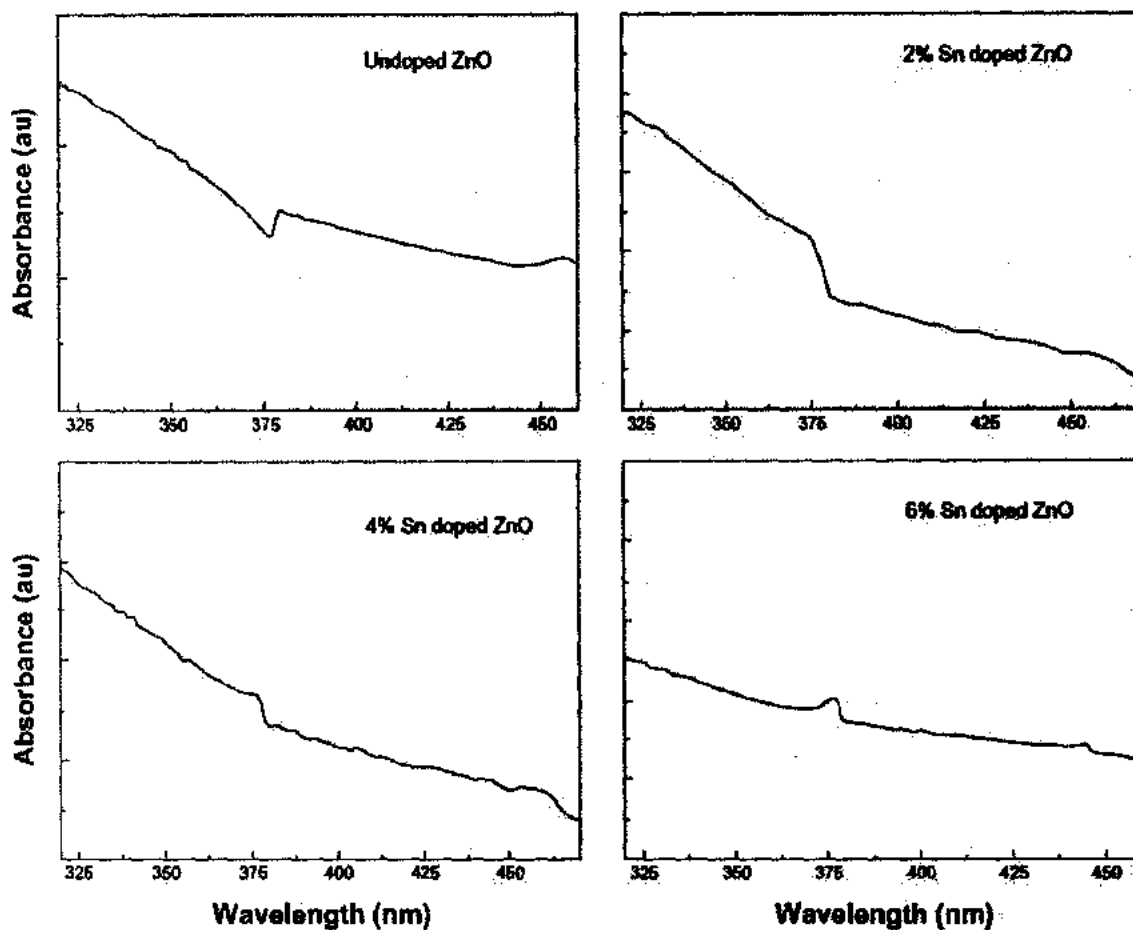
Figure 4.7 UV-vis absorption spectra of the prepared nanostructures

4.2.4 Antibacterial activity

The in vitro antibacterial activity of $Sn_xZn_{1-x}O$ nanostructures toward different bacterial pathogens were investigated by the disc diffusion agar method. All samples show antibacterial activity toward all three pathogens, as shown in figure 4.8. Interestingly, the zone of inhibition

54

produced by undoped ZnO is higher than that of 2% Sn doped ZnO, but less than that of 4% Sn doped ZnO, and the inhibition zone caused by 6% Sn doped ZnO is less than that of 4% Sn doped ZnO against all the three types of pathogens, as shown in figure 4.9. It is demonstrated in the reported literature that particle size and morphology greatly influence the activity of ZnO against various microorganisms [128, 129]. In this study, both particle size and shape have been observed to have significant role in the bactericidal potency of $Sn_xZn_{1-x}O$ nanostructures against all the three pathogens. The antibacterial activity of ZnO nanostructures may be attributed to several mechanisms such as electrostatic interactions of cell walls and membranes, generation of ROS, and medium [129]. In this study, the antibacterial activity of undoped ZnO is higher when compared to 2% Sn doped ZnO, because particle size is lesser in the first case. But the inhibitory activity of 4% Sn doped ZnO is higher than that of undoped and 2% Sn doped ZnO, though particle size of 4% Sn doped ZnO is larger than the undoped and 2% Sn doped ZnO. From SEM results, it has been observed that the morphology of the 4% Sn doped ZnO is rod shaped, while that of the undoped and the 2% Sn doped ZnO was spherical. The inhibitory activity of 6% Sn doped ZnO is less than that of the 4% Sn doped ZnO. This may be due to the reason that the particle size is greater in case of 6% Sn doped ZnO. It may be concluded that the particle size, Sn content, and morphology play vital roles in the activity of $Sn_xZn_{1-x}O$ nanostructures against all the pathogens tested.

A

B

C
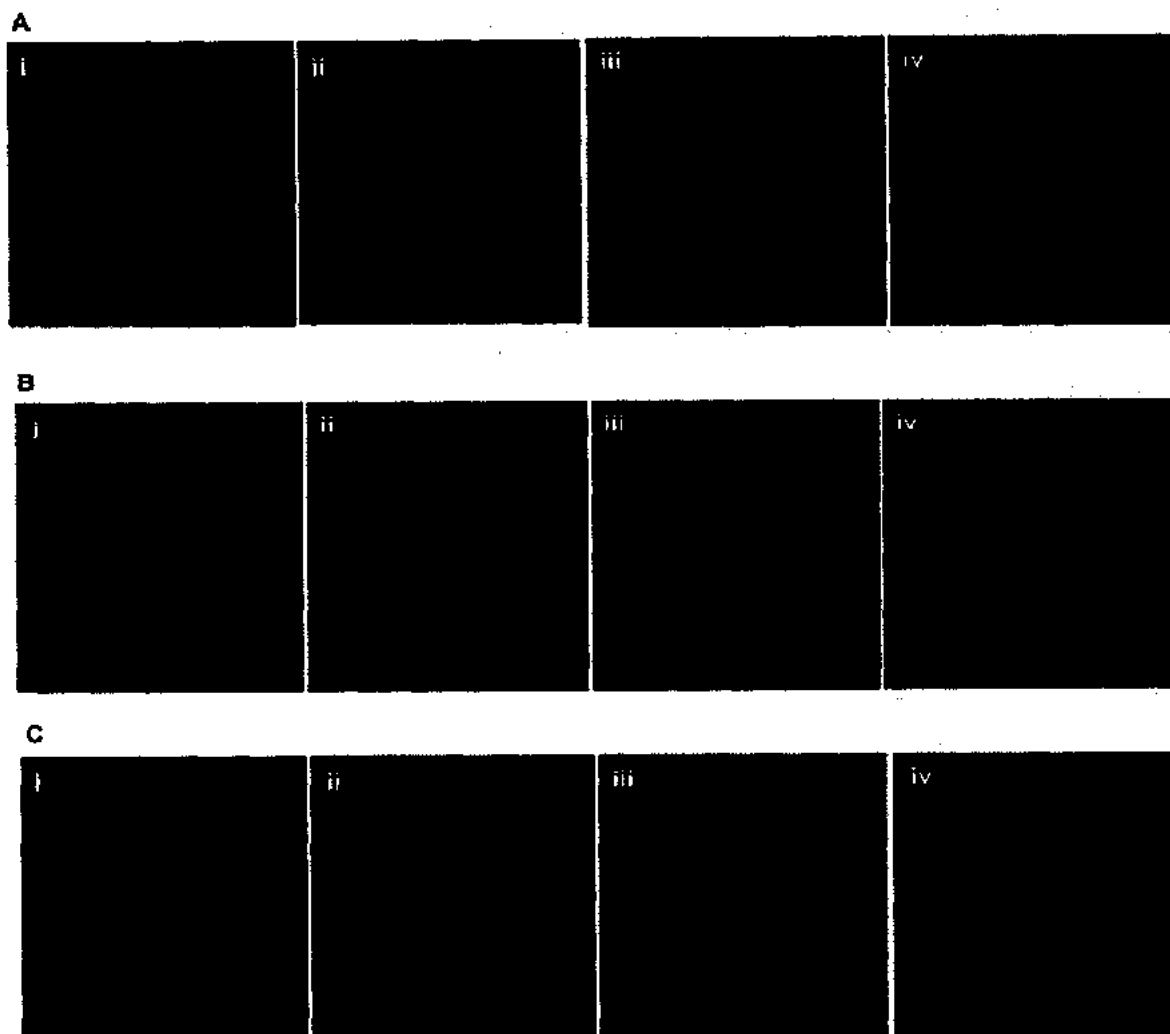
Figure 4.8 ZOI produced by (i) 0%, (ii) 2%, (iii) 4%, and (iv) 6% Sn doped ZnO against (A) E. coli, (B) S. aureus and (C) P. aeruginosa.

The influence of Sn doping on the antibacterial activity of ZnO nanostructures against *E. coli*, *S. aureus*, and *P. aeruginosa* microbial colony growth rate was also investigated. Figure 4.9 (A-C) shows the effect of $Sn_xZn_{1-x}O$ nanostructures on the growth rate of *E. coli*, *S. aureus*, and *P. aeruginosa*, respectively. It is observed that all the synthesized nanostructures effectively inhibited the growth rate of *S. aureus* but is less effective against the other two bacterial strains tested. The antibacterial activity is probably derived from the interaction of negatively charged cell membranes and positively charged nanostructures, interaction of metal ions with bacteria,

56

and the orientation of nanostructures [128]. Sn doping has influenced the activity of ZnO nanostructures against all the bacterial strains tested. The efficacy of ZnO nanostructures against growth inhibition of these bacterial strains varies slightly with increases in Sn concentration.
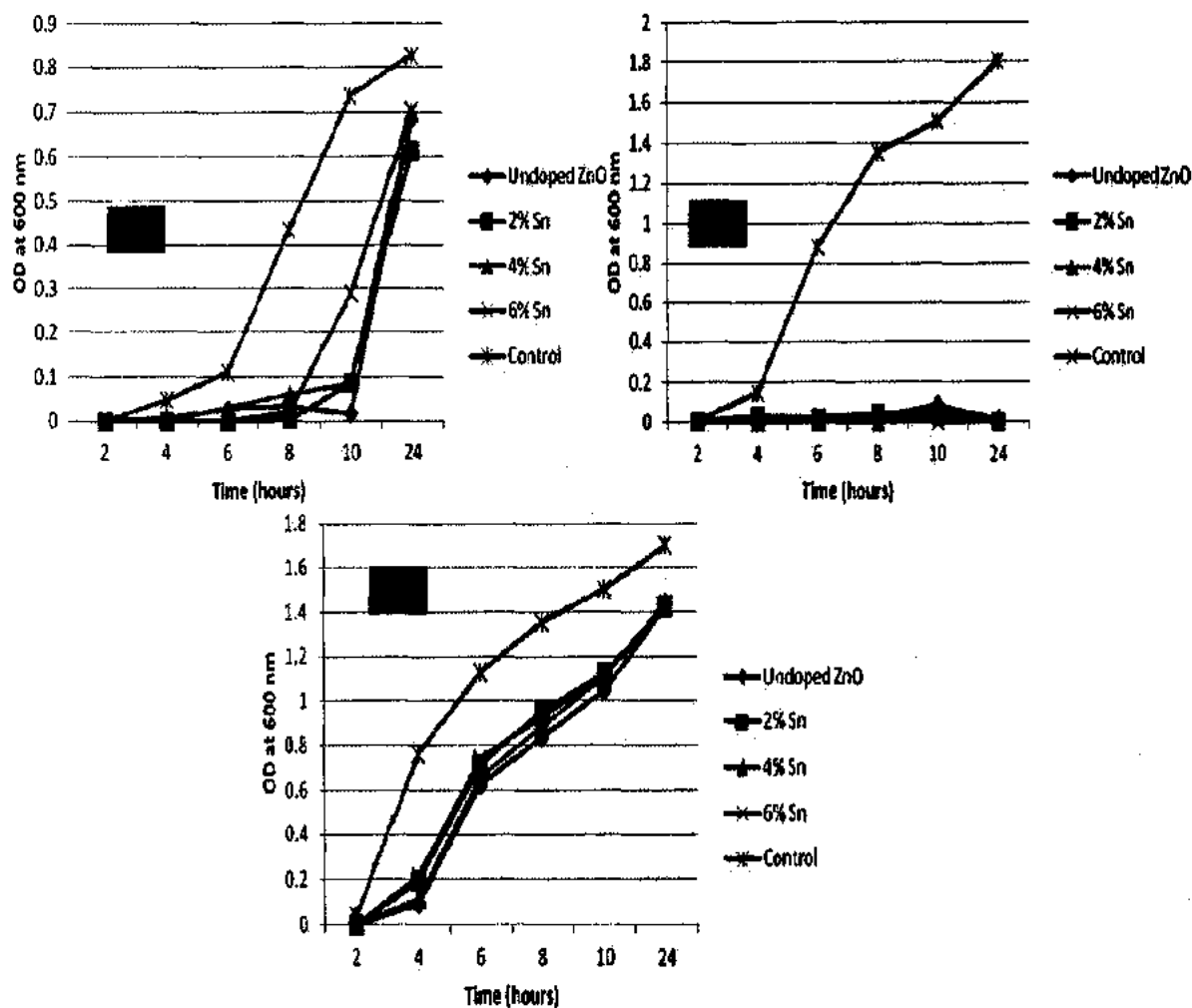
Figure 4.9 Effect of $Sn_xZn_{1-x}O$ nanostructures on the growth rate of A) E. coli B) S. aureus C) P. aeruginosa strain.

Sn doping has significantly enhanced the activity of ZnO against S. aureus when compared to the other two bacterial strains tested. The zone of inhibition produced by 4% Sn doped ZnO is 22

mm, which is almost 37% more than that produced by undoped ZnO nanostructures (14 mm), as shown in figure 4.10. S. aureus is a bacterium responsible for various skin diseases which are hard to treat with traditional antibiotics. S. aureus can also easily contaminate hospital implants and thereby spread and cause various serious infections [129-131]. ZnO is a well known material due to its established use in creams, lotions, antibacterial coatings, and UV protectors. Therefore, using 4% Sn doped ZnO nanostructures instead of ZnO in UV protectors, creams, and lotions will lead to effective control of bacterial infections in addition to their UV blocking properties [118, 129]. Also, the spreading of infectious diseases due to bacterial contamination may be controlled by coating hospital implants with $Sn_xZn_{1-x}O$ nanostructures.
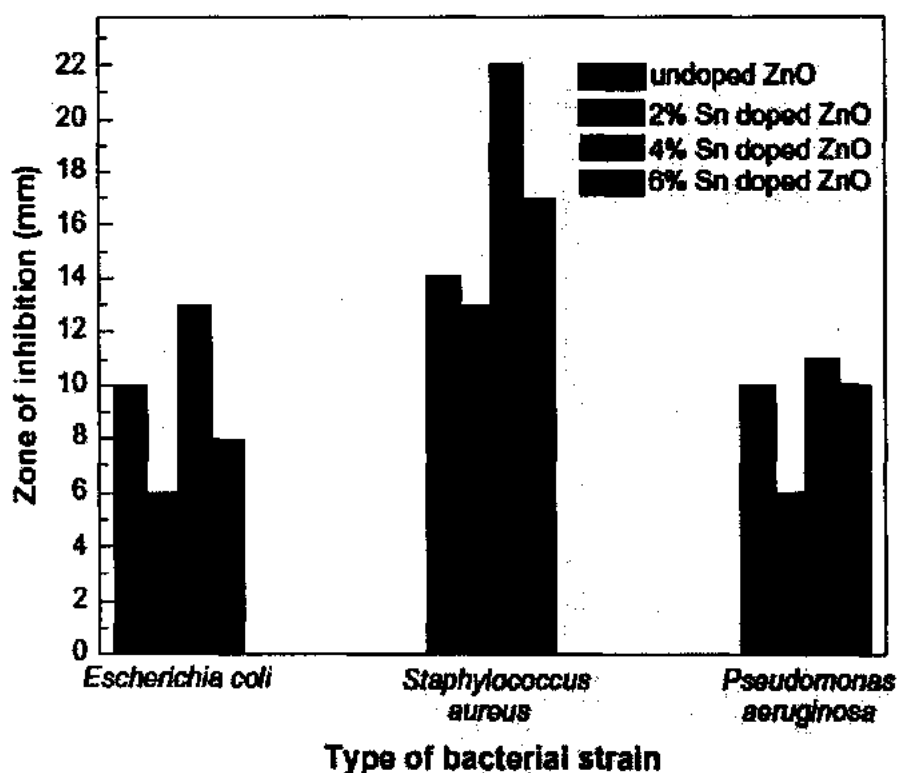
Figure 4.10 Bar graph showing ZOI introduced by $Sn_xZn_{1-x}O$ nanostructures

4.2.5 Cytotoxicity

To evaluate the cytotoxicity of $Sn_xZn_{1-x}O$ nanostructures, SH-SY5Y cells grown in DMEM with 10% FBS were exposed to $Sn_xZn_{1-x}O$ nanostructures for 24 hours and its effect on

SH-SY5Y cells was tested. In order to investigate whether $Sn_xZn_{1-x}O$ nanostructures support cell survival or not, we performed optical microscopy and quantified the total cell number with and without $Sn_xZn_{1-x}O$ nanostructures. It is shown in figure 4.11 that there is no significant effect of $Sn_xZn_{1-x}O$ nanostructures on the SH-SY5Y cells viability. All synthesized samples may be considered as biosafe because the percentage of damage is very low.
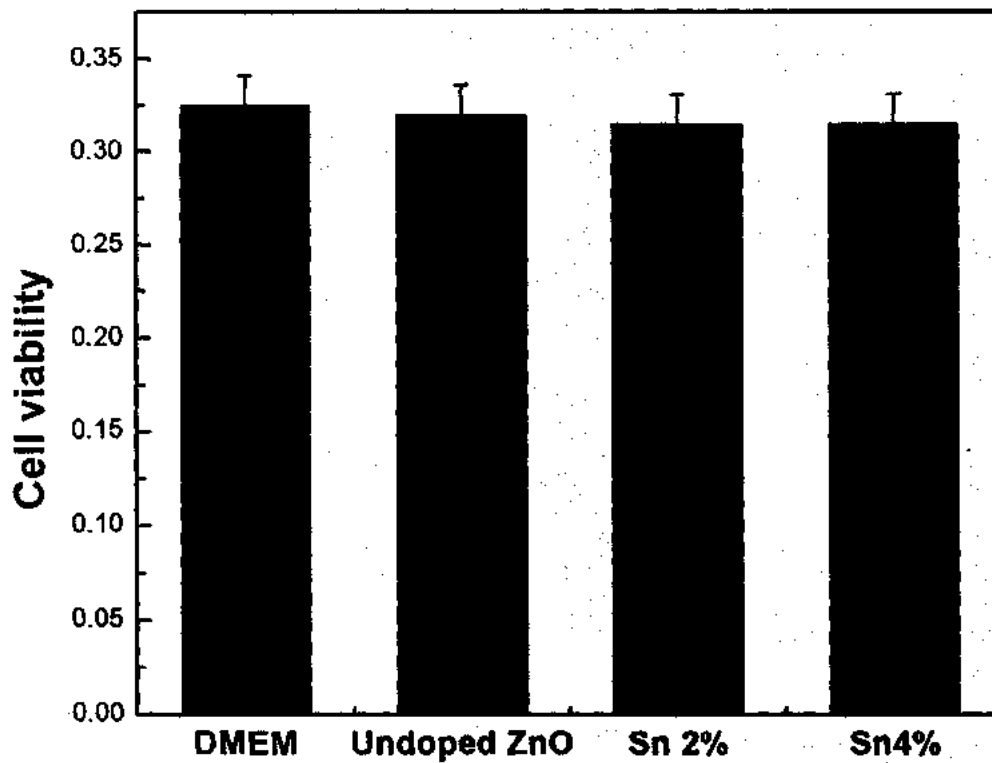
Figure 4.11 Effect of $Sn_xZn_{1-x}O$ nanostructures on SH-SY5Y cells viability

It is also evident from figure 4.12, which was obtained by phase contrast microscopy, that cells are healthy and have normal morphologies in the samples treated with $Sn_xZn_{1-x}O$.
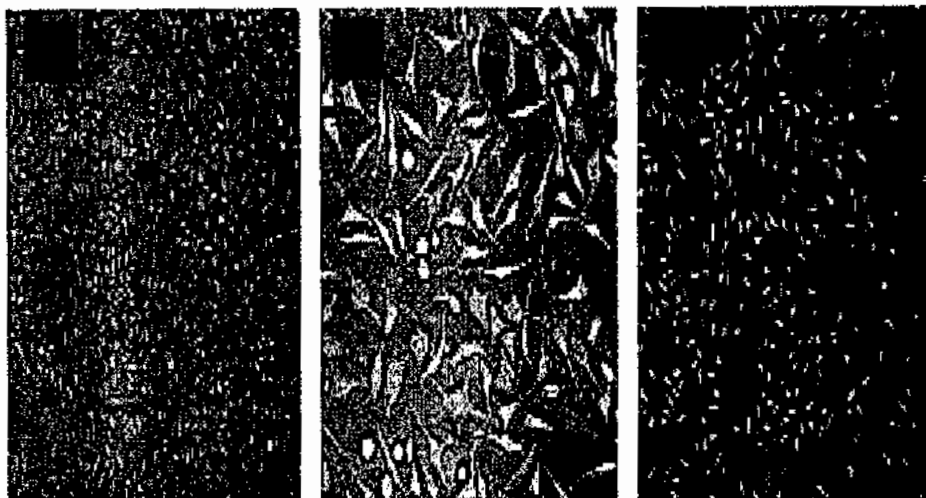
Figure 4.12 Phase contrast microscopy of SH-SY5Y cells treated with A) undoped, B) 2% Sn and C) 4% Sn doped ZnO nanostructures.

Chapter No. 5

Synthesis, Characterizations and Antibacterial Activity of Ag Doped ZnO Nanorods

5.1 Introduction

Recently, One-dimensional ZnO nanostructures such as nanowires, rods, tubes etc have fascinated enormous interest because of their potential as building blocks for novel nanodevices [132]. Excellent properties of one-dimensional ZnO nanostructures such as large exciton binding energy (60 meV), chemical and thermal stability, direct wide energy band gap (Eg = 3.37 eV), biosafety and biocompatibility ensure their applications in field-effect transistors, solar cells, lasers, biological and chemical sensors, photodiodes, optoelectronics, antibacterial coating and anti cancer agents [133-136]. Doping ZnO nanorods with suitable metal usually bring remarkable variations in morphology, electrical and optical characteristics. Silver (Ag) is considered to be excellent dopant for ZnO to tune its various properties such as electrical, optical and surface properties (i.e. oxygen vacancies and crystal defects) [137, 138]. Recently, Ozlem et al reported that Ag doping creates considerable amount of crystal defects in ZnO nanorods and as a result significantly enhances its photocatalytic activity [139]. Therefore, it is believed that it may also enhance the antibacterial activity of ZnO nanorods as crystal defects and oxygen vacancies can lead to enhanced generation reactive oxygen species (ROS), which play vital role in the antibacterial activity of a material [136]. Here $Ag_xZn_{1-x}O$ nanorods have been successfully fabricated via chemical co-precipitation technique and investigated their physical properties in detail. Also, effect of Ag content on the antibacterial characteristics of ZnO nanorods has been investigated.

5.2 Results and Discussions

5.2.1 Structural and morphological investigations

Figure 5.1(a) shows the XRD patterns of $Ag_xZn_{1-x}O$ samples synthesized by chemical co-precipitation technique. XRD patterns for $Ag_xZn_{1-x}O$ samples grown under the same synthesis conditions reveal the formation of single phase wurtzite structure of ZnO with no impurities related peaks.
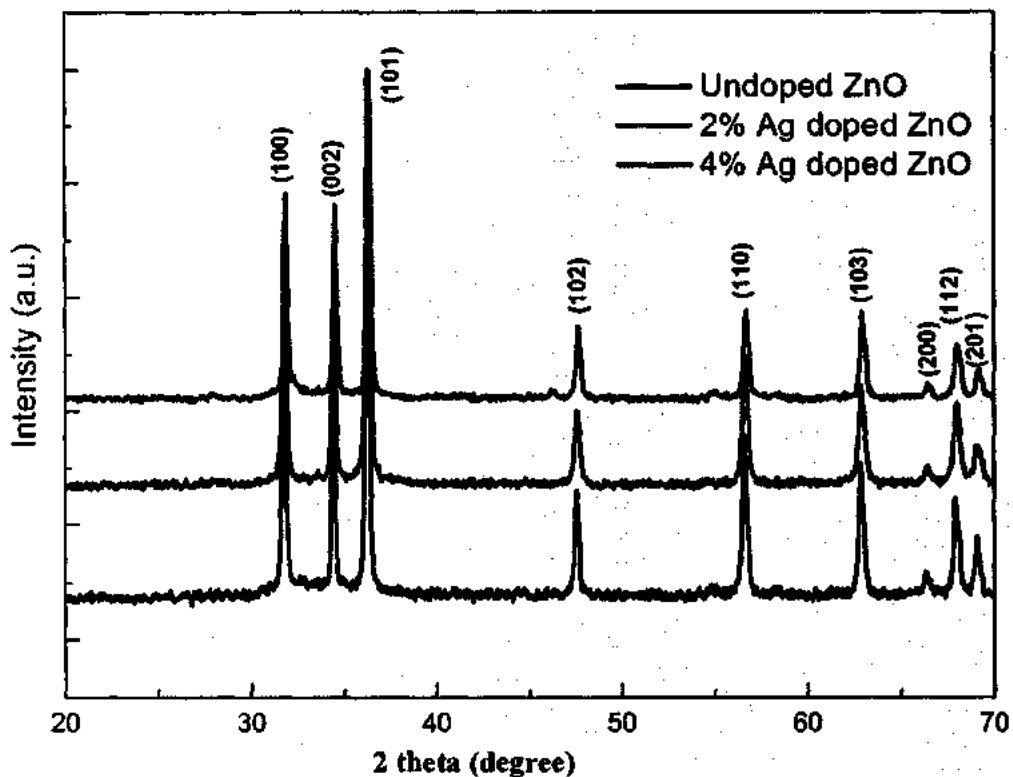
Figure 5.1(a) XRD patterns of $Ag_xZn_{1-x}O$ nanorods

According to previous reports, incorporation of Ag into ZnO matrix resulted in detectable peak shifts to comparatively lower or higher 2θ values [140] and segregation of Ag at particle boundaries of ZnO crystal resulted in no detectable shift [141]. Figure 5.1(b) depicts the extended XRD patterns of $Ag_xZn_{1-x}O$ samples. It is clear that, (101) peak of ZnO lattice shifts towards higher 2θ values with increase in Ag content, suggesting the successful incorporation of

62

Ag into ZnO host matrix. This peak shift may be attributed to the differences in ionic radii of Ag and Zn ions. To get more detailed structural analysis, lattice constants were calculated for all samples. Lattice constants "a" and "c" were calculated from (100) and (002) planes respectively, using following equations;

$$a = \frac{\lambda}{\sqrt{3}sin\theta}$$

$$\text{and } c = \frac{\lambda}{sin\theta}.$$

The lattice constants "a" and "c" are observed to decrease from 3.247 Å and 5.207 Å for undoped ZnO to 3.237 Å and 5.187 Å for 4% Ag doped ZnO. This decrease in lattice constants shows the successful incorporation of Ag into ZnO lattice.
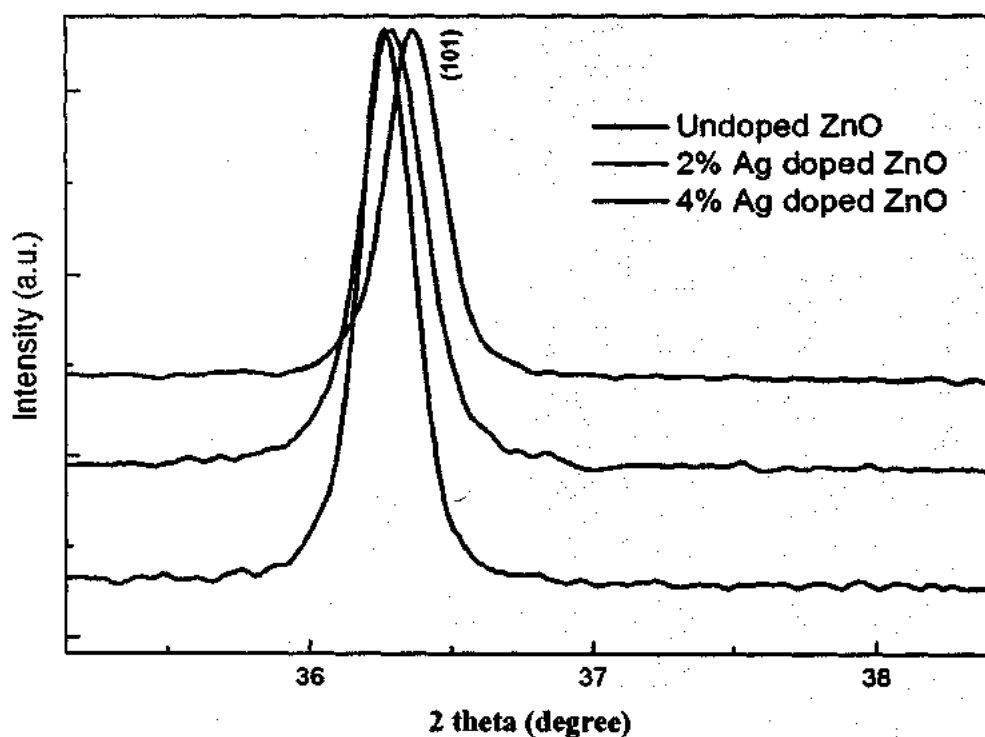
Figure 5.1(b) Extended XRD patterns of prepared nanorods

Surface morphology of the synthesized samples was studied using SEM. SEM images of $Ag_xZn_{1-x}O$ samples are shown in figure 5.2. Undoped ZnO sample exhibits rod like morphology with average diameter of 96 nm and average length of 700 nm. Ag content significantly influenced the morphology and diameter of ZnO nanorods as shown in figure 5.2(b).
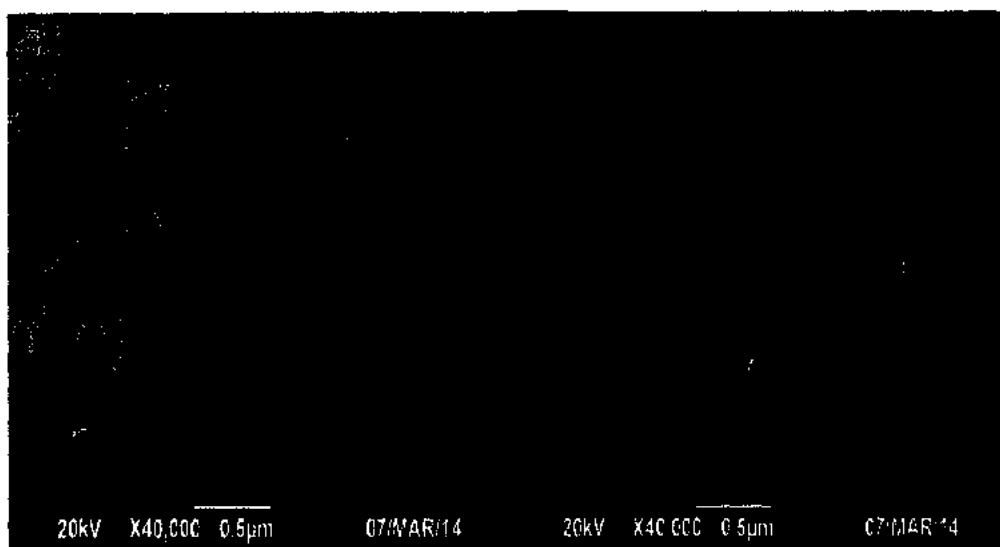
Figure 5.2 SEM images of a) Undoped ZnO b) 4% Ag doped ZnO

5.2.2 FTIR and Raman studies

The chemical nature of the prepared samples was examined using FTIR spectroscopy. FTIR spectra of ZnO nanorods doped with varying amount of Ag (i.e. 0, 2 and 4 at %) are shown in figure 5.3. The bands located at 3494 cm^{-1} may be assigned to O-H stretching vibrational mode, while bands located at 900 cm^{-1} represent the presence of N-O deformation vibration. The characteristic band of ZnO wurtzite structure appears at 489 cm^{-1} along with an additional band at 702 cm^{-1} for all samples. This additional band may be attributed to the fact that two absorption band appear in infrared region for one dimensional ZnO nanostructures [127]. FTIR spectra

64

exhibit no absorption bands related to AgO or AgO₂, which suggests high purity of the prepared samples and corroborate well with the XRD results.
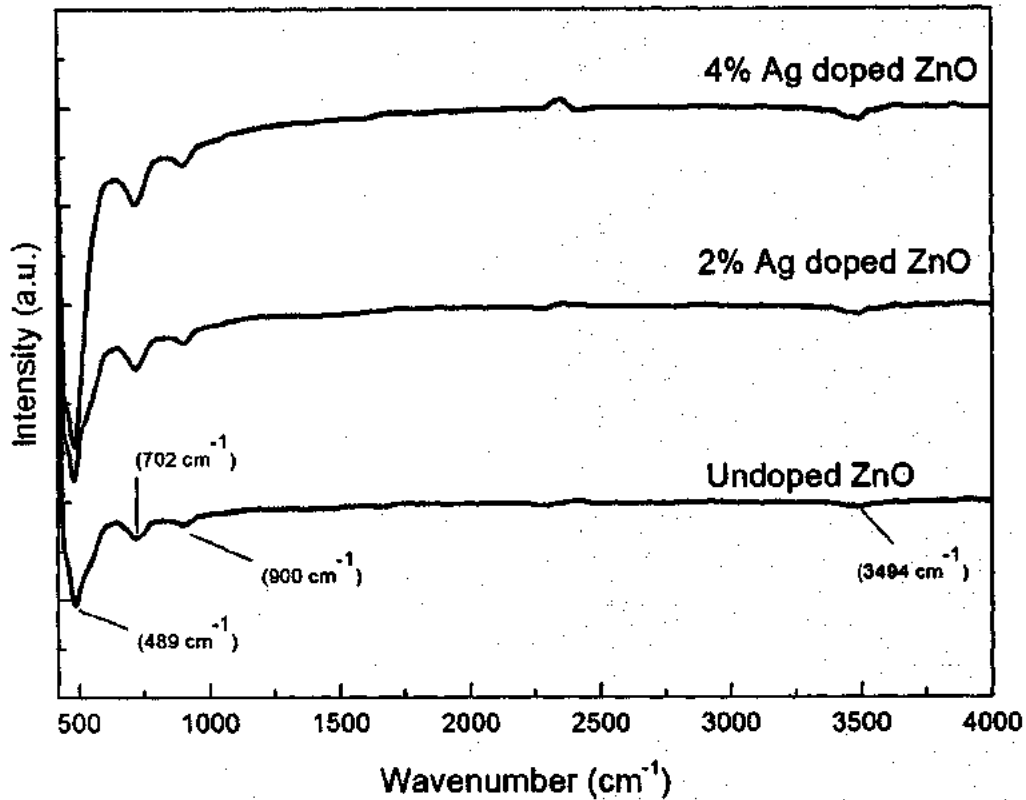
Figure 5.3 FTIR spectra of synthesized nanorods

Raman spectroscopy is considered to be an effective tool to probe the microscopic structure and vibrational properties of nanorods. It has the capability to notice the presence of minor phases in the sample which are not easy to detect with help of XRD. Figure 5.4 depicts the Raman spectra of $Ag_xZn_{1-x}O$ nanorods. Raman spectra of $Ag_xZn_{1-x}O$ nanorods exhibit four predominant Raman modes centered at 328, 385, 434 and 574 cm⁻¹. Raman modes centered at 328, 385 and 434 cm⁻¹ could be assigned to E_{2H}-E_{2L}, A_1^{TO} and E_{2H} phonons modes, respectively. 434 cm⁻¹ is the most intense peak in all samples and is the characteristic peak of wurtzite

structure of ZnO [66]. The Raman peak centered at 574 cm^{-1} belongs to E_1^{LO} mode and is significantly red shifted as compared to characteristic wurtzite phase peak (580 cm^{-1}). As this peak is largely associated with defects therefore a red shift clearly suggests the presence of large number of defects such as Zn interstitial and oxygen vacancies [142]. The peak is further red shifted with Ag doping which suggests enhancement in the number of defects with Ag doping into ZnO host matrix [143]. Absence of peaks related to Ag dopant rules out the secondary cluster formation and confirms the successful incorporation of Ag into ZnO host matrix. Raman spectroscopy results corroborate well with XRD and FTIR results.
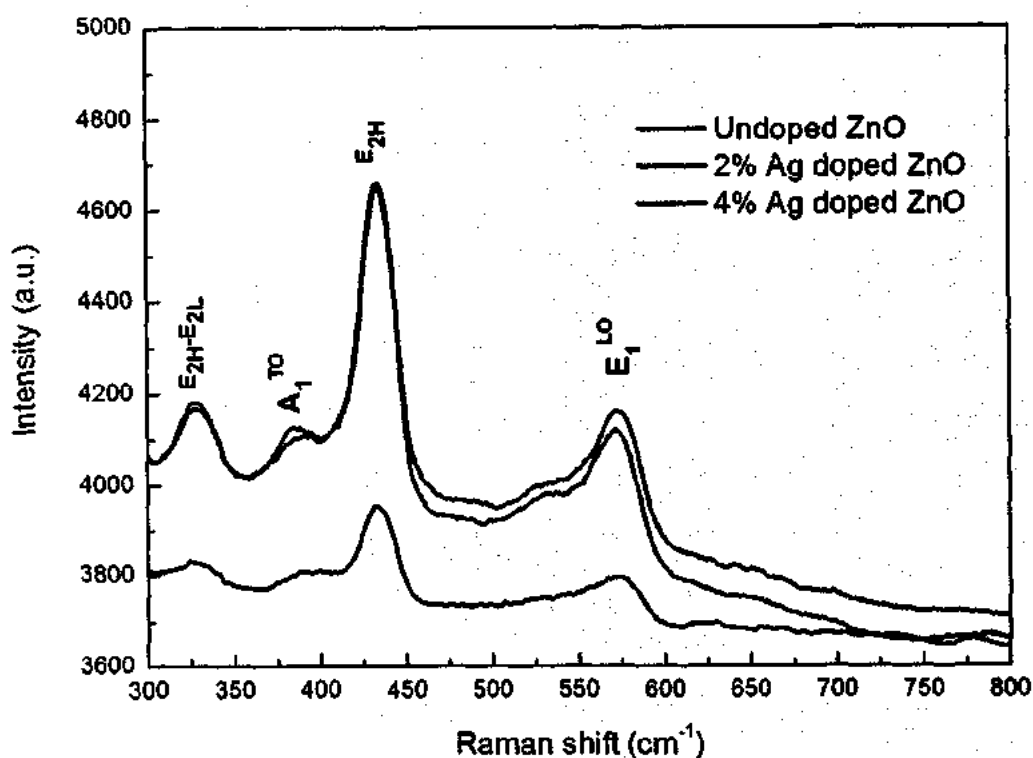
Figure 5.4 Raman spectra of Ag$_x$Zn$_{1-x}$O

5.2.3 Optical study

UV-visible spectroscopy technique was employed to investigate the influence of Ag doping on the optical properties of ZnO nanorods. Figure 5.5 exhibits the UV-visible absorption

spectra of $Ag_xZn_{1-x}O$ nanorods. Undoped ZnO exhibits typical band gap absorption peak centered at 374 nm (3.31 eV) related with wurtzite crystal structure of ZnO [144]. For 2% and 4% Ag doped ZnO nanorods exhibits typical band gap absorption peak is centered at 378 nm (3.28 eV) and 376 nm (3.29 eV), which are red shifted comparing to undoped ZnO nanorods. This red shift may be understood on the basis of quantum size effects, as it can be seen in SEM images that nanorods diameter increases with the Ag doping. Furthermore, it is reported that substitution of Ag^+ ions into Zn^{2+} sites results in red shift of typical band gap absorption peak of ZnO nanorods [145].
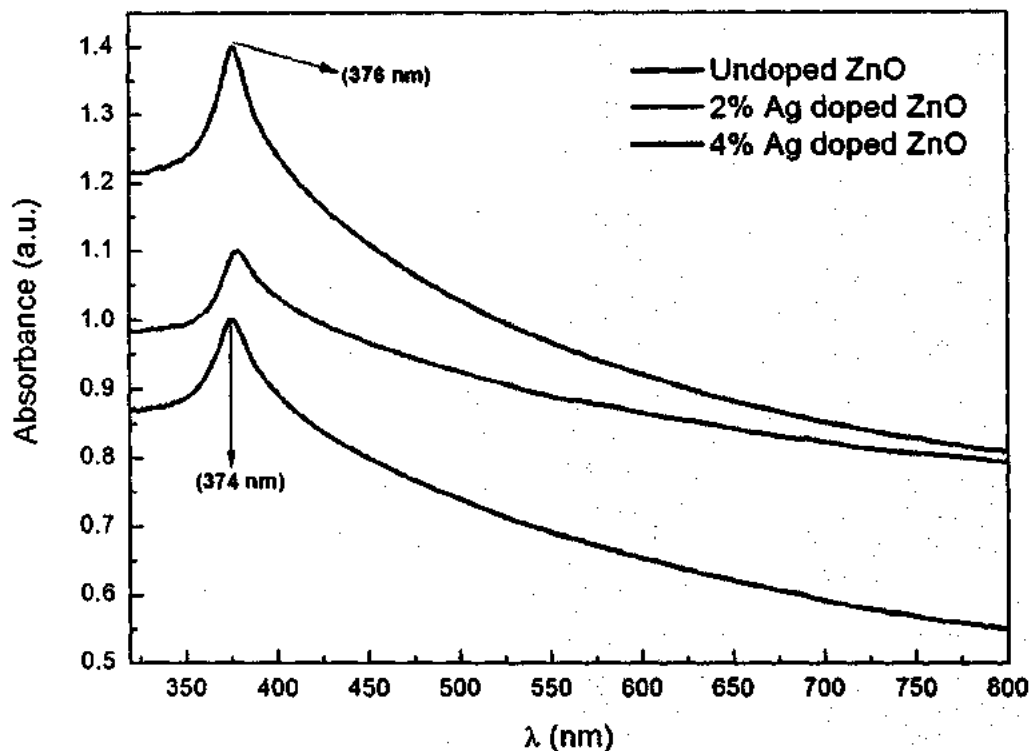
Figure 5.5 UV-visible spectra of prepared nanorods

5.2.3 Antibacterial activity

To determine and investigate the influence of Ag doping on antibacterial activity of the prepared ZnO nanorods against E. coli, S. aureus and Pseudomonas aeruginosa; their colloidal

suspensions were treated with the respective bacterial strains. $Ag_xZn_{1-x}O$ nanorods exhibit antibacterial activity towards all the bacterial strains tested as shown in figure 5.6. The ZOI against all the three pathogenic bacteria tested increases significantly with Ag doping as shown in the bar graph figure 5.7. Ag doping increases the ZOI up to 50%, 50% and 350% against *E. coli*, *S. aureus* and *Pseudomonas aeruginosa* respectively. The ZOI is measure of bactericidal potency of materials. Hence, remarkable increase in ZOI suggests huge enhancement in the bactericidal potency of ZnO nanorods with Ag doping.

To further evaluate the antibacterial activity of the prepared nanorods, growth inhibition study or time kill essay was employed. Figure 5.8 (a), (b) and (c) shows the growth curves of *E. coli*, *S. aureus* and *Pseudomonas aeruginosa* in the presence of $Ag_xZn_{1-x}O$ nanorods. Control sample i.e. bacteria grown in the absence of nanorods is also provided for comparison. *E. coli* growth is inhibited to some extent by undoped ZnO nanorods and growth inhibition is further increased by 2% Ag doping. But, 99% *E. coli* growth is inhibited when it is grown in the presence of 4% Ag doped ZnO nanorods as depicted in figure 5.8 (a). Undoped ZnO rods seem to be more effective against *S. aureus*, and inhibits 60 % growth rate of it. While, 4% Ag doped ZnO nanorods have inhibited 99% growth rate of *S. aureus* as shown in figure 5.8 (b). Ag doping has been found also effective against *Pseudomonas aeruginosa* as 4% Ag doped nanorods inhibited its 99% growth rate as depicted in figure 5.8 (c). It is concluded from the time kill assay test that among all prepared nanorods, 4% Ag doped ZnO nanorods sample is most effective against all the bacterial strains tested, which is also the case in disc method.
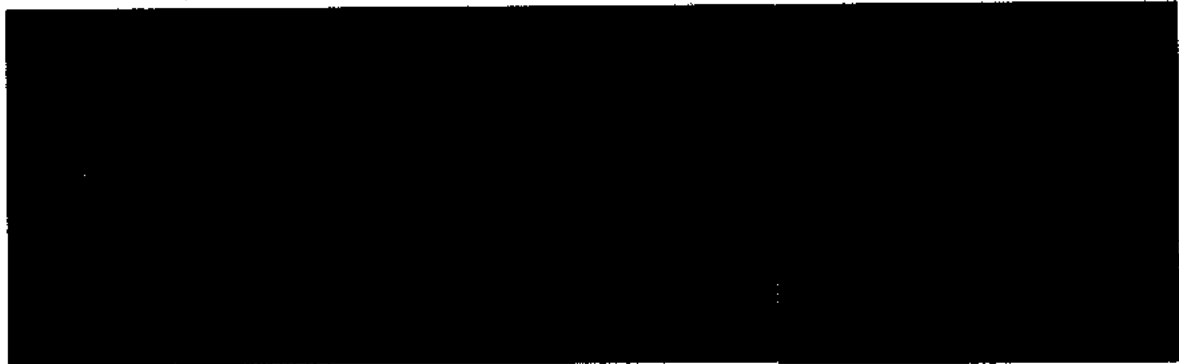
(A) *E. coli*
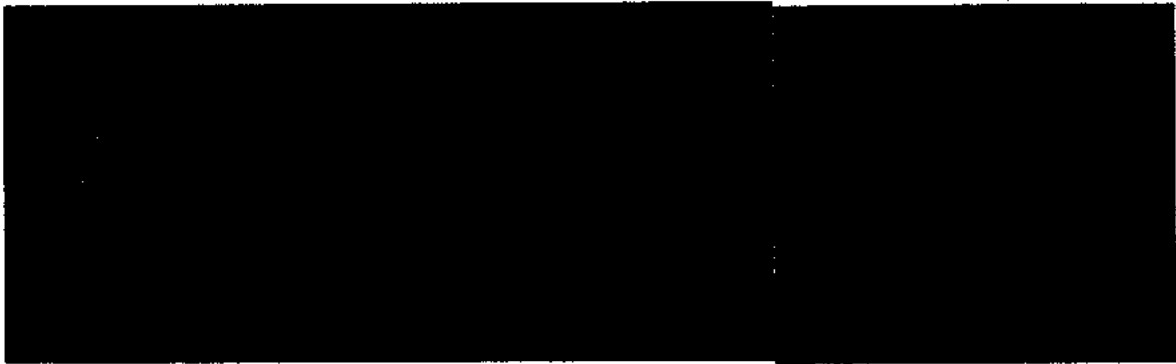
(B) *S. Aureus*

(C) *Pseudomonas aeruginosa*

Figure 5.6 Antibacterial activity of i) undoped ii) 2% Ag doped and iii) 4% Ag doped ZnO nanorods assessed by disc method
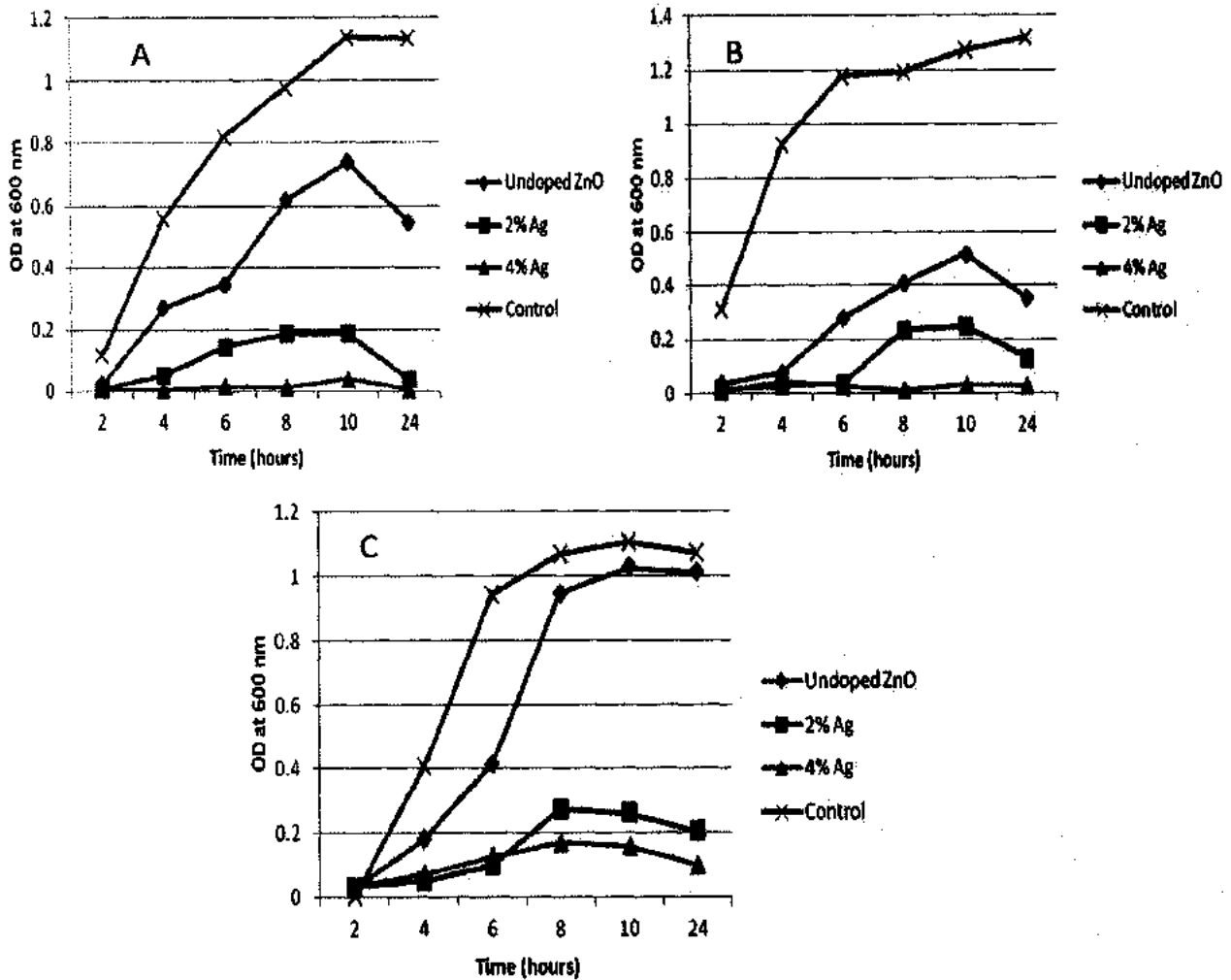
Figure 5.7 Effect of $Ag_xZn_{1-x}O$ nanorods on the growth rate of A) E. coli B) S. aureus C) P. aeruginosa strain.

Two possible mechanisms are suggested by several studies regarding the interaction of ZnO nanomaterials and bacteria. Firstly, decomposition of ZnO results in formation of reactive oxygen species (i.e. H_2O_2, hydroxyl radicals, singlet oxygen and Zn^{2+} ions), which leads to harmful interaction with bacteria and causes their death. Secondly, ZnO nanomaterials can accumulate on the surfaces of bacteria and cause disruption of cellular function and disorganization of cellular membranes. So, the antibacterial activity of the prepared ZnO

nanorods may be due to the mentioned mechanisms individually or accumulatively [113]. Mostly it is believed that with the reduction of particle size the antibacterial activity of ZnO enhances, on contrary to our results [81, 75]. Only a few reports are available in the literature on the doping effects on antibacterial activity of ZnO. A.H. Shah et al. have reported higher bioactivity of Ag doped ZnO nanostructures against *M. leutus* and *K. pneumonia* bacteria, which is attributed to decreased particle sizes [146]. I. Matai et al. also observed enhanced antibacterial activity of Ag-ZnO nano-composite [147]. But in our case the diameter of nanorods is found to increase with the increase in Ag doping as shown in the SEM images. This contradiction may be explained through the incorporation of Ag dopant into ZnO host matrix, compensating for particle size effects. Ag doping into ZnO matrix is reported to increase the Zn^{2+} ions release in water participate effectively in the antibacterial activity [147]. With the substitution of Ag ions on the sites of Zn ions in host matrix, an increased number of Zn ions are expected on interstitial sites. The Zn ions can be more easily released from interstitial sites than from their native sites. Moreover in Ag doped ZnO samples, Ag^{+} ions release may also be possible which may enhance their antibacterial activity. As from Raman spectroscopy results, it can be seen that Ag doping results in abundance of defects such as oxygen vacancies and Zn interstitial defects in ZnO nanorods. These ions may lead to bacteria cell death via strong electrostatic interactions with the positively charged cell membranes. Furthermore, defects may increase the formation of ROS surfaces of Ag doped ZnO nanorods [139] and which can enhance the antibacterial activity considerably. It has been reported that ZnO can be activated by visible light to enhance the electron-hole pair generation [148]. Upon reaction with water molecules, these holes can generate ROS via mechanism discussed by A.H. Shah et al. [149]. But the problem is recombination of electron-hole pair, which can reduce the ROS generation. However, defects in

ZnO crystal may trap the electron produced and the recombination of electron-hole pair may effectively be inhibited [150]. Hence, the presence of defects will lead to high degree of ROS generation. These ROS can penetrate the bacteria cell wall and cause their death [149]. So, from these discussions it may be concluded that antibacterial activity of ZnO nanorods increases with the increase in Ag content which may be attributed to Zn/Ag ions release and defects.

5.2.5 Cytotoxicity

The understanding of biosafety and biocompatibility of nanomaterials is of immense interest especially when they are being used for health related applications. Therefore, the cytotoxicity of the prepared nanorods has been investigated towards *SH-SY5Y* cells. Figure 5.8 shows the cell viability of $Ag_xZn_{1-x}O$ nanorods. It can be seen from the figure that the prepared nanorods do not influence the healthy cells viability.
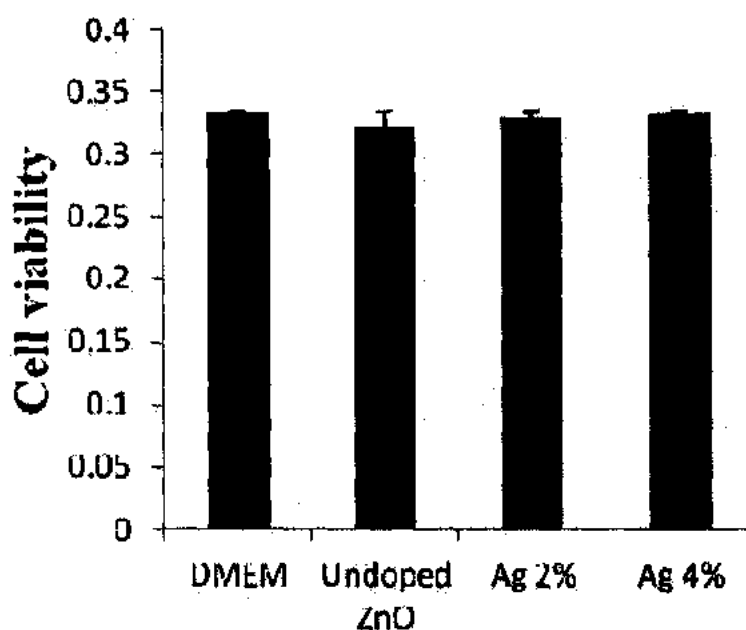
Figure 5.8 Effect of $Ag_xZn_{1-x}O$ nanorods on the viability of SH-SY5Y cells

To further evaluate the cytotoxicity, the prepared nanorods induced effects on the morphology of SH-SY5Y cells has been analyzed by phase contrast microscopy. It has been observed that both $Ag_xZn_{1-x}O$ nanorods have not influenced the healthy cells morphology as shown in figure 5.9.
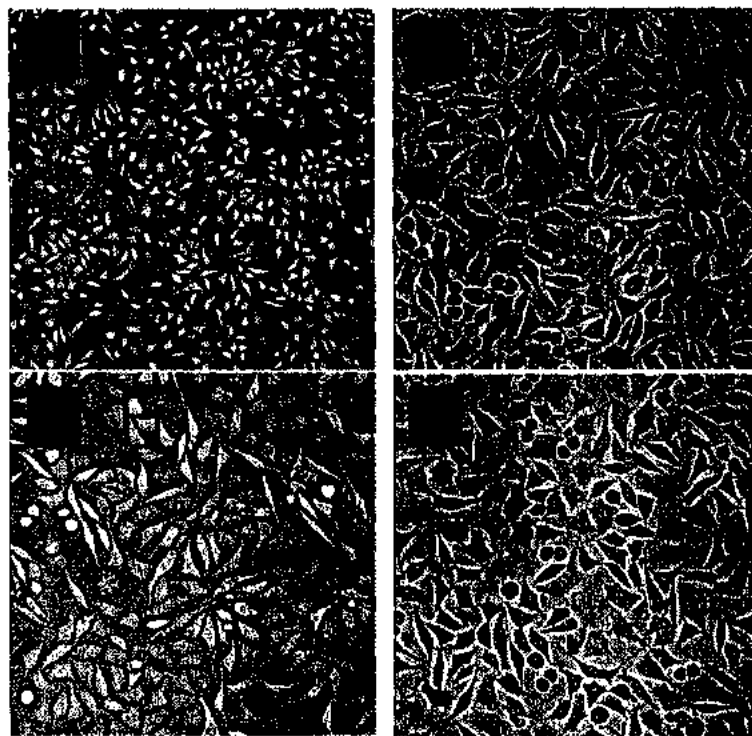
Figure 5.9 Cell morphology of SH-SY5Y cells after treatment A) Undoped, B) 2% Ag doped and 4% Ag doped ZnO nanorods

Chapter No. 6

Synthesis, Characterizations and Antibacterial Activity of Ni Doped ZnO Nanorods

6.1 Introduction

Transition metal doping into ZnO matrix is believed to be an effective tool to tune its various properties. Previously, it has been reported that optical and magnetic properties of ZnO nanorods can be tuned by transition metal doping [151, 152]. Ni is believed to be an excellent dopant for ZnO nanorods in order to change its different properties because of its unique stability at Zn^{2+} sites [153]. It has been reported that Ni doping into ZnO matrix may efficiently reduce the electron-hole pair recombination chances and lead to enhanced photocatalytic activity [154]. The inhibition of photogenerated electron-hole pair may also enhance their antibacterial activity. To the best of our knowledge, no work has been reported till date on the antibacterial study of Ni doped ZnO nanorods. Therefore, ZnO nanorods doped with varying amount of Ni synthesized by chemical co-precipitation have been investigated for certain physical properties and antibacterial activity.

6.2 Results and Discussions

6.2.1 Structural and morphological investigations

XRD technique has been used to investigate the phase purity and crystalline structure of the prepared samples. Figure 6.1(a) depicts the XRD patterns of $Ni_xZn_{1-x}O$ samples grown under the same synthesis conditions. All the diffraction peaks of $Ni_xZn_{1-x}O$ samples are well indexed to the single phase wurtzite structure of ZnO. The diffraction peaks intensities are observed to decrease with the increase in Ni concentration revealing that Ni doping slightly impede the crystallinity of ZnO.
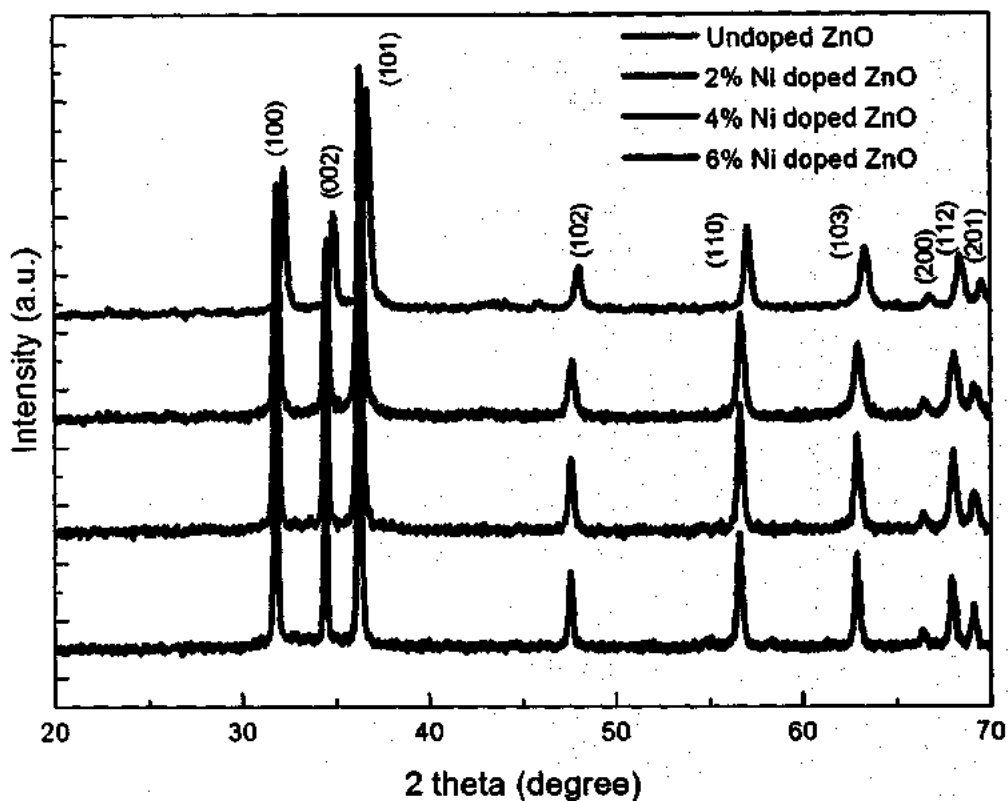
Figure 6.1(a) XRD patterns of $Ni_xZn_{1-x}O$ nanorods

Furthermore, the main (101) peak shifts towards higher angle with Ni doping as shown in the figure 6.1(b), which suggests the substitution of Ni^{2+} ions on the sites of Zn^{2+} ions. This peak shift is attributed to the changes in d-values or lattice constants with Ni doping as ionic radii of Ni^{2+} ions is smaller than Zn^{2+} ions [155]. In addition, no extra peaks related to Ni or any other impurities are found, which further confirms the successful incorporation of Ni dopant into ZnO host matrix. To get more detailed structural analysis, lattice constants "a" and "c" have been calculated from (100) and (002) planes respectively. The lattice constants "a" and "c" are found to decrease from 3.247 Å and 5.207 Å for undoped ZnO to 3.205 Å and 5.136 Å for 6% Ni doped ZnO. This decrease in lattice constants may lead to increase in the diffraction angle as compared to undoped ZnO.
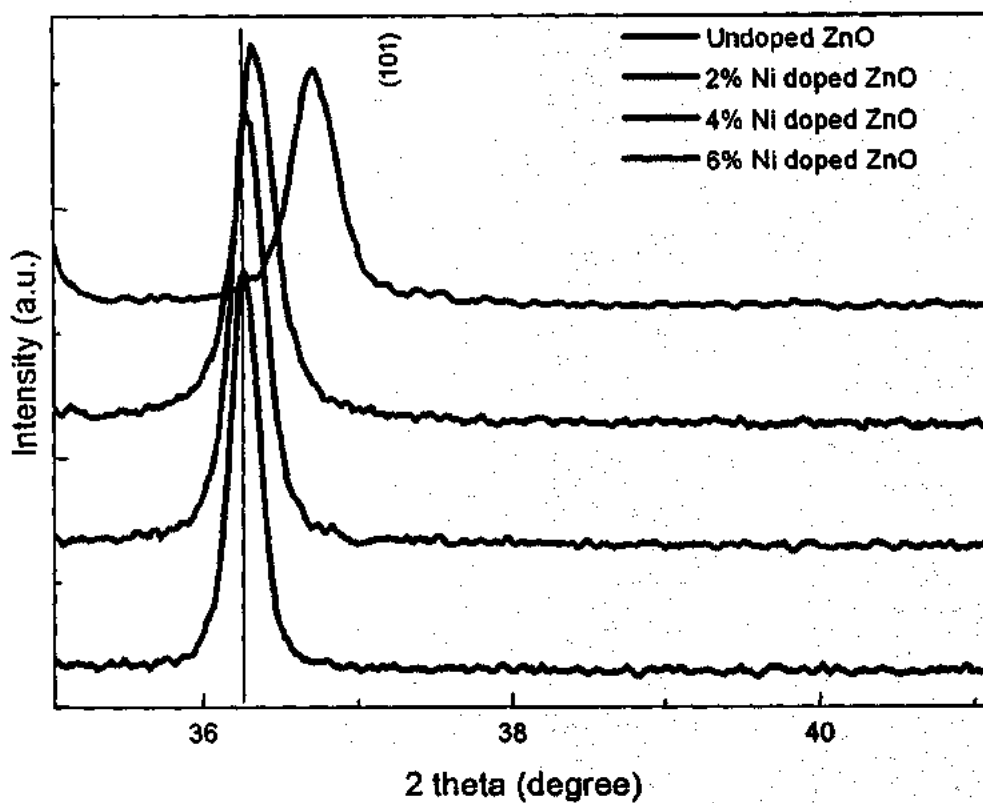
Figure 6.1(b) Extended XRD patterns of the prepared nanorods

The morphology of the synthesized samples have been carefully examined using SEM. Figure 6.2 (a), (b) and (c) depicts the SEM images of $Ni_xZn_{1-x}O$ samples. As-prepared ZnO sample exhibits rod like morphology with average diameter of 80 nm and average length of 1 μm. Interestingly, it is observed that prepared samples undergo significant variation in

diameter and length of ZnO nanorods with increase in Ni dopant concentration in ZnO host matrix. The 2% Ni doped ZnO sample has a morphology of nanorods with the average length of 800 nm and 110 nm diameter as shown in Figure 6.2 (a). With further increase of Ni dopant concentration, the length of nanorods further decreases and diameter increases as shown in figure6.2 (b) and (c).
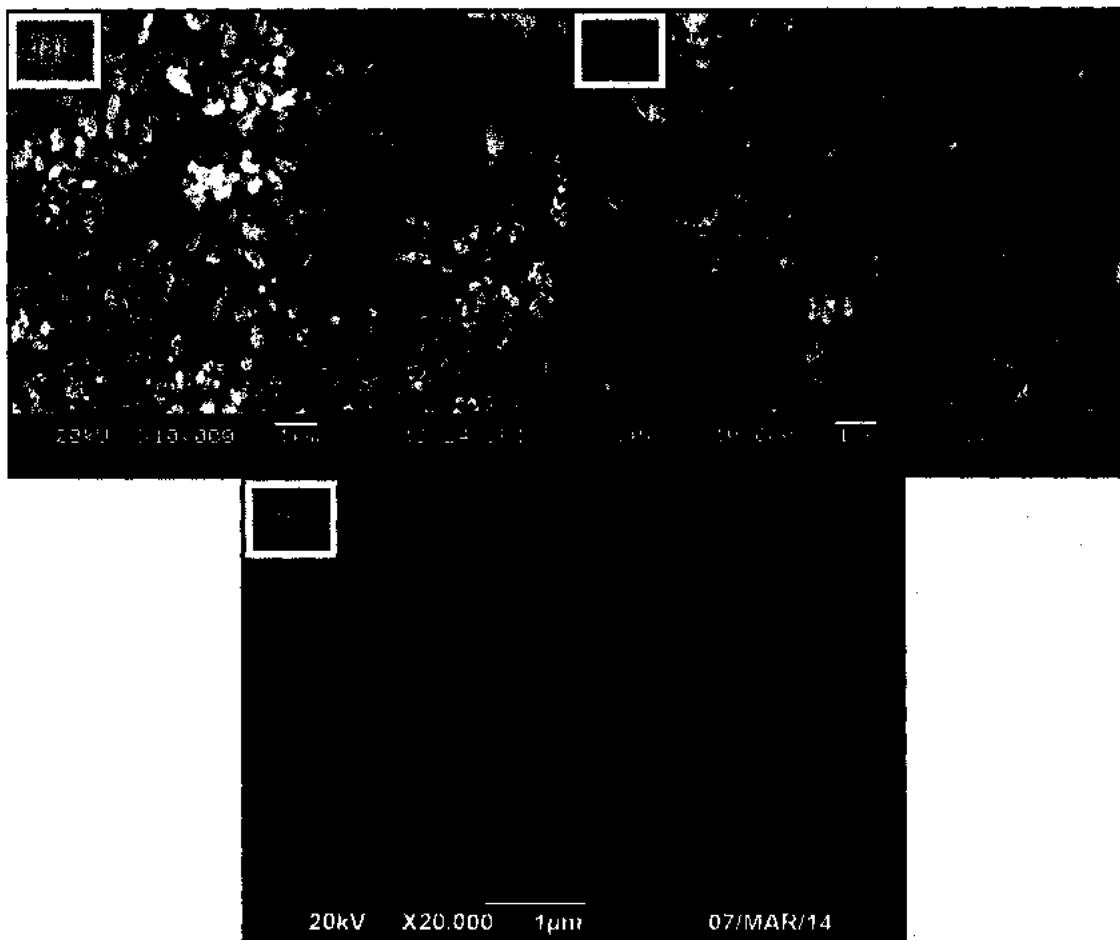
Figure 6.2 SEM images of a) 2% Ni doped, b) 4% Ni doped and c) 6% Ni doped ZnO

6.2.2 FTIR and Raman studies

The presence and absence of chemical vibrational modes on the surfaces of $Ni_xZn_{1-x}O$ nanorods have been examined by FTIR spectroscopy. FTIR spectra of ZnO nanorods doped with varying amount of Ni (i.e. 0, 2, 4 and 6 at %) are shown in figure 6.3. The small absorption band at 900 cm^{-1} corresponds to N-O deformation vibrational mode which might be due to the atmospheric nitrogen adsorption on the surfaces of synthesized nanorods. The characteristic band of ZnO wurtzite structure appears at 489 cm^{-1} along with an additional band at 702 cm^{-1} for all samples. Recently, it is reported that two absorption bands appear in IR region for ZnO nanorods. Hence, our FTIR results match very well with the reported one [127]. FTIR spectra lack absorption bands related to Ni-O band, which demonstrates high purity of the $Ni_xZn_{1-x}O$ nanorods and corroborate well with the XRD results.
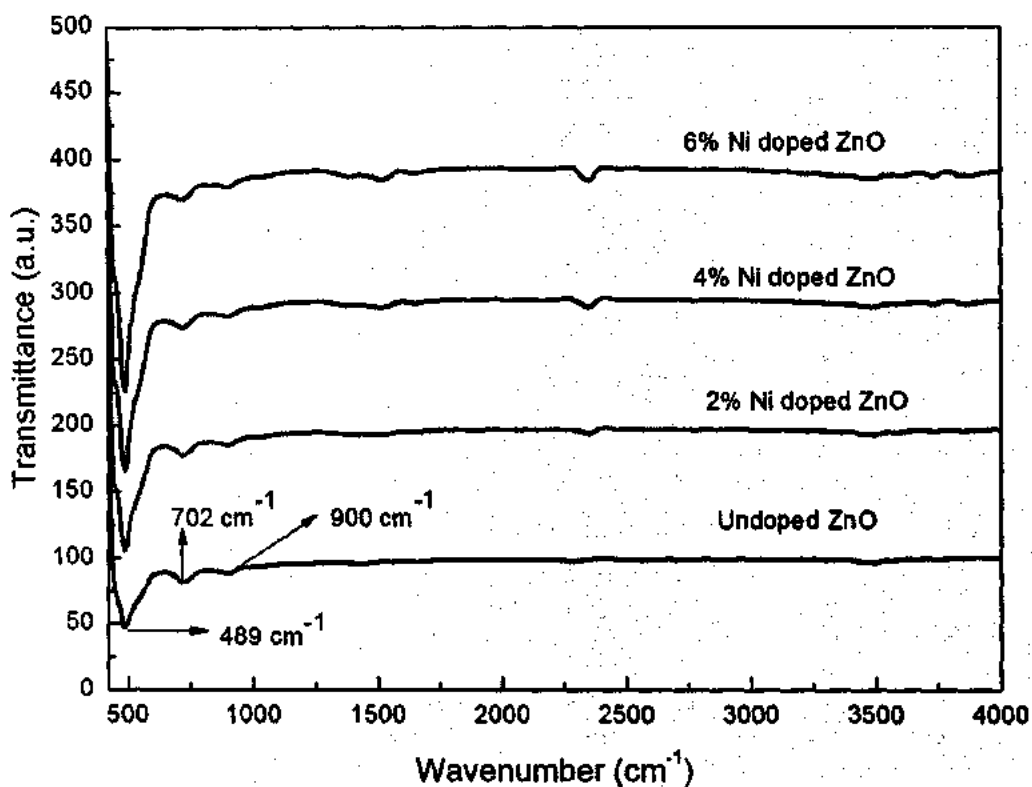
Figure 6.3 FTIR spectra of $Ni_xZn_{1-x}O$ ZnO nanorods

78
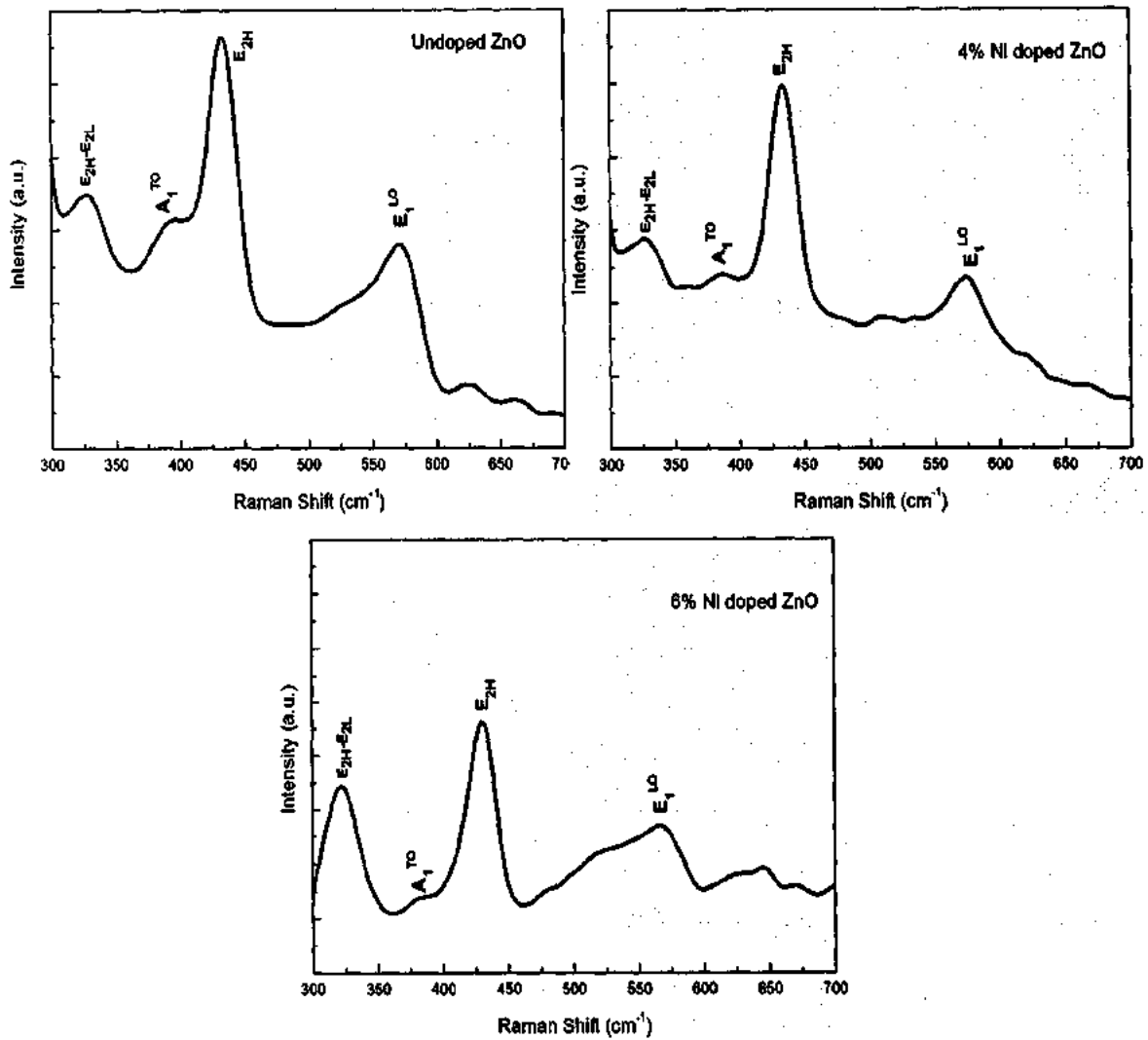
Figure 6.4 Raman spectra of $Ni_xZn_{1-x}O$ nanorods

Figure 6.4 depicts the Raman spectra of the $Ni_xZn_{1-x}O$ nanorods which shows a number

of Raman modes in the range of 300 to 800 cm^{-1}. In Raman spectra of undoped ZnO nanorods, a

predominant peak at 434 cm^{-1} corresponds to non-polar optical phonon mode of ZnO (i.e. E_{2H});

representing band characteristic wurtzite phase of ZnO [151, 152]. This E_{2H} band is present and

most dominant in Raman spectra of all samples revealing the formation of wurtzite phase ZnO

nanorods. The Raman modes centered at 328, 385, 434 and 574 cm^{-1} are assigned to E_{2H}-E_{2L},

79

A_1^{TO} and E_1^{LO} phonons modes respectively [150, 151]. It is very much clear from the Raman spectra of all doped nanorods that each and every peak in these spectra can be well matched with that of undoped nanorods. The absence of extra of modes in the Raman spectra of Ni doped ZnO nanorods demonstrate the successful incorporation of Ni into host matrix. There is only one difference in the Raman spectra of doped and undoped nanorods that is the broadening and red shifting of E_1^{LO} phonons mode band which is raised from the formation oxygen vacancies with the increase in the dopant concentration. The broadening and red shifting of the Raman mode may be attributed to the activation and formation of structural defects in $Ni_xZn_{1-x}O$ nanorods [142, 143].

6.2.3 Optical study

UV-visible absorption spectroscopy method has been employed to investigate the Ni doping induced effects on the optical characteristics of ZnO nanorods. The optical absorption spectra of the prepared $Ni_xZn_{1-x}O$ nanorods are shown in figure 6.5. The spectrum of pristine ZnO nanorods exhibit band edge absorption peak at 374 nm. The band edge absorption peaks of Ni doped ZnO nanorods shifts to longer wavelengths (red shifted). The 6% Ni doped ZnO nanorods band edge absorption peak is centered at 380 nm having red shift of 6 nm. Different authors explained that red shift in ZnO band edge absorption peak with transition metals doping could be attributed to sp-d spin exchange interactions between the band electrons of ZnO and the localized d-electrons of transition metal ions substituting the cation [156-159]. They explained that s-d and p-d exchange interactions could give rise to a negative and a positive correction to the conduction band and the valance band edges respectively, leading to the narrowing of band gap. Hence, it is concluded that Ni doping induced red shift in band edge absorption peak of ZnO in our case is due to sp-d exchange interactions.
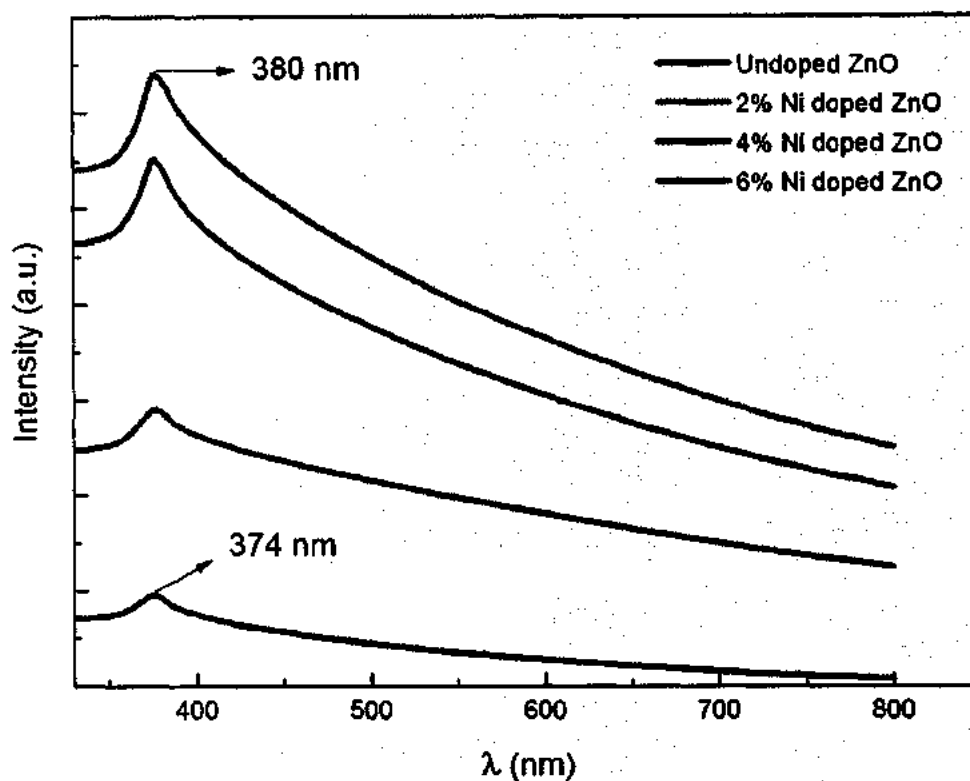
Figure 6.5 UV-visible absorption spectra of prepared nanorods

6.2.4 Antibacterial activity

The prepared $Ni_xZn_{1-x}O$ nanorods have been tested against clinically isolated Gram-negative Gram-positive bacteria by two different methods. Firstly, agar disc method has been employed to investigate the influence of Ni doping on ability of ZnO nanorods to rupture the bacterial cells. Antibacterial activity of ZnO nanorods against the *S. aureus* and *P. aeruginosa* bacteria is found to increase with Ni doping as indicated by the zone of inhibition (ZOI) they produced. As it can be seen from figure 6.6 that ZOI produced by ZnO nanorods increases with the increase in Ni dopant concentration. The observed ZOI for undoped ZnO nanorods is 6 mm and 12 mm against *S. aureus* and *P. aeruginosa* respectively, which is increased up to 14 mm and 16 mm for 6% Ni doped ZnO nanorods. On the other hand for the *E. coli* bacteria, ZOI produced by prepared nanorods slightly decreases with increase in Ni doping level. The observed

81

ZOI for undoped ZnO nanorods is 11 mm which is decreased up to 9 mm for 6% Ni doped ZnO nanorods.
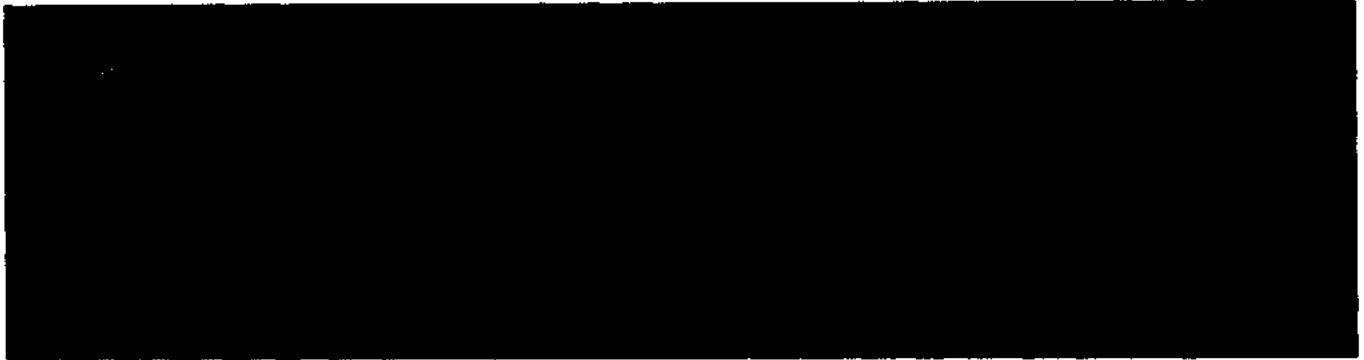
(A) *E. coli*

(B) *S. Aureus*
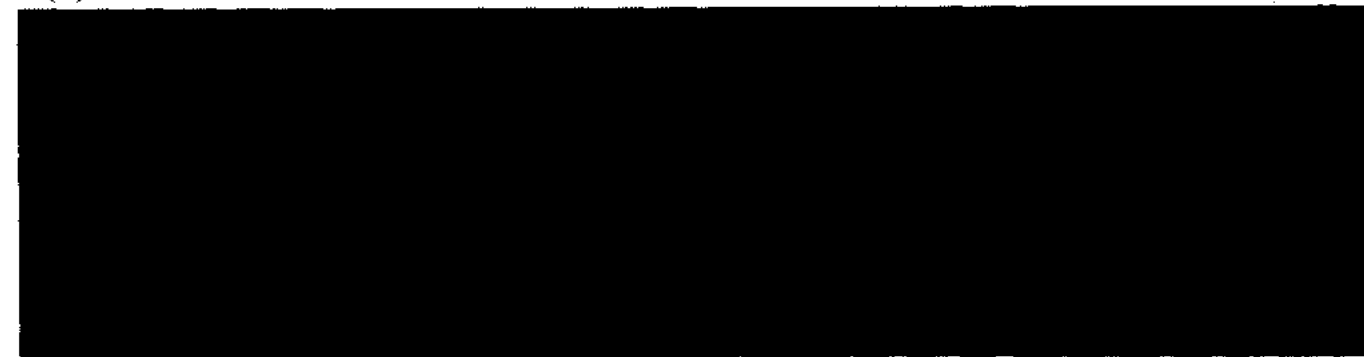
(C) *Pseudomonas aeruginosa*

Figure 6.6 Antibacterial activity of a) undoped b) 2% Ni c) 4% Ni and d) 6% Ni doped ZnO nanorods assessed by disc method

Secondly, time kill assay technique has been used to investigate the influence of Ni doping on growth inhibition ability of ZnO nanorods. *E. coli*, *P. aeruginosa* and *S. aureus*

bacterial strains growth curves have been recorded in the presence $Ni_xZn_{1-x}O$ nanorods. Figure 6.7 (a, b & c) shows the growth curves of *E. coli*, *P. aeruginosa* and *S. aureus* respectively after treating them with the prepared nanorods. Control sample i.e. without presence of prepared nanorods is presented for comparison. In case of *E. coli*, undoped ZnO nanorods limit its growth rate to some extent while Ni doped ZnO nanorods has very negligible effect on it. But, for *P. aeruginosa* and *S. aureus*, Ni doping is seen to be very much effective in inhibition of their growth rate. The 2% and 4% Ni doped ZnO nanorods inhibit almost 50% growth rate of *P. aeruginosa*. However, in the presence of 6% Ni doped ZnO nanorods no growth is observed. The growth rate of *S. aureus* decreases with Ni doping and diminishes on use of 4% and 6% Ni doped ZnO nanorods. Only few studies are reported on the antibacterial activity of metal doped ZnO nanostructures. M. Vasanthi et al. have reported enhancement in the antibacterial activity of nanocrystalline ZnO films via Sn doping [159]. X. Zhang et al. have observed 95.9% antibacterial potency of Sb doped ZnO nanostructures against *S. aureus* bacteria [160]. Enhanced antibacterial potency has been reported for Cr doped ZnO nanostructures [149]. Our results are more promising comparing to these studies as we have observed complete eradication of *P. aeruginosa* and *S. aureus* bacteria by application of 6% Ni doped ZnO nanorods.

Several mechanisms of inhibitory action are proposed for ZnO nanomaterials antibacterial activity. Firstly, the adherence of the nanomaterials on the surface of bacteria can lead to physical blockage of transport channels of the cells. This blockage of transportation in cell may lead to cell starvation and eventually its death [161]. Secondly, bacterial cell death is also caused by the oxidation of membranes lipids by excessive ROS production [162]. ROS could be produced on the surface of ZnO via light induced effects [163]. Recently, it is reported that white light is enough for producing electron-hole pair [164, 165].
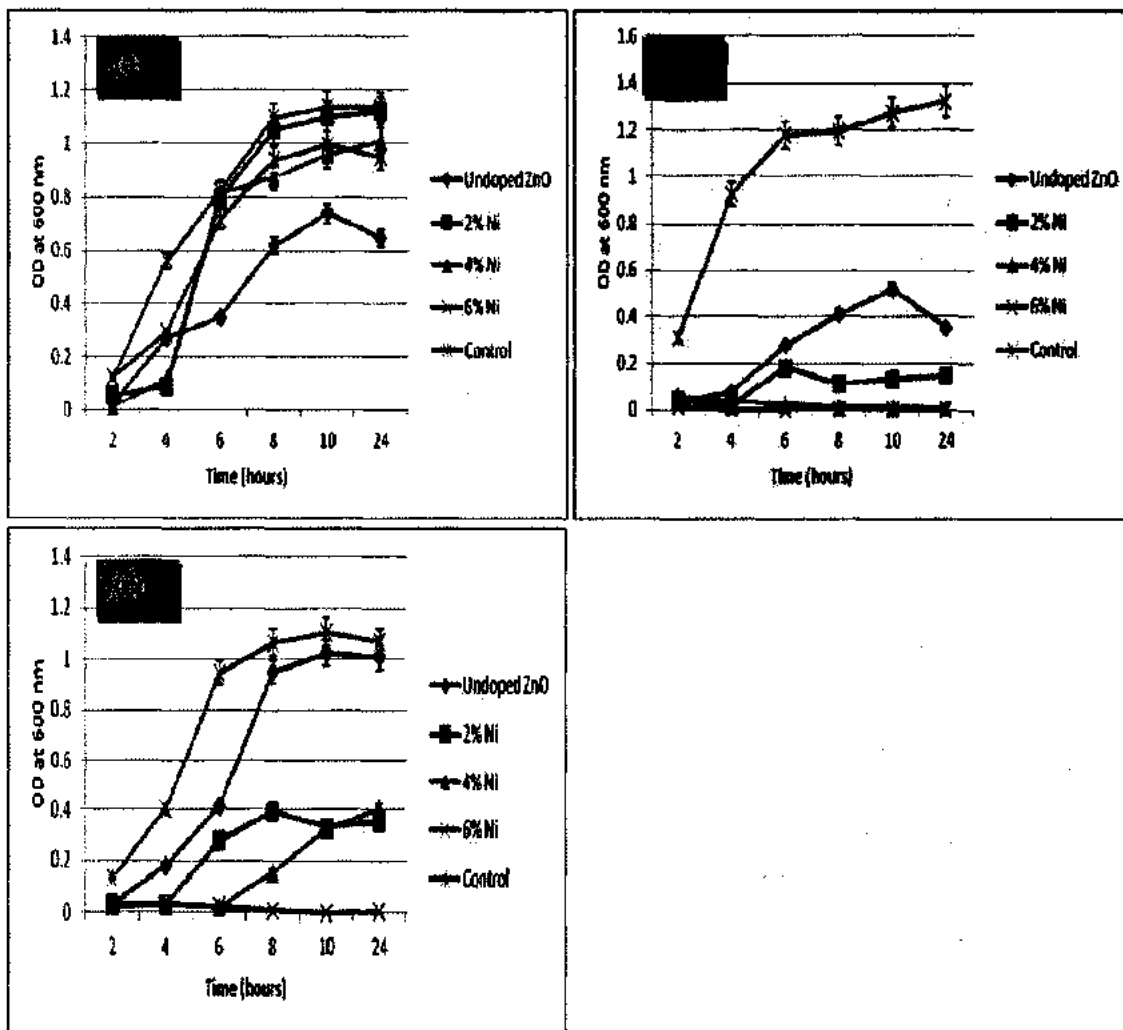
Figure 6.7 Effect of $Ni_xZn_{1-x}O$ nanorods on the growth rate of a) *E. coli*, b) *S. aureus* and c) *Pseudomonas aeruginosa* strains

ROS can be produced by the interaction of photo generated holes with water molecules through a mechanism explained by A.H. Shah et al. [149]. However, this ROS production is strongly influenced by the recombination of photo generated electron-hole pairs. But if this recombination is inhibited then excessive ROS can be produced by ZnO nanostructures. Recently, it is reported by some research groups that the presence of structural defects in the system can inhibit this recombination process by acting as trapping centers for photo generated electrons [139, 154]. As it can be seen from Raman spectroscopy results that large number of

defects are introduced in ZnO nanorods with Ni doping. Hence, presence of large number of defects may lead to higher antibacterial activity of $Ni_xZn_{1-x}O$ nanorods. In order to confirm whether the enhanced antibacterial activity of doped nanorods is due to photo induced effects or not, we have recorded the growth curves for all the bacteria in dark in the presence of synthesized nanorods colloidal suspensions. From these results, it is observed that antibacterial activity of Undoped ZnO nanorods in dark is much lower than that observed in normal laboratory light conditions. Furthermore, Ni doping slightly decreases the antibacterial activity of ZnO nanorods in dark conditions which may be due to the larger diameter of doped ZnO nanorods comparing to undoped. Hence, it is confirmed that photo induced ROS generation play important role in the antibacterial activity of the synthesized nanorods.

Secondly, it is reported in the literature that the antibacterial potency of ZnO nanorods may linked to the amount of free Zn^{2+} ions in the solution [110]. Furthermore, it is suggested that the abundance of Zn^{2+} ions in ZnO nonmaterial's solution may be significantly enhanced by metal doping [159]. When metal ions are doped into ZnO matrix, then dopant ions may push the Zn^{2+} ions towards interstitial sites. The release of Zn^{2+} ions from interstitial sites is effortless in comparison with their release from local sites. Hence, release of more Zn^{2+} ions in doped ZnO nanorods solution as compared to undoped nanorods is logical. Therefore, the increase in the antibacterial potency of ZnO nanorods against *P. aeruginosa* and *S. aureus* may be credited to enrichment in ROS generation and Zn^{2+} ions with Ni doping. Here, a question arises that why antibacterial activity of ZnO nanorods towards *E. coli* does not increase with Ni doping. On the basis of direct interactions of nanorods, it can be understood because diameter of nanorods decreases with Ni doping which may to some extant reduces ZnO capability against *E. coli*. But why the same effect is not seen against *Pseudomonas aeruginosa* and *S. aureus*. This difference

in the antibacterial activity of Ni doped ZnO nanorods against different bacterial strains may be due to the difference in cell wall integrity or membrane structure of the respective bacterium. Also, various bacterial strains have significantly different infectivity and tolerance towards different agents including antibiotics [159]. Recently, A. Jain et al reported that $E.\ coli$ bacterium is more resistant to ROS generation as compared to $S.\ aureus$ because of the presence of extra outer membranes and lipopolysaccharide in $E.\ coli$, which are not present in case of $S.\ aureus$ [165, 166]. Another report suggests that $S.\ aureus$ has smaller negative charge as compared to $E.\ coli$, which would allow a high level of penetration of charged radicals into $S.\ aureus$ [166]. This would cause more damage and cell death of $S.\ aureus$ than $E.\ coli$.

6.2.5 Cytotoxicity

The SH-SY5Y cells have been used to probe the cytotoxic nature of the $Ni_xZn_{1-x}O$ nanorods on healthy cells. Figure 6.8 shows the cell viability of SH-SY5Y cells after treatment with the prepared nanorods. It is observed that the number viable healthy cells remain same after treatment for 24 hours. This demonstrates the biosafety and biocompatibility of the synthesized $Ni_xZn_{1-x}O$ nanorods.
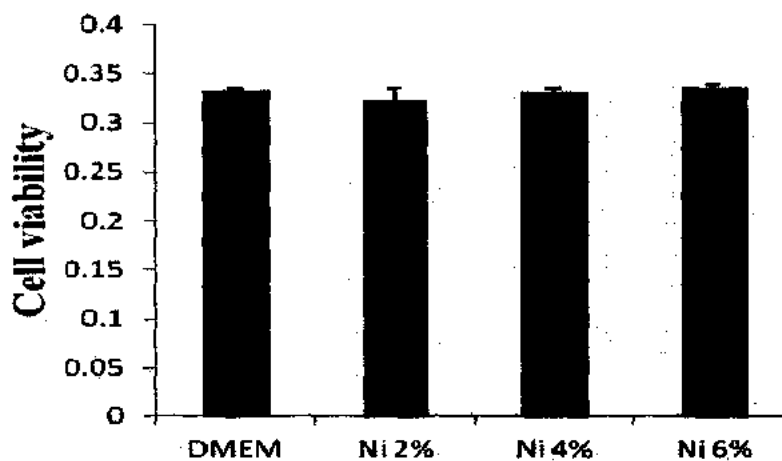
Figure 6.8 Effect of $Ni_xZn_{1-x}O$ nanorods on the viability of SH-SY5Y cells

Phase contrast microscopy has been employed to investigate the prepared nanorods induced effects on the SH-SY5Y cells morphology. It has been observed from figure 6.9 that the nanorods do not alter the cell morphology. Hence, the synthesized $Ni_xZn_{1-x}O$ nanorods may be considered as biosafe and biocompatible.
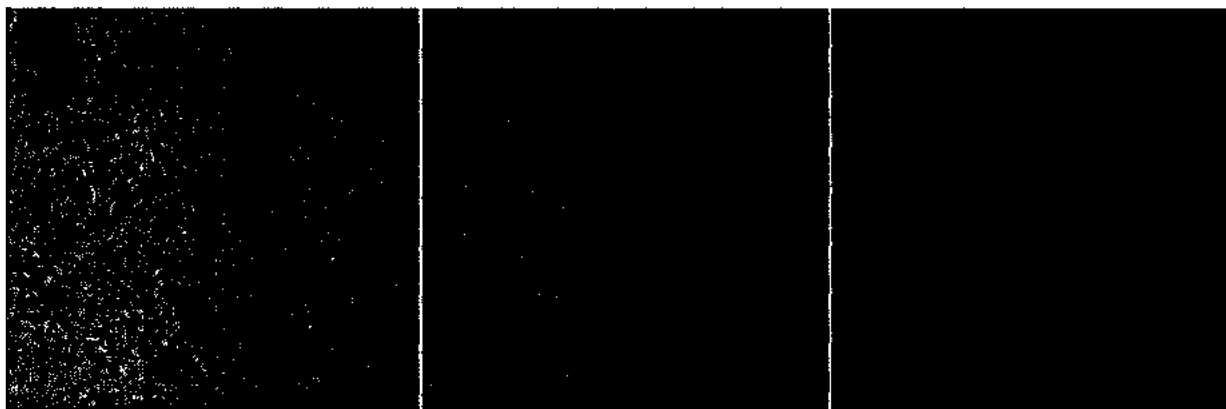
Figure 6.9 Cell morphology of SH-SY5Y cells after treatment with A) 2% Ni doped, B) 4% Ni doped and C) 6% Ni doped ZnO nanorods

Chapter No. 7

Synthesis, Characterizations and Antibacterial Activity of Ce Doped CuO Nanostructures

7.1 Introduction

CuO is an interesting multifunctional narrow band gap p-type semiconductor having tremendous physiochemical properties [36]. CuO can be readily mixed with polymers comparatively than the other metal oxides. The polymers mixed with CuO nanostructures can be used for dressing of wounds and coating of the hospital implants. This will effectively enhance the wounds healing rate and control the spreading of infectious diseases [86]. Various studies have demonstrated the antibacterial activity of CuO nanostructures [120]. Several mechanisms underlying the antibacterial activity of CuO nanostructures have been reported such as adherence to the bacterial cell, release of Cu ions and reactive oxygen species (ROS) generation on the surfaces of nanostructures [86]. The ROS generation is reported to be significantly increased by the creation of defects in the metal oxide structure [87]. The selective metal doping into metal oxide matrix can lead to the creation of large amount of structural defects (such as oxygen vacancies and interstitial defects) [167]. Only two studies are available in the literature about the doping induced effects on the antibacterial activity of CuO nanostructures. It has been reported in those papers that zinc doping of CuO nanostructures can lead to higher ROS production due to structural defects thereby increasing their antibacterial activity [86, 168]. But, Ce doping induced effects on the antibacterial activity of CuO nanostructures has not been yet reported. In this chapter, facile chemical synthesis of $Ce_xCu_{1-x}O$ nanostructures, their physical properties as well as antibacterial activity have been discussed.

7.2 Results and Discussions

7.2.1 Structural and morphological investigations

The structural characteristics of the prepared samples have been investigated through XRD. Figure 7.1 depicts the XRD patterns of $Ce_xCu_{1-x}O$ samples grown under the same synthesis conditions. From XRD data, only diffraction peaks of the CuO monoclinic structure can be found. No characteristic peaks are observed related to the secondary phases of ceria, hence confirming the formation of single phase CuO monoclinic structure for doped and undoped samples. The most intense peak i.e. (111), systematically shifts towards lower 2θ values with Ce doping (shown in the inset of figure 7.1) which reveals the successful doping of Ce ions into the host matrix.
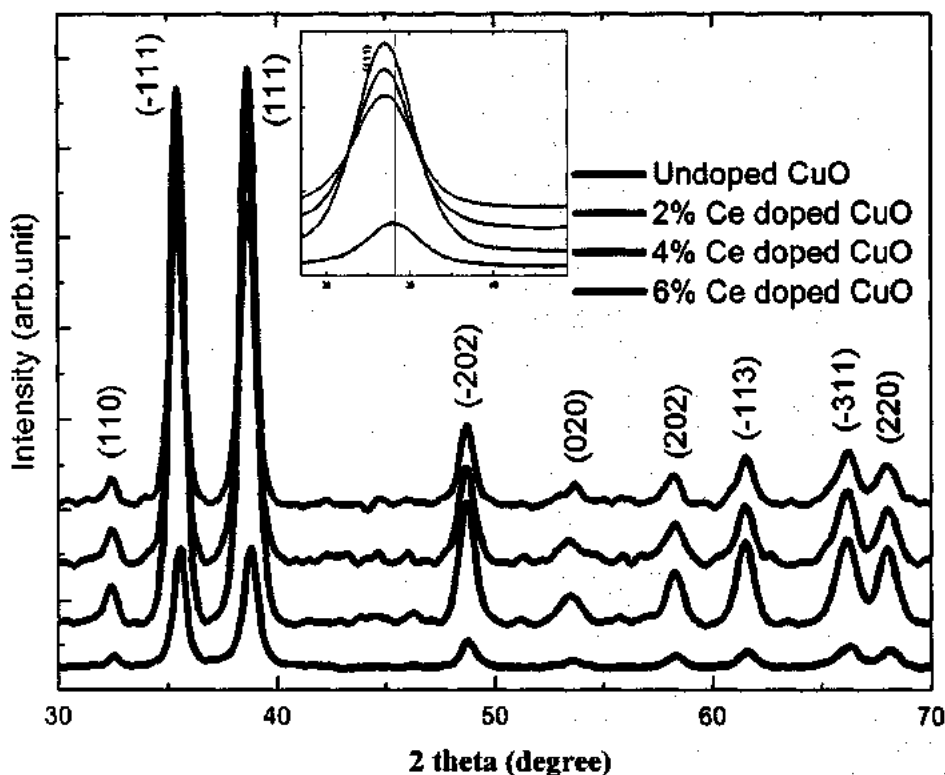
Figure 7.1 XRD patterns of the prepared samples

The morphology of the synthesized $Ce_xCu_{1-x}O$ samples have been examined through SEM. Figure 7.2(a-d) shows the SEM images of $Ce_xCu_{1-x}O$ samples. SEM images reveal the

formation of rod-like nanostructures having average diameter of 30 nm incase of undoped CuO. Interestingly, it is observed that upon Ce doping the morphology of CuO nanostructures is transformed into sheet-like nanostructures. The thickness of sheet-like nanostructures is observed to increases gradually with the increase in Ce doping concentration. This morphological transformation may be attributed to the successful incorporation of Ce ions into CuO matrix. The chemical reactivity of an element significantly increases with the decrease in Pauling electro-negativity [169]. The Pauling electro-negativity of Cu (1.9) is much higher as compared to that of Ce (1.1). Hence, Ce doping may enhance the growth rate of CuO nanostructures and cause morphological transformation.
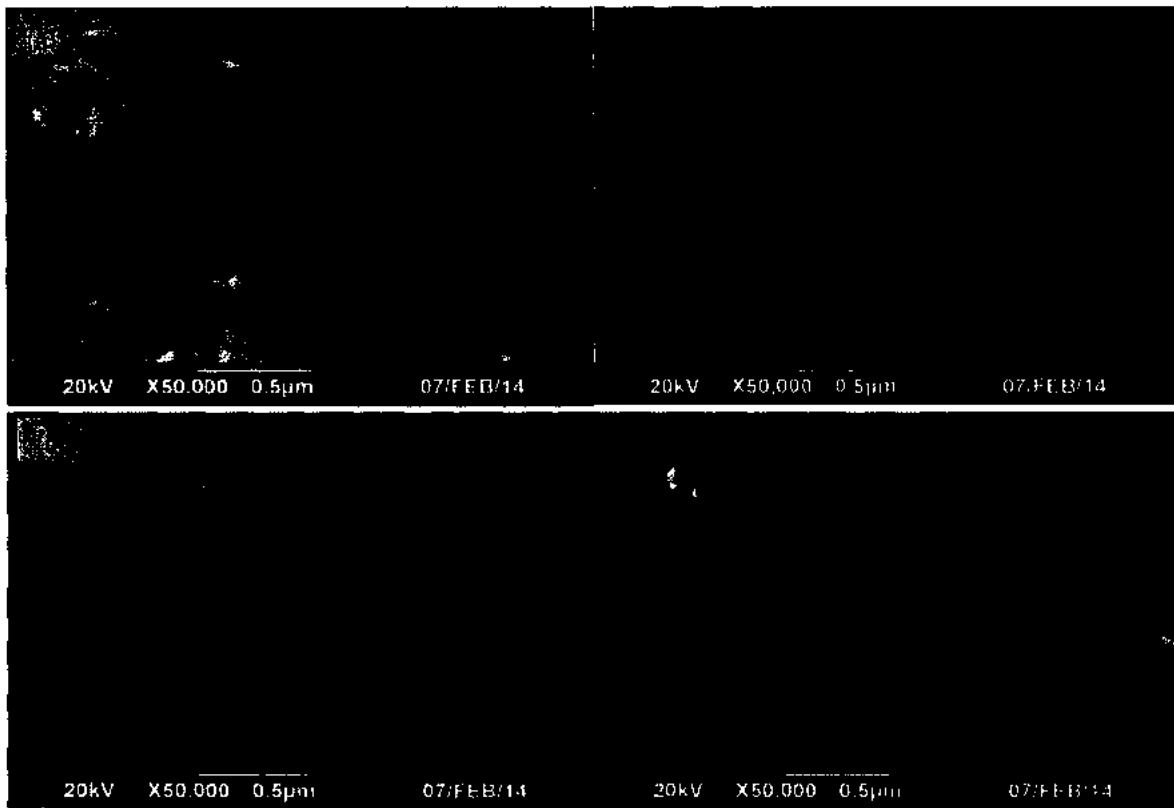
Figure 7.2 SEM images of (a) Undoped CuO, (b) 2% Ce, (c), 4% Ce and (d) 6% Ce doped CuO samples

7.2.2 FTIR and Raman investigations

The presence or absence of vibrational modes on the surfaces of the prepared nanostructures has been investigated using FTIR analysis. Figure 7.3 depicts the FTIR spectra of the synthesized nanostructures. FTIR spectra of CuO nanostructures show single characteristic strong peak at 529 cm^{-1} associated with Cu-O stretching vibrations of monoclinic CuO, which match very well with the reported values [169]. With the Ce doping, this mode undergoes systematic blue shift towards 537 cm^{-1}. The blue shift in IR band with Ce doping may be linked with the variation in surface defects [170]. Furthermore, vibrational modes related to Cu_2O, and CeO_2 are not detected confirming that all the prepared samples comprise of purely monoclinic CuO phase. Thus FTIR analysis confirms the XRD results.
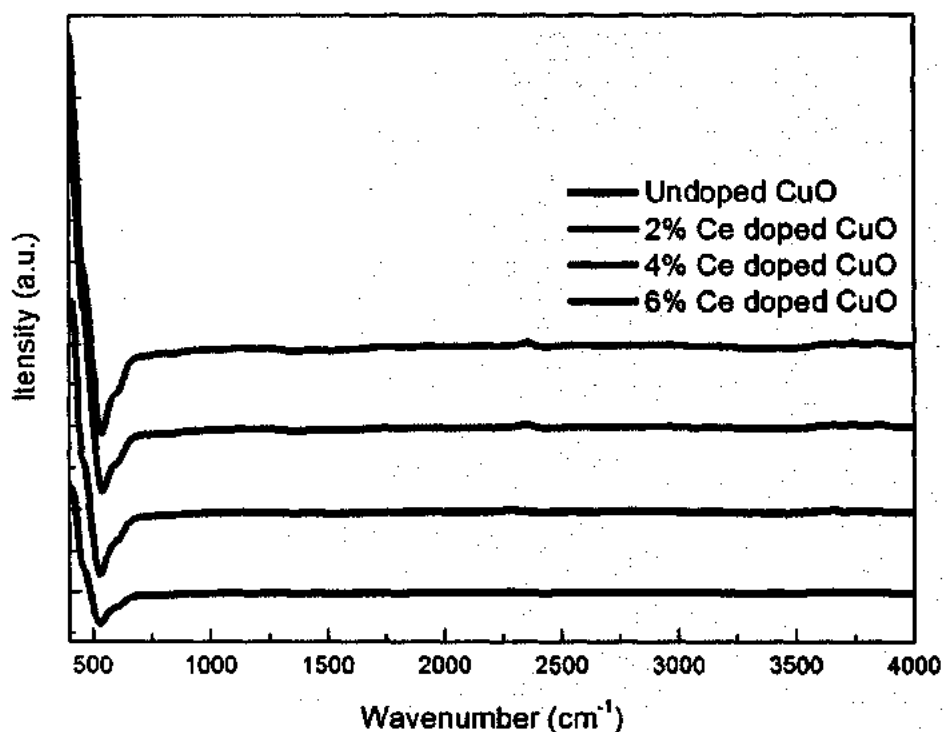
Figure 7.3 FTIR spectra of the prepared nanostructures

The study of phonons in nanomaterials is very important because the interaction between phonon and electron plays vital role in the optical characteristics of a material. Raman

91

spectroscopy is a strong tool to examine the vibrational, structural properties and defects chemistry of CuO nanostructures. CuO always crystallizes in monoclinic structure which is illustrated by C^6_{2h} (C^2/c) space group. CuO have 12 phonon vibrational modes at the zone centered described the following equation as follows:

$$\Gamma = 4A_u + 5B_u + A_g + 2B_g \qquad (7.1)$$

The three ($A_g + 2B_g$) modes are Raman active, while three acoustical modes are represented by ($A_u + 2B_u$) and the remaining 6 modes are infrared active. Figure 7.4 depicts the Raman spectra of undoped and Ce doped CuO nanostructures which contains Raman active modes at 278, 310 and 625 cm^{-1} which are assigned to one A_g and two B_g modes respectively. The peak positions of all the Raman active modes are blue shifted as compared to that of bulk CuO, which may be attributed to the particle size effects [171]. The peak at wave number of 508 cm^{-1} may be linked with multi-phonon scattering mode [172].
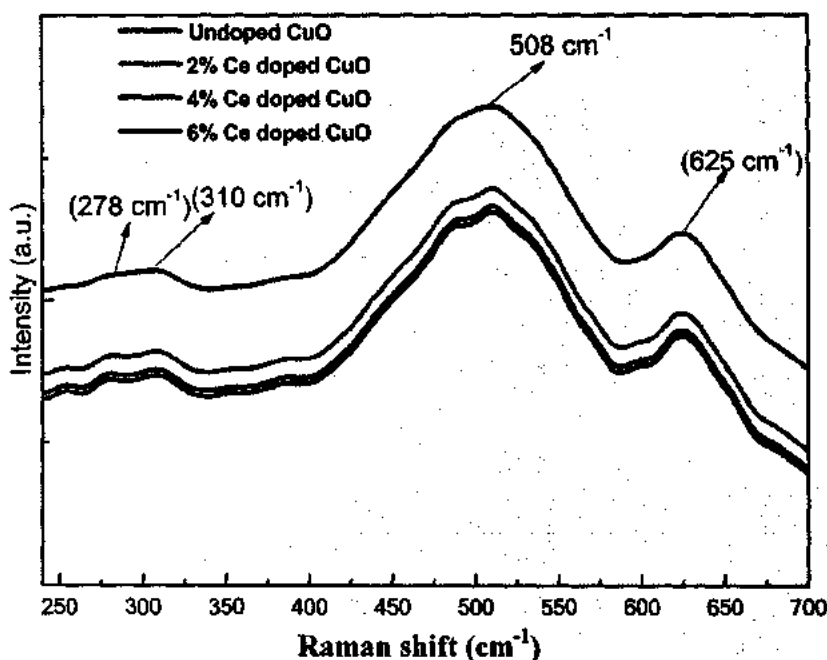
Figure 7.4 Raman spectra of the synthesized nanostructures

7.2.3 Optical study

The Ce doping induced effects on the optical properties of CuO nanostructures have been explored using UV-visible absorption spectroscopy. Absorption spectra of $Ce_xCu_{1-x}O$ nanostructures have been recorded in the wavelength range of 200-800 nm and shown in figure 7.5.
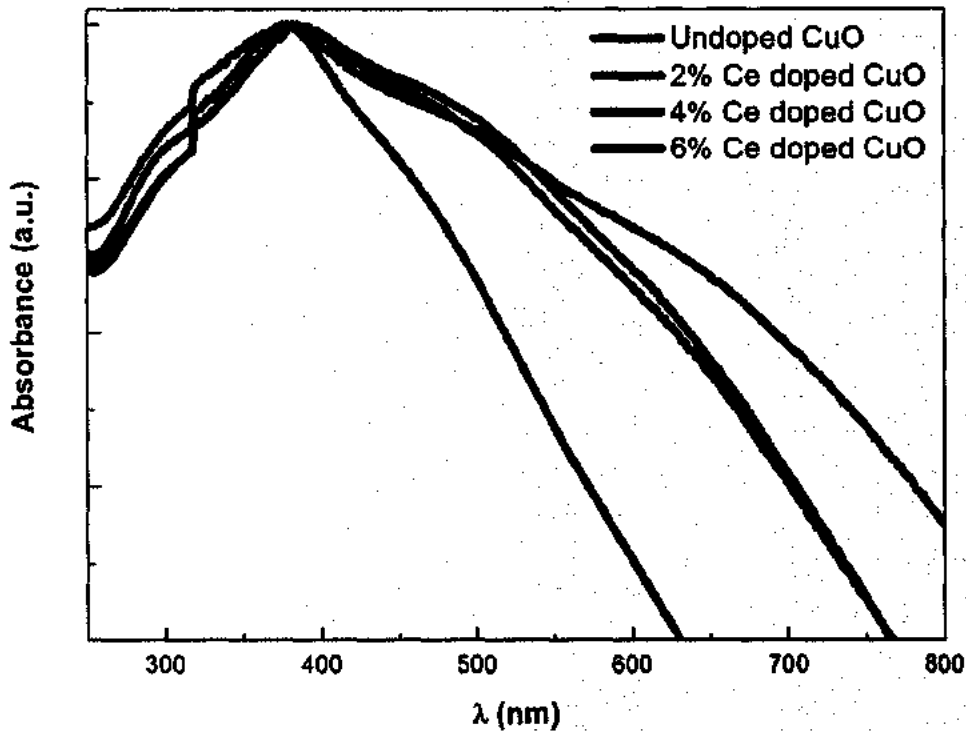
Figure 7.5 UV-vis absorption spectra of the synthesized nanostructures

The absorption spectra of undoped CuO nanostructures show broad absorption peak in the UV region at 380 nm. The CuO nanostructures doped with 2 and 4% Ce show a slight red shift in the absorption peak whereas 6% Ce doped sample exhibit no shift as compared to that of undoped CuO nanostructures. Moreover, it is observed that undoped CuO strongly absorbs the light in UV region and weakly in visible region. But all Ce doped CuO samples exhibit significant light absorption in the visible region. This remarkable absorption of light in the visible region and the red shift in absorption edge may be attributed to the following reasons: 1)

93

the Ce doping may reduce the band gap of CuO and electron from the valence band can be excited to conduction band by absorbing visible light, 2) interaction between the 4f electrons of Ce and conduction band electrons of CuO [173].

The optical band gap of undoped and Ce doped CuO nanostructures have been estimated using the following relation [174];

$$(\alpha h\upsilon)^n = B(h\upsilon - E_g)$$

In this relation α is the absorption coefficient, $h\upsilon$ is the photon energy, B is a constant, E_g represents band gap energy and n can either take up value 2 for direct band gap or 1/2 for indirect band gap. Here, n is taken 2 for calculation of the direct band gap energies of the prepared nanostructures. The band gap energies of undoped and Ce doped CuO nanostructures have calculated by plotting $(\alpha h\upsilon)^2$ versus $h\upsilon$ and extrapolating the linear part of the curves to the energy axis. The direct band gap energy of undoped CuO nanostructures is observed to be 2.48 eV, which is much higher as compared to band gap of 1.2 eV of bulk CuO [25]. This enlargement of CuO band gap may be assigned to quantum size effects as discussed in introduction section. Previously, band gap energy of 4.13 eV has been reported for quantum dots of CuO having average particle size of 10 nm [25]. The band gap energy of CuO nanostructures has been found to decrease down to 2.2 eV with Ce doping as shown in figure 7.6. This may be explained as follows: the Ce dopant may produce a distinct impurity band into the band gap of ZnO by its 4f5d electrons localized states, which may broaden due to the overlap of the wave functions of the adjacent dopants electrons [175-177]. This impurity band can merge with the bottom of the conduction band at sufficient dopant concentration level. The merging of impurity band with conduction band may cause the reduction of the band gap [178]. Such discussions are recently reported for Ce doped ZnO and GaN [178, 179]. Furthermore, the decrease in the band

94

gap may be associated with charge transfer between the conduction or valence band electrons of CuO with 4f5d electrons of Ce^{4+} ions. This charge transfer may create trapping levels in the Ce doped CuO nanostructures which can decrease the band gap of CuO [180].
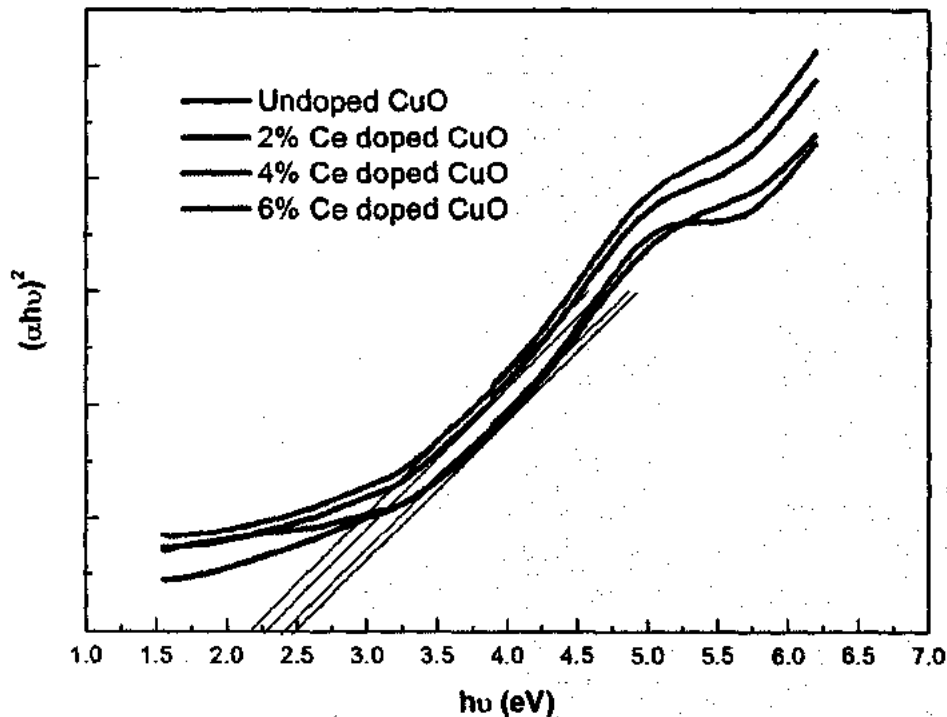
Figure 7.6 Direct band gap energy estimation of $Ce_xCu_{1-x}O$ nanostructures

7.2.4 Antibacterial study

Ce doping induced effects on the antibacterial activity of CuO nanostructures have been investigated. Figure 7.7 (a & b) represents the growth curves of *E. coli* and *S. aureus* in the presence of colloidal suspensions of $Ce_xCu_{1-x}O$ nanostructures. Undoped CuO nanostructures have delayed the growth of *E. coli* for 4 hours and decreased it afterwards. The growth inhibition capability of CuO nanostructures against *E. coli* is observed to increase significantly with the increase in Ce doping level. 6% Ce doped CuO nanostructures inhibit almost 90% growth of *E. coli* as shown in figure 7.7 (a). The prepared undoped and Ce doped CuO nanostructures are

found to be more effective against *S. aureus* than *E. coli*. 65% growth of *S. aureus* is inhibited by application of undoped CuO nanostructures and is observed to increase significantly with Ce doping. It is found that the multi-drug resistant *S. aureus* bacterium can be completely eradicated by the application of 6% Ce doped CuO nanostructures as shown in figure 7.7 (b).
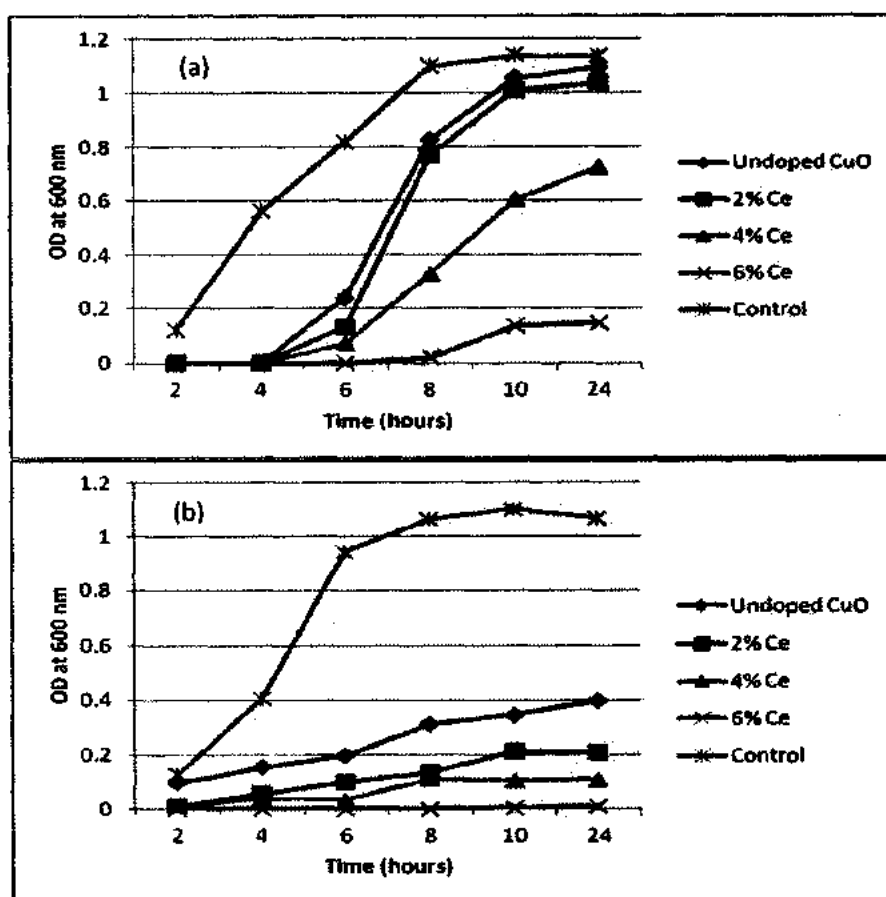
Figure 7.7 Growth Curves for (a) *E. coli* (b) *S. aureus* bacterial strain in the presence of $Ce_xCu_{1-x}O$ nanostructures

Several mechanisms of action have been proposed for the inhibition of bacteria by metal oxides nanostructures such as; direct electrostatic interaction between nanostructures and bacteria cell wall, photoactivation of metal oxides and the generation of reactive oxygen species (H_2O_2, hydroxyl radicals and singlet oxygen) or release of metal ions in the suspension [81, 86]. Here, a question arises that why the antibacterial of CuO nanostructures is increased with the

increase in Ce dopant concentration. This enhancement may be attributed two reasons. 1) The Ce doping may enhance the ROS generation capability of CuO nanostructures. CuO nanostructures can be activated by white light to generate electron-hole pair. Upon reaction with water molecules, these holes can generate ROS via mechanism as earlier for ZnO. But the problem is recombination of electron-hole pair, which can reduce the ROS generation. In case of Ce doped CuO samples, the probability of electron-hole pair recombination may be reduced due to the trapping of electrons by Ce ions via following process [180]:

$$Ce^{4+} + e^- \rightarrow Ce^{3+}$$

$$Ce^{3+} + O_2 \rightarrow O_2^{\bullet} + Ce^{4+}$$
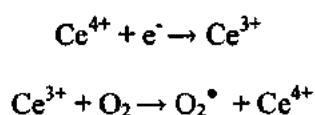
Hence, the enhancement in the antibacterial activity of CuO nanostructures with Ce doping may be credited to the electrons trapped in the Ce sites. The trapping of electrons will lead to more ROS generation, resulting in higher antibacterial activity of Ce doped CuO nanostructures. 2) The antibacterial activity of CuO nanostructures is also associated with the release of Cu^{2+} ions in the solution [92]. With the substitution of Ce^{4+} ions for Cu^{2+} ions in the host matrix, there is a possibility that some Cu^{2+} ions will accommodate on the interstitial sites. And it is logical to expect release of more Cu^{2+} ions in the solution because ions can easily be released from interstitial sites comparing from native sites. Furthermore, Ce^{4+} ions may also be released in the solution in case of Ce doped CuO nanostructures. Thus, Ce doping will enhance the release of Ce^{4+} and Cu^{2+} ions leading to higher antibacterial activity of Ce doped CuO nanostructures.

7.2.5 Cytotoxicity

Nanomaterials can be used as potential antibacterial agents only if they exhibit toxicity towards bacteria but not towards healthy human cells. Thus, understanding about the cytotoxicity of the nanomaterials is essential before their application in biomedical sector. Therefore, the

cytotoxicity of the prepared nanostructures has been investigated on human cell line *SH-SY5Y* cells. *SH-SY5Y* cells have been treated with synthesized $Ce_xCu_{1-x}O$ nanostructures for 24h and number viable cells were recorded under optical microscope. The prepared nanostructures have no significant effect on the viability of healthy cell line as shown in figure 7.8. To support these results, phase contrast microscopy has been used to evaluate the effects of synthesized nanostructures on the morphology of the *SH-SY5Y* cells. It can be seen from figure 7.9 that both undoped and Ce doped CuO nanostructures have altered the cell morphology to some extent. But no significant effects have been observed on cell count. Hence, the prepared nanostructures may be considered biosafe and biocompatible towards the tested cell line. These findings suggest that the Ce doping has significantly enhanced the antibacterial activity of CuO nanostructures both against Gram-negative *E. coli* and Gram-positive *S. aureus* bacteria but have a non toxic nature towards *SH-SY5Y* cells.
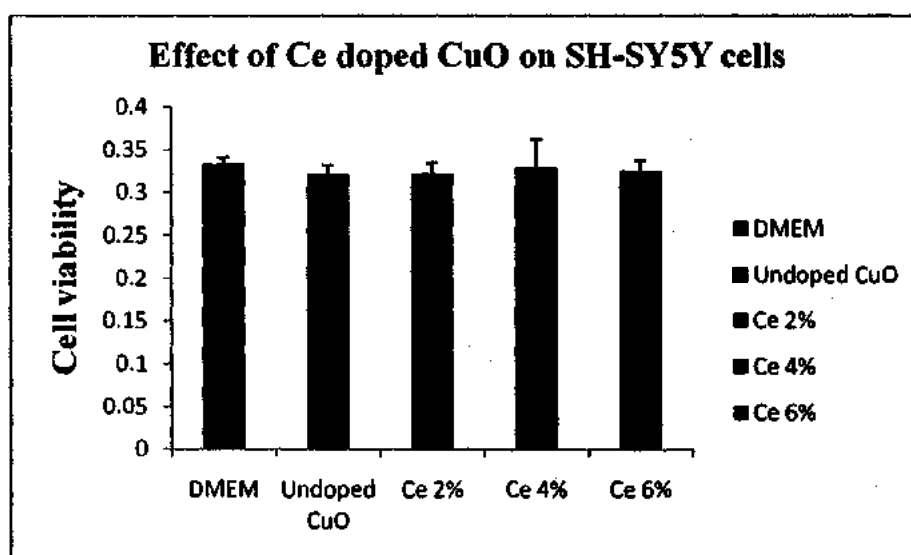

Figure 7.8 Effect of $Ce_xCu_{1-x}O$ nanostructures on *SH-SY5Y* Cells
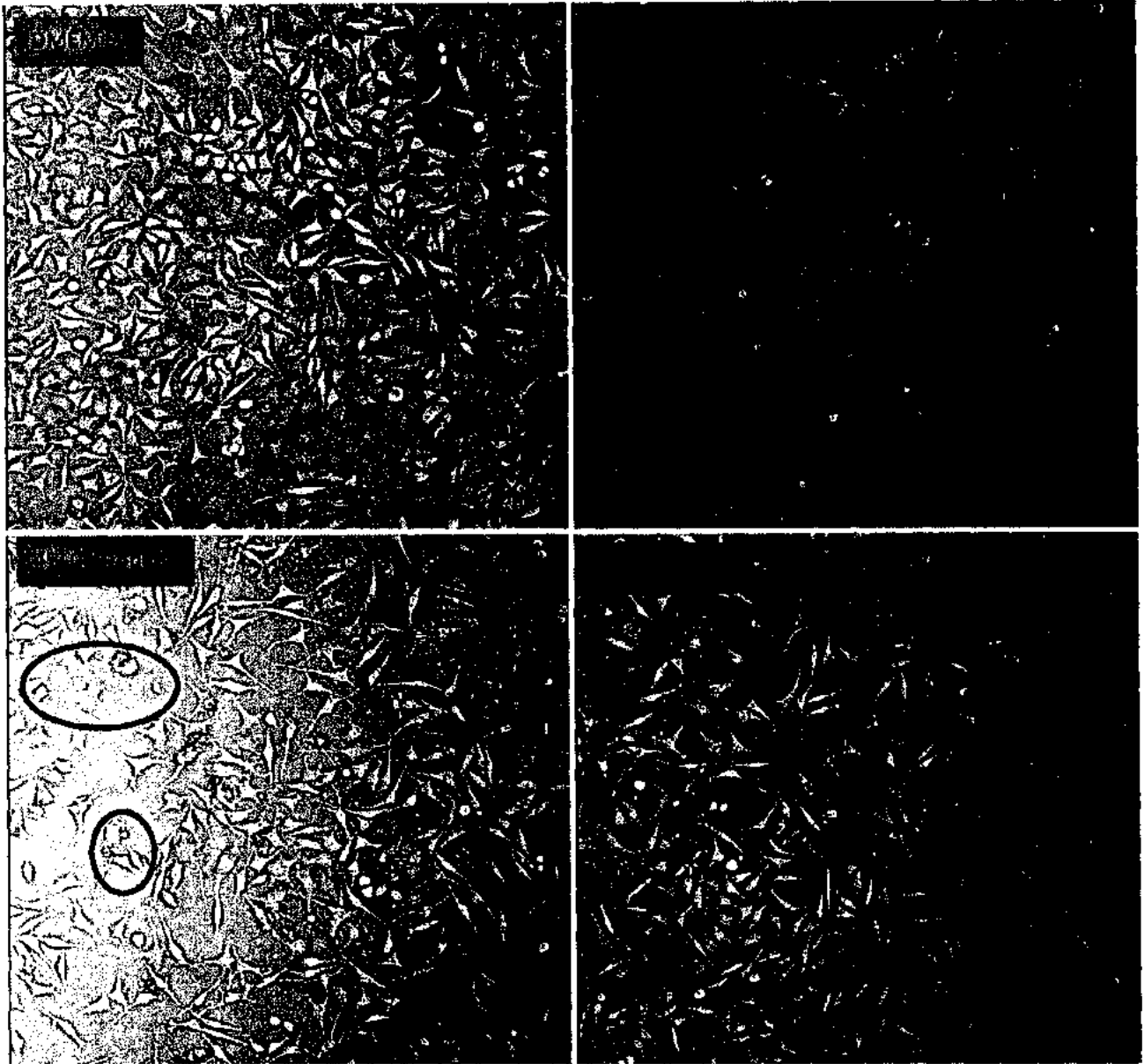
Figure 7.9 Phase contrast microscopy images of the SH-SY5Y cells after treatment with the prepared nanostructures (circles show morphological variation)

Conclusions

The core objectives of this thesis were to fabricate and characterize different MOs nanostructures and to choose best MO in terms of its physical properties and bioactivity. Furthermore, tuning of the physical properties especially, defects chemistry and optical properties for improving its biological performance. To achieve these objectives, four different MOs nanostructures such as ZnO, CuO, SnO$_2$ and CeO$_2$ have been synthesized by a simple, cost effective, versatile and easily reproducible soft chemical method under the same conditions with controlled particle sizes and shapes. The synthesized MOs nanostructures have been characterized for various physical properties such as structural, morphological, vibrational and optical properties. Furthermore, their antibacterial activity has examined against different multi-drug resistant bacteria. It has been observed that ZnO nanostructures have the highest antibacterial potency among all MOs nanostructures.

Keeping in view the physical properties and antibacterial activity, ZnO nanostructures have been selected and tuned their various physical properties via selective chemical doping. As chemical doping is one of the most effective and easy way for this purpose. ZnO nanostructures have been doped with different metals such as Sn, Ag and Ni. The detailed structural investigations have been done and it is observed that all dopants have been successfully doped into ZnO host matrix without creating any secondary phases. The dopants have varied the structural characteristics of ZnO such as crystallite size, lattice parameters and crystalline quality of ZnO but hexagonal wurtzite structure of host ZnO is maintained for all doped nanostructures. The morphological analyses of the undoped and doped nanostructures have been carried out via SEM. It has been observed that Sn doping transforms the particle shape of ZnO from spherical to rods. Furthermore, Ag and Ni dopants have also varied the morphology of ZnO and also varied

the particle size. The morphological transformation and variation in particle sizes have been attributed to various factors such as difference in their Pauling electronegativities and dipolar interactions between host ions and dopant ions due to polar crystal nature of ZnO along c-axis. It is concluded from FTIR results that in case of spherical nanoparticles, ZnO gives one peak in IR region while two peaks for nanorods. These are very interesting findings as morphological transformations can be judged with help of IR spectroscopy. The vibrational properties of undoped and all doped ZnO nanostructures have been studied with Raman spectroscopy. Raman spectroscopy results also supported the successful incorporation of dopants in ZnO matrix and corroborated well with XRD and FTIR results. It has further indicated the formation of crystal defects in ZnO host matrix with metal doping. The Ag dopant among all the dopants has been found to create the largest amount of defects such as Zn interstitial and oxygen vacancies. It has been concluded from the study of the optical investigations that the doping of ZnO nanostructures is very effective for tuning their optical bandgap edge. The Sn and Ag dopants have increased the bandgap energy of ZnO nanostructures while Ni doping resulted in decreased band gap energy. This tuning of bandgap energies have been attributed to the quantum confinement effects and sp-d exchange interactions. The tunable bandgap energies and defects concentration make these nanostructures potential for various applications such as UV absorbents, sunscreens, light emitting diodes, solar cells, photo-catalytic degradation of pollutants, field effect transistors, targeted drug delivery, anticancer agents and antibacterial activity.

It has been concluded from antibacterial studies that all the dopants have increased the antibacterial activity of ZnO nanostructures remarkably. This remarkable increase in the antibacterial activity can be associated with the particle size and shape, tunable optical and

defects characteristics of doped ZnO nanostructures. It has been observed that particle size and rod-like morphology are more effective as compared to other shapes of nanostructures. Furthermore, ROS generation and soluble metal ions also play a major role in the antibacterial activity of ZnO nanostructures. If ZnO nanostructures have more defects then it inhibits the photo-generated electron-hole pair which leads to higher amount of ROS generation as a result there is higher antibacterial activity. This is why Ag doped ZnO nanorods have been observed to have highest antibacterial activity among all synthesized nanostructures. Finally, from cytotoxicity results it have been concluded that both undoped and metal doped ZnO nanostructures are biosafe and biocompatible which makes them potential for various biomedical applications such as targeted delivery, antibacterial coating of hospital implants, wound dressing materials and UV sunscreen creams and lotions.

Finally, in ordered to have better antibacterial activity against Gram-negative bacteria (ZnO has showed less activity against Gram-negative as compare with Gram-positive bacteria), $Ce_xCu_{1-x}O$ nanostructures have been prepared via same procedure as adopted for ZnO based nanostructures. As CuO has wide absorption band in range of UV to visible so it was expected to have better photo-degradation of Gram-negative bacteria as compared to other MOs. The structural investigations have shown the formation of a single phase monoclinic structure of CuO for all samples. The SEM images have revealed the formation of rod-like CuO nanostructures with an average diameter of 30 nm. The FTIR spectra of undoped and Ce doped CuO nanostructures have shown a single characteristic strong peak associated with the Cu–O stretching vibrations of monoclinic CuO. The bandgap energy of CuO nanostructures has been found to significantly decrease with Ce doping. The Ce doped CuO nanostructures have been observed to be more effective than the undoped CuO nanostructures both against Gram-negative

and Gram-positive bacteria. Interestingly, it has been found that *S. aureus* and *Pseudomonas aeruginosa* bacteria can be completely eradicated by application of Ce doped CuO nanostructures. Cytotoxicity results have demonstrated that all the prepared nanostructures of CuO are also biosafe and biocompatible to healthy cells.

References

[1] C. Noguera, Physics and Chemistry at Oxide Surfaces; Cambridge University Press: Cambridge, UK, (1996).

[2] H.H. Kung, Transition Metal Oxides: Surface Chemistry and Catalysis; Elsevier: Amsterdam, (1989).

[3] V.E. Henrich, P.A. Cox, The Surface Chemistry of Metal Oxides; Cambridge University Press: Cambridge, UK, (1994).

[4] A.F. Wells, Structural Inorganic Chemistry, 6th edition; Oxford University Press: New York, (1987).

[5] W.A. Harrison, Electronic Structure and the Properties of Solids; Dover: New York, (1989).

[6] R.W.G. Wyckoff, Crystal Structures, 2nd ed.; Wiley: New York, (1964).

[7] M. Valden, X. Lai, D.W. Goodman, Science, 281, (1998) 1647.

[8] J.A. Rodriguez, G. Liu, T. Jirsak, Z. Chang, J. Dvorak, A. Maiti, J. Am. Chem. Soc., 124, (2002) 5247.

[9] M. Baumer, H. Freund, J. Prog. Surf. Sci., 61, (1999) 127.

[10] M.L. Trudeau, J.Y. Ying, Nanostructured Mater., 7, (1996) 245.

[11] V. Palkar, P. Ayyub, S. Chattopadhyay, M. Multani, Phys Rev B., 53, (1996) 2167.

[12] M. Ghosh, D. Karmakar, S. Basu, S.N. Jha, D. Bhattacharyya, S.C. Gadkari, S.K. Gupta, Journal of Physics and Chemistry of Solids., 75, (2014) 543.

[13] R.K. Hailstone, A.G. DiFrancesco, J.G. Leong, T.D. Allston, K.J. Reed, J. Phys. Chem. C., 113, (2009) 15155.

[14] G. Ramakrishna and H.N. Ghosh, Langmuir., 19, (2003) 3006.

[15] J.E. Spanier, R.D. Robinson, F. Zhang, S.W. Chan, I.P. Herman, Phys Rev B., 64, (2001) 245407.

[16] A.I. Ekimov, A.A. Onushchenko, Sov phys Semicon., 16, (1982) 775.

[17] J.E. Brus JE, J Lumin., 31, (1984) 381.

[18] Y. Kayanuma, Phys Rev B., 38, (1988) 9797.

[19] M. Iwamoto, T. Abe, Y. Tachibana, J. Mol. Catal. A., 55, (2000) 143.

[20] O. Vigil, F. Cruz, A. Morales-Acabedo, G. Contreras-Puente, L. Vaillant, G. Santana, Mat. Chem. Phys., 68, (2001) 249.

[21] T. Suzuki, I. Kosacki, V. Petrovsky, H.U. Anderson, J. Appl. Phys., 91, (2001) 2308.

[22] R. Viswanaha, S. Sapra, B. Satyani, B.N. Der, D.D. Sarma, J. Mat. Sci., 14, (2004) 661.

[23] H. Deng, J.M. Hossenlopp, J. Phys. Chem. B., 109, (2005) 66.

[24] O.I. Micic, J. Sprague, Z. Lu, A.J. Nozik, Appl Phys Lett., 68, (1996) 3150.

[25] K. Borgohain, J.B. Singh, M.V. Rama Rao, T. Shripathi, S. Mahamuni, Phys Rev B., 61, (2000) 11093.

[26] P. Patsalas, S. Logothetidis, and C. Metaxa, Appl. Phys. Lett., 81, (2002) 466.

[27] S.D. Park, J.M. Vohs, and R.J. Gorte, Nature, 404, (2000) 265.

[28] X.D. Feng, D.C. Sayle, Z.L. Wang, M.S. Paras, B. Santora, A.C. Sutorik, T.X.T. Sayle, Y. Yang, Y. Ding, X.D. Wang, and Y.S. Her, Science, 312, (2006) 1504.

[29] T. Masui, K. Fujiwara, K. Machida, G. Adachi, T. Sakata, and H. Mori, Chem. Mater., 9, (1997) 2197.

[30] T.S. Stefanik and H.L. Tuller, J. Eur. Ceram. Soc., 21, (2001) 1967.

[31] N. Imanaka, T. Masui, H. Hirai, and G. Adachi, Chem. Mater., 15, (2003) 2289.

[32] A.H. Morshed, M.E. Moussa, S.M. Bedair, R. Leonard, S.X. Liu, and N. El-Masry, Appl. Phys. Lett., 70, (1997) 1647.

[33] X.J. Yu, P.B. Xie, and Q.D. Su, Phys. Chem. Chem. Phys., 3, (2001) 5266.

[34] V.K. Ivanov, O.S. Polezhaeva, G.P. Kopitsa, A.E. Baranchikov, and Y.D. Tretyakov, Inorg. Mater., 44, (2008) 272.

[35] R.J. Cava, Science, 257, (1990) 656.

[36] J.M. Tranquada, B.J. Sternlieb, J.D. Axe, Y. Nakamura, S. Uchida, Nature, 375, (1995) 561.

[37] K. Kwak, C. Kim. Korea–Australia Rheol J., 17, (2005) 35.

[38] J.F. Xu, W. Ji, Z.X. Shen, S.H. Tang, X.R. Ye, D.Z. Jia, J Solid State Chem., 147, (1999) 516.

[39] A. Rahnama, M. Gharagozlou, Opt Quant Electron, 44, (2012) 313.

[40] J.F. Wagner, Science, 300, (2003) 1245.

[41] R.E. Presley, C.L. Munsee, C.-H. Park, D. Hong, J.F. Wager, D.A. Keszler, J. Phys. D., 37, (2004) 2810.

[42] M. Sawada, M. Higuchi, S. Kondo, Jpn. J. Phys., 40, (2001) 3332.

[43] C. Xu, J. Tamaki, N. Miura, Sensors and Actuators B, 147, (1991) 3.

[44] A.L. Dawar, J.C. Joshi, J. Mater. Sci., 19, (1984) 1.

[45] L.M. Cukrov, T. Tsuzuki, P.G. McCormick, Scr. Mater., 44, (2001) 1787.

[46] F. Lu, Y. Liu, M. Dong, X. Wang, Sensors and Actuators B, 66, (2000) 225.

[47] C. Karunakaran, S. Sakthi Raadha, P. Gomathisankar, Journal of Alloys and Compounds, 549, (2013) 269.

[48] R. Adnan, N.A. Razana, I.A. Rahman and M.A. Farrukh, Journal of the Chinese Chemical Society, 57, (2010) 222.

[49] Y.L. Wu, A.I.Y. Tok, F.Y.C. Boey, X.T. Zeng, X.H. Zhang, Appl Surf Sci., 253, (2007) 5473.

[50] R. Yousefi, B. Kamaluddin, Appl Surf Sci., 255, (2009) 9376.

[51] M.S. Akhtar, M.A. Khan, M.S. Jeon, O.B. Yang, Electrochim Acta., 53, (2008) 7869.

[52] A.J. Morfa, N. Kirkwood, M. Karg, T.B. Singh, P. Mulvaney, J Phys. Chem. C, 115, (2011) 8312.

[53] M.J. Akhtar, M. Ahamed, S. Kumar, M.M. Khan, J. Ahmad, S.A. Alrokayan, Int. J. Nanomedicine, 7, (2012) 845.

[54] N. Jones, B. Ray, K.T. Ranjit, A.C. Manna, FEMS Microbiol Lett., 279, (2008) 71.

[55] C. Klingshirn, phys. stat. sol. B, 244, (2007) 3027.

[56] C. Jagadish, S.J. Pearton, Zinc Oxide Bulk, Thin Films and Nanostructures, Elseviser Ltd., (2006).

[57] O. Nennewitz, H. Schmidt, J. Pezoldt, T.H. Stauden, J. Schawohl, L. Spiess, Physica Status Solidi (a)., 145, (1994) 283.

[58] R. Viswanatha, S. Sapra, B. Satpati, P.V. Satyam, B.N. Dev, D.D. Sarma, J. Mater. Chem., 14, (2004) 661.

[59] W. Ming-wei, B.K. Woo, T. Zhen, H. Jia-guang, C. Wei, Z. Wei-li, Optoelectronics Letters., 6, (2009) 0431.

[60] K.L. Foo, U. Hashim, K. Muhammad, C.H. Voon, Nanoscale Research Letters., 9, (2014) 429.

[61] W. Il Park, J.S. Kim, G.H. Yi, M.H. Bae, H.J. Lee, Appl. Phys. Lett., 85, (2004) 5052.

[62] H. Morkoç and U. Ozgur, Zinc Oxide: Fundamentals, Materials and Device Technology, WILEY-VCH Verlag GmbH & Co. KGaA, Weinheim., (2009).

[63] D.C. Look, Mater. Sci. Eng., 80, (2001) 383.

[64] T. Olorunyolemi, A. Birnoim, Y. Carmel, O. Wilson, I. Lioyd, S. Smith, and R. Campbell, J. Am. Cera. Socie., 85, (2002) 1249.

[65] T.C. Damen, S.P.S. Porto and B. Tell, Physical Review, 142, (1966) 570.

[66] C.A. Arguello, D.L. Rousseau and S.P.S. Porto, Physical Review, 181, (1969) 1351.

[67] R.H. Callender, S.S. Sussman, M. Selders and R.K. Chang, Physical Review B: Condensed Matter, 7, (1973) 3788.

[68] J.M. Calleja and M. Cardona, Physical Review B: Condensed Matter, 16, (1977) 3753.

[69] M.A. Stroscio and M. Dutta, Phonons in Nanostructures, Cambridge University Press, (2001).

[70] N. Ashkenov, B.N. Mbenkum, C. Bundesmann, V. Riede, M. Lorenz, D. Spemann, E.M. Kaidashev, A. Kasic, M. Schubert, M. Grundmann, G. Wagner, H. Neumann, V. Darakchieva, H. Arwin and B. Monemar, Journal of Applied Physics, 93, (2003) 126.

[71] K.C. Barick, M. Aslam, J. Wu, V.P. Dravid, D. Bahadur, J. Mater. Res., 24, (2009) 3543.

[72] X. Wang, J. Xu, B. Zhang, H. Yu, J. Wang, X. Zhang, J. Yu, Q. Li, Adv. Mater., 18, (2006) 2476.

[73] B.E. Sernelius, K.F. Berggren, Z.C. Jin, I. Hamberg, C.G. Granqvist, Phys Rev B., 37, (1988) 10244.

[74] D.A. Lucca, D.W. Hamby, M.J. Klopfstein, G. Cantwell, Phys. Stat. Solidi. B, 229, (2002) 845.

[75] O. Yamamoto, Int. J. Inorg. Mater., 3, (2001) 643.

[76] Q.L. Li, S. Mahendra, D.Y. Lyon, L. Brunet, M.V. Liga, D. Li, P.J.J. Alvarez, Water Res., 42, (2008) 4591.

[77] W. Witte, Infect. Genet. Evol., 4, (2004) 187.

[78] F. Vandenesch, T. Naimi, M.C. Enright, Emerg Infect Dis., 9, (2003) 978.

[79] L. Hall-Stoodley, J.W. Costerton, P. Stoodley. Nat. Rev. Microbiol., 2, (2004) 95.

[80] D.R. Monteiro, L.F. Gorup, A.S. Takamiya, A.C. Ruvollo-Filho, E.R.D. Camargo and D.B. Barbosa, Int. J. Antimicrob. Agents, 34, (2009) 103

[81] V.B. Schwartz, T. Franck, R. Sandra, P. Sabine, C. Lars, L. Alexandros, F. Renate, L. Katharina and J. Ulrich, Adv. Funct. Mater., 22, (2012) 2376.

[82] F. Sayılkana, M. Asilturka, N. Kirazb, E. Burunkayab, E. Arpac and H. Saylkan, J. Hazardous Mater., 162, (2009) 1309.

[83] O. Akhavan and E. Ghaderi, Surf. Coat. Technol., 205, (2010) 219.

[84] X. Bingshe, N. Meia, W. Liqiao, H. Wensheng and L. Xuguang, J. Photochem. Photobiol. A, 188, (2007) 98.

[85] C. Karunakarann, R.S. Sakthi and P. Gomathisankar, Mater. Sci. Semicond. Process., 16, (2013) 818.

[86] J. Sawai and T. Yoshikawa, J. Appl. Microbiol., 96, (2004) 803.

[87] E. Malka, I. Perelshtein, A. Lipovsky, Y. Shalom, L. Naparstek, N. Perkas, T. Patick, R. Lubart, Y. Nitzan, E. Banin, A. Gedanken, Small, 9, (2013) 4069.

[88] M. Schiek, K. Al-Shamery, M. Kunat, F. Traeger, Ch. Wöll, Phys. Chem. Chem. Phys., 8, (2006) 1505.

[89] M.J. Hajipour, K.M. Fromm, A.A Ashkarran, D.J de Aberasturi, I.R de Larramendi, T. Rojo, V. Serpooshan, W.J. Parak and M. Mahmoudi, Trends in Biotechnology, 30, (2012) 499.

[90] G. Gao, Nanostructures and nanomaterials: Synthesis, properties and applications, Imperial College Press, (2004).

[91] C. Karunakaran, V. Rajeswari, P. Gomathisankar, Mater. Sci. Semicond. Process., 14, (2011) 133.

[92] T. Adschiri, Y. Hakuta, K. Sue, K. Arai, J. Nanopart. Res., 3, (2001) 227.

[93] A. Azam, A.S. Ahmed, M. Oves, M.S. Khan, S.S. Habib, A. Memic, Int. J. Nanomed., 7, (2012) 6003.

[94] G.L. Yang, H.H. Ko, Y.W. Hsue, K.H. Yang, M.C. Wang, J. Han, X.J. Zhao, Ceram. Int., 39, (2013) 6805.

[95] Y. Tong, Y. Liu, L. Dong, et al, J. Phys. Chem. B., 110, (2006) 20263.

[96] J.F. Zang, C.M. Li, X.Q. Cui, J.X. Wang, X.W. Sun, H. Dong, C.Q. Sun, Electroanal., 19, (2007) 1008.

[97] R.A. Laudise, A.A. Ballman, J. Phys. Chem., 64, (1960) 688.

[98] S. Yamabi, H. Imai, J. Mater. Chem., 12, (2002) 3773.

[99] A. Kawska, P. Duchstein, O. Hochrein, D. Zahn, Nano Lett., 8, (2008) 2336.

[100] B.D. Cullity, Addison Wesley London, (1959).

[101] J.Z. Zhang, Optical Properties and Spectroscopy of Nanomaterials, World Scientific Publishing Co. Pvt. Ltd., (2009).

[102] R.K. Mishra, P.P. Sahay, Synthesis, Ceram. Int., 38, (2012) 2295.

[103]P. Virendra, D. Charlnene, Y. Deepti, A.J. Shaikh, V. Nadanathangam, Spectrochimica Acta Part A, 65, (2006) 173.

[104]D. Dasa, B.C. Nathb, P. Phukonc, S.K. Dolui, Colloids and Surfaces B: Biointerfaces, 101, (2013) 430.

[105]N. Talebiann, F. Jafarinezhad, Ceram. Int., 39, (2013) 8311.

[106]H.H. Koa, G. Yang, H.Z. Chengd, M.C. Wanga, X.J. Zhao, Ceram. Int., (2013) In press.

[107]A.A. Ashkarran, M. Ghavami, H. Aghaverdi, P. Stroeve, M. Mahmoudi, Chem. Res. Toxicol., 25, (2012) 1231.

[108]G. Subbiahdoss, S. Sharifi, D.W. Grijpma, S. Laurent, H.C. van der Mei, M. Mahmoudi, H.J. Busscher, Acta Biomaterialia, 8, (2012) 2047.

[109]B.S. Veronique, T. Franck, R. Sandra, P. Sabine, C. Lars, L. Alexandros, F. Renate, L. Katharina, and J. Ulrich, Adv. Funct. Mater., 22, (2012) 2376.

[110]K.H. Tam, A.B. Djurisic, C.M.N. Chan, Y.Y. Xi, C.W. Tse, Y.H. Leung, W.K. Chan, F.C.C. Leung, D.W.T. Au, Thin Solid Films, 16, (2008) 6167.

[111]R.R. Krishna, T.K. Ranjit and C.M. Adhar, Langmuir, 27, (2011) 4020.

[112]Y.W. Baek, and Y. Jan, Sci. Total Environ., 409, (2011) 1603.

[113]J.M. Anthony, K. Nicholas, K. Matthias, T.B. Singh and M. Paul, J. Phys. Chem. C, 115, (2011) 8312.

[114]J.A. Mohd, A. Maqusood, K. Sudhir, K. Majeed, A. Javed and A.A. Salman, Int. J Nanomed., 7, (2012) 845.

[115]N. Salah, S.S. Habib, Z.H. Khan, Int. J Nanomed., 6, (2011) 863.

[116] M. Jung, S. Kim, S. Ju, Optical Materials, 33, (2011) 280.

[117] S. Ameena, S. Akhtarb, H.K. Seoc, Y.S. Kima, H.S. Shin, Chemical Engineering Journal, 187, (2012) 351.

[118] A. Mariam, T.M. Begam, M. Jayachandran, P. Kumar and M. Bououdina. International Journal of Bioassays, 2, 2013 304.

[119] L.L. Zhang, Y.H. Jiang, Y.L. Ding, J Nanoparticle Res., 93, (2007) 479.

[120] F. Sayılkana, M. Asilturka, N. Kirazb, E. Burunkayab, E. Arpac, H. Sayılkan, Journal of Hazardous Materials, 162, (2009) 1309.

[121] Y.S. Jang, E.Y. Lee, Y.H. Park, S.H. Jeong, S.G. Lee, Y.R. Kim, M.K. Kim, S.W. Son, Mol Cell Toxicol., 8, (2012) 171.

[122] Z. Peng, G. Dai, W. Zhou, P. Chen, Q. Wan, Q. Zhang, B. Zou. Applied Surface Science, 256, (2010) 6814.

[123] R. Kripala, K. Guptaa, K. Srivastavab, S.K. Mishra, Spectrochimica Acta Part A, 79, (2011) 1605.

[124] L. Luo, K.H. Fliger, D. Xie, M. Niederberger, J Sol-Gel Sci Technol., 65, (2013) 28.

[125] S. Xu, Z.L. Wang, Nano Res., 4, (2011) 1013.

[126] Z.L. Wang, J. Phys.: Condens. Matter., 16, (2004) 829.

[127] L. Wu, Y. Wu, X. Pan and F. Kong, Optical Materials, 28, (2006) 418.

[128] S. Gunalana, R. Sivaraja, V. Rajendran, Progress in Natural Science: Materials International, 22, (2012) 695.

[129] Veronique B. Schwartz , Franck Thetiot , Sandra Ritz , Sabine Putz , Lars Choritz , Alexandros Lappas , Renate Forch , Katharina Landfester , and Ulrich Jonas. Adv. Funct. Mater. 2012;22:2376–2386.

[130] B.A. Lipsky, V.P. Tabak, R.S. Johannes, L. Vo, L. Hyde, J.A. Weigelt, Diabetologia, 53, (2010) 914.

[131] T. Xia, M. Kovochich, M. Liong, L. Madler, B. Gilbert, H. Shi, J.I. Yeh, J.I. Zink and A.E. Neel, ACS Nano, 10, (2008) 2121.

[132] P. Yang, H. Yan, S. Mao, R. Russo, J. Johnson, R. Saykally, N. Morris, J. Pham, R. He, H. Chao, Adv. Funct. Mater., 12, (2002) 323.

[133] Y. Cui, Q.Q. Wei, H.K. Park, C.M. Lieber, Science, 293, (2001) 1289.

[134] S. Saito, M. Miyayama, K. Koumot, and H. Yanagida, J. Am. Ceram. Soc., 68, (1985) 40.

[135] Y. B. Li, Y. Bando, and D. Golberg, Appl. Phys. Lett., 84, (2004) 3603.

[136] S. Choopun, A. Tubtimtae, T. Santhaveesuk, S. Nilphai, E. Wongrat, and N. Hongsith, Appl. Surf. Sci., 256, (2009) 998.

[137] R. Wang, J.H. Xin, Y. Yang, H. Liu, L. Xu, and J. Hu, Appl. Surf. Sci., 227, (2004) 312.

[138] Q.H. Li, Y.X. Liang, Q. Wan, and T.H. Wang, Appl. Phys. Lett., 85, (2004) 6389.

[139] A. Ozlem, E.H. Husnu, D. Caner, J. Am. Ceram. Soc., 96, (2013) 766.

[140] Y. Jin, Q. Cui, K. Wang, J. Hao, Q. Wang, and J. Zhang, J. Appl. Phys., 109, (2011) 053521.

[141] M.J. Height, S.E. Pratsinis, O. Mekasuwandumrong, P. Praserthdam, Appl. Catal. B, 63, (2006) 305.

[142] M. Scepanovi, M. Grujic-Brojcin, K. Vojisavljevic, S. Bernik, T. Sreckovic, J. Raman Spectrosc., 41, (2010) 914.

[143] B.S. Reddy, S.V. Reddy, N.K. Reddy, Y.P. Reddy, Adv. Mat. Lett., 5, (2014) 199.

[144] R. Wahab, S.G. Ansari, Y.S. Kim, H.K. Seo, G.S. Kim, G. Khang, and H.S. Shin, Mater. Res. Bull., 42, (2007) 1640.

[145] S.H. Jeong, B.N. Park, S.B. Lee, J.H. Boo, Surf. Coat. Technol., 201, (2007) 5318.

[146] A.H. Shah, E. Manikandan, M.B. Ahmed, V. Ganesan, J Nanomed Nanotechol., 4, (2013) 168.

[147] I. Matai, A. Sachdev, P. Dubey, S.U. Kumar, B. Bhushan, P. Gopinath, Colloids and Surfaces B: Biointerfaces, 115, (2014) 359.

[148] Y.J. Xing, Z.H. Xi, Z.Q. Xue, X.D. Zhang, J.H. Song, R.M. Wang, J. Xu, Y. Song, S. L. Zhang, D.P. Yu, Appl Phys Lett., 83, (2003) 1689.

[149] A.H. Shah, E. Manikandan, M.B. Ahmed, D.A. Mir, S.A. Mir, Journal of Luminescence, 145, (2014) 944.

[150] N. Talebian, S.M. Amininezhad, M. Doudi, Journal of Photochemistry and Photobiology B: Biology, 120, (2013) 66.

[151] J. Iqbal, T. Jan, R. Yu, J Mater Sci: Mater Electron, 24, (2013) 4393.

[152] J. Iqbal, T. Jan, M. Shafiq, A. Arshad, N. Ahmad, S. Badshah, R. Yu, Ceramics International, 40, (2014) 2091.

[153] K. Raja, P.S. Ramesh, D. Geetha, Spectrochimica Acta Part A: Molecular and Biomolecular Spectroscopy, 120, (2014) 19.

[154] J. Zhao, L. Wang, X. Yan, Y. Yang, Y. Lei, J. Zhou, Y. Huang, Y. Gu, Y. Zhang, Materials Research Bulletin, 46, (2011) 1207.

[155] B. Zhang, X.T. Zhang, H.C. Gong, Z.S. Wu, S.M. Zhou, Z.L. Du, Physics Letters A, 372, (2008) 2300.

[156]F. Ahmed, S. Kumar, N. Arshi, M.S. Anwar and B.H. Koo, CrystEngComm., 14, (2012) 4016.

[157] Z.C. Chen, L.J. Zhug, X.M. Wu and Y.D. Meng, Thin Solid Films, 515, (2007) 5462.

[158] K.J. Kim and Y.R. Park, J. Appl. Phys., 96, (2004) 4150.

[159] M. Vasanthi, K. Ravichandran, N. Jabena Begum, G. Muruganantham, S. Snega, A. Panneerselvam, P. Kavitha, Superlattices and Microstructures, 55, (2013) 180.

[160] X. Zhang, R. Zhou, P. Liu, L. Fu, X. Lan, G. Gong, International Journal of Applied Ceramic Technology, 8, (2011) 1088.

[161] R.K. Dutta, Bhavani P. Nenavathu, M.K. Gangishetty, A.V.R. Reddy, Colloids and Surfaces B: Biointerfaces, 94, (2012) 143.

[162] J. Sawai, E. Kawada, F. Kanou, H. Igarashi, A. Hashimoto, T. Kokugan, M. Shimizu, J. Chem. Eng., 29, (1996) 627.

[163] G. Applerot, A. Lipovsky, R. Dror, N. Perkas, Y. Nitzan, R. Lubart, A. Gedanken, Adv. Funct. Mater., 19, (2009) 842.

[164] N. Padmavathy, R. Vijayaraghavan, Sci. Technol. Adv. Mater., 9, (2008) 3.

[165]A. Jain, R. Bhargava, P. Poddar, Materials Science and Engineering C, 33, (2013) 1247.

[166] R. Sonohara, N. Muramatsu, H. Ohshima, T. Kondo, Biophysical Chemistry, 55, (1995) 273

[167]D.M. Smyth, Solid State Ionics, 129, (2000) 5.

[168] Y. Su-Hua, H. H. Sheng-Yu, T. Cheng-Hsun, Japanese Journal of Applied Physics, 49, (2010) 06GJ06.

[169] K. Borgohain, J.B. Singh, M.V. Rama Rao, T. Shripathi, S. Mahamuni, Phys. Rev. B, 61, (2000) 11093.

[170] R.N. Mariammal, K. Ramachandran, G. Kalaiselvan, S. Arumugam, B. Renganathan, D. Sastikumar, Applied Surface Science, 270, (2013) 545.

[171] J. F. Xu, W. Ji, Z. X. Shen, W. S. Li, S. H. Tang, X. R. Ye, D. Z. Jia and X. Q. Xin, J. Raman Spectrosc., 30, (1999) 413.

[172] J, Chrzanowski and J.C. Irwin, Solid State Communications, 70, (1989) 11.

[173] W.Y. Xu, C. Yang, M.B. Luo, L.N. Meng, G.L. Huang, Adv. Mater. Res., 177, (2011) 96.

[174] S. Rehman, A. Mumtaz, S.K. Hasanain, J Nanopart Res., 13, (2011) 2497.

[175] A. Majid, A. Ali, J. Phys. D: Appl. Phys., 42, (2009) 45412.

[176] G. Borghs, K. Bhattacharyya, K. Deneffe, P. Van Mieghem, R. Mertens, J. Appl. Phys., (1989) 4381.

[177] J.M.D. Coey, M. Venkatesan, C.B. Fitzgerald, Nat.Mater., 4, (2005), 173.

[178] A. Majid, J. Iqbal, A. Ali, J Supercond Nov Magn., 24, (2011) 585.

[179] J. Iqbal, X. Liu, H. Zhu, C. Pan, Y. Zhang, D. Yu, R. Yu, J. Appl. Phys., 106, (2009) 083515.

[180] Z. Shi, M. Zhou, D. Zheng, H. Liu and S. Yao, J. Chin. Chem. Soc., 60, (2013) 1156.

Plagiarism Declaration

Plagiarism of the thesis was carried out via turnitin (ID: 601875382) and found to be well under the allowed limit.